

G.V. Kurdyumov Institute for Metal Physics
National Academy of Sciences of Ukraine

Qualification scientific manuscript

Anastasiia Halkina

PH.D. THESIS:

**ELASTIC PROPERTIES OF ANISOTROPIC AND HETEROGENEOUS
METALLIC POLYCRYSTALS WITH CUBIC LATTICE DETERMINED BY
ULTRASONIC TEXTURE ANALYSIS**

105 – Applied Physics and Nanomaterials
Natural Sciences

Submitted for the award of the degree of Doctor of Philosophy

The dissertation contains the results of the author's own research. The use of ideas, results, and texts of other authors is duly referenced to the corresponding sources.

 A. Halkina

Supervisor: Dr. Oleh Zaporozhets

Kyiv – 2025

Анотація

Галкіна А.А. – Пружність анізотропних та неоднорідних металевих полікристалів з кубічною ґраткою, визначена методом ультразвукового текстурного аналізу – Кваліфікаційна наукова праця на правах рукопису. Дисертація на здобуття наукового ступеня доктора філософії зі спеціальності 105 – прикладна фізика та наноматеріали, Інститут металофізики ім. Г. В. Курдюмова НАН України, Київ, 2025.

Дисертаційна робота присвячена дослідженню текстури, пружних та деяких механічних властивостей анізотропних і неоднорідних металевих полікристалів за допомогою методу ультразвукового текстурного аналізу (УЗТА), зокрема, після високоенергетичних спрямованих видів термомеханічної обробки, таких як ультразвукова ударна обробка (УЗУО). Відомо, що наявність текстури у матеріалі найчастіше спричиняє анізотропію пружних параметрів, які є фундаментальними характеристиками будь-якого твердого тіла та безпосередньо чи опосередковано пов'язані з іншими фізико-механічними властивостями. Тому комплексна оцінка текстури та пружного стану матеріалів є критично важливою для забезпечення надійності роботи конструкцій, прогнозування їхньої поведінки в умовах експлуатаційних навантажень та запобігання аварійним ситуаціям. Однак таких комплексних досліджень наразі є обмежена кількість, що обумовлено, ймовірно, технологічною складністю та тривалістю їх проведення.

Традиційні методи визначення текстури, такі як рентгенівський дифракційний та нейтронографічний аналіз, характеризуються високою точністю, однак є руйнівними, вимагають ретельної підготовки зразків, застосовні лише у лабораторних умовах, а також в деяких випадках надають інформацію лише з приповерхневих шарів матеріалу. Те саме стосується й стандартних методів визначення пружних характеристик (механічні випробування, наноіндентування).

Натомість метод УЗТА є неруйнівним, експресним, дає можливість досліджувати об'єм матеріалу, різні ділянки зразків складної форми в різних геометричних напрямках, в тому числі недоступних для проведення УЗ

вимірювань. До того ж, метод УЗТА дозволяє отримати комплексну інформацію про текстурний та пружний стан матеріалу без залучення додаткових методів дослідження за допустимих для технічних задач похибок. З огляду на це, метод УЗТА є перспективним для проведення комплексних досліджень текстурних та пов'язаних із ними пружних властивостей анізотропних просторово неоднорідних матеріалів, що підтверджується отриманими в роботі результатами.

В даній роботі досліджено: 1) зразки модельного сплаву латуні Cu-37Zn у формі прямокутного паралелепіпеда (“масивні” зразки) та пластини з того ж сплаву, піддані одноразовій ударній обробці (УО) з наступною УЗУО при кімнатній та криогенній температурах (air-UIT та cryo-UIT відповідно); 2) масивні зразки та пластини високоентропійних сплавів медичного призначення 51Ti31Zr18Nb, 51Ti31Zr10Nb8Ta, 51Zr31Ti18Nb та 51Zr31Ti10Nb8Ta в литому стані та після УЗУО; 3) дрiт малого діаметру ($d \sim 1$ мм) із суперсплаву Inconel 718, підданого комплексним впливам наводнювання та УЗУО;

- УО масивних зразків Cu-37Zn призводить до кристалографічного переходу мідь-латунь, суттєвого загострення інтенсивності дифракційних ліній [111] в напрямку деформації вже при $\epsilon = 11,02\%$. При $\epsilon = 18,8\%$ вказані ефекти посилюються. Крім того, УО збільшує модуль E в напрямку деформації та поперечному, що узгоджується з текстурними змінами, оскільки кристалографічний напрямок [111] відповідає максимуму модуля E . Результат є типовим для швидкісної спрямованої деформації стиску.
- Після наступної УЗУО при кімнатній температурі (далі – кімн-УЗУО) у використаному режимі виявлено зворотній текстурний перехід латунь-мідь, пов'язаний із впливом знакозмінної складової УЗУО, що зриває з точок закріплення текстурні елементи, сформовані після УО. УЗУО при криогенній температурі (далі – крио-УЗУО) масивних зразків в аналогічному режимі не змінює типу текстури, а впливає лише на значення та анізотропію пружних параметрів. Це пов'язано з пригніченням руху дефектів, їх накопиченням, ускладненням дислокаційного ковзання та домінування двійникування як

основного механізму деформації, що і сприяє збереженню у зразках текстури типу латуні.

- Кімн-УЗУО ізотропних пластин сплаву Cu-37Zn призводить до формування текстури типу латуні вже після 20с обробки, в той час як після кріо-УЗУО навіть при 60с обробки зберігається типова текстура міді. Спостережуване двійникування та зсувні смуги у зразку після кріо-УЗУО сприяють формуванню текстури латунного типу, тоді як релаксація напружень, незвичайна дислокаційна активність, стимульована ультразвуковими коливаннями, та утворення дислокаційних комірок у зразку після кімн-УЗУО призводять до формування текстури мідного типу. Результати, отримані на масивних зразках та на пластинах Cu-37Zn, повністю узгоджуються між собою.
- отримано дані довідкового характеру про пружні параметри, їх просторову неоднорідність та анізотропію, твердість за Віккерсом та характеристику пластичності за концепцією Ю.В.Мільмана зразків із сплавів 51Ti31Zr18Nb, 51Ti31Zr10Nb8Ta, 51Zr31Ti18Nb та 51Zr31Ti10Nb8Ta в литому стані та після УЗУО. Визначено вплив концентрації Zr, Nb і Ta у сплавах та УЗУО на зміни вказаних параметрів, їх анізотропію та неоднорідність. Визначено, що Та-вмісні сплави мають суттєво вищу неоднорідність згаданих характеристик, при цьому вплив домішок Та на значення та анізотропію пружних модулів залежить від вихідного вмісту Zr та Ti. УЗУО дозволяє зменшити абсолютні значення, анізотропію та неоднорідність більшості досліджених властивостей, зокрема, модуля Юнга E сплавів, що є особливо важливим з огляду на сферу їх застосування. В процесі проведених досліджень було використано необхідне програмне забезпечення для усереднення швидкостей УЗ та пружних та механічних характеристик просторово неоднорідних та анізотропних матеріалів, що дало змогу відпрацювати методологію отримання кількісної інформації про їх ізотропні значення для негомогенних полікристалів на основі Ti та Zr.

- Вперше використано метод УЗТА для експериментальних досліджень пружних, текстурних та головних механічних властивостей дроту малого діаметру ($d \sim 1$ мм) із суперсплаву Inconel 718, підданого комплексним впливам наводнювання та УЗУО. При цьому завдяки аксіальній текстурі дроту виявилось достатнім вимірювати ν_{ij} лише в радіальному напрямку із вектором поляризації в осьовому та тангенціальному напрямках. Поряд із методом УЗТА в експериментах застосовано механічні випробування зразків на розтяг та метод дифракції зворотно розсіяних електронів (EBSD). За даними УЗТА встановлено, що під дією наводнювання поверхні дроту і, у першу чергу, УЗУО спостерігається відхилення полюсів (111) на полюсній фігурі від осьового напрямку у бік радіального. При цьому модуль Юнга E зменшується з одночасним збільшенням модулю зсуву G , що призводить до зростання твердості HV (максимально в межах 5-6%) та зміцнення зразка в осевому напрямку, що якісно корелює із результатами механічних випробувань. Зменшення характеристики пластичності δ_H при цьому не перевищує 0.8-0.9%. Для зразків, попередньо загартованих, відпалених та підданих УЗУО, зафіксовано додаткове збільшення HV після наводнювання. За результатами EBSD отримано дані про комбінований вплив поверхневої УЗУО та наводнювання на зеренну структуру та кристалографічну текстуру досліджуваних зразків, що якісно узгоджуються із даними УЗТА і підтверджують, що головним чинником впливу УЗУО та наводнювання на пружні, текстурні та механічні властивості дроту із сплаву IN718 є еволюція текстури, що у свою чергу призводить до відповідних змін пружних модулів E та G та механічних характеристик і у підсумку до зміцнення дроту в осьовому напрямку.

Отримані результати підтверджують ефективність застосованого методу пошарового УЗТА для досліджень пружних, текстурних та головних механічних властивостей анізотропних полікристалів, а також показують можливості більш широкого використання спрямованих видів деформації типу УЗУО металів для керування їх службовими характеристиками.

Ключові слова: кристалографічна текстура, пружні властивості, метод ультразвукового текстурного аналізу, анізотропні та неоднорідні матеріали, пружна анізотропія, Inconel 718, неруйнівний контроль, механічні властивості, ультразвукова ударна обробка, Ti-Zr сплави медичного призначення, мікроструктура, високоенергетична деформація

Abstract

Anastasiia Halkina - Elasticity of Anisotropic and Inhomogeneous Metallic Polycrystals with Cubic Lattices Determined by the Ultrasonic Texture Analysis

Method - Qualification research manuscript submitted for the degree of Doctor of Philosophy in the specialty 105 – Applied Physics and Nanomaterials, G. V. Kurdyumov Institute for Metal Physics of the National Academy of Sciences of Ukraine, Kyiv, 2025

This dissertation is devoted to the investigation of crystallographic texture, elastic, and some mechanical of anisotropic and spatially inhomogeneous metallic polycrystals using the ultrasonic texture analysis (USTA) method, particularly after high-energy directional thermomechanical treatments such as ultrasonic impact treatment (UIT). It is well established that the presence of texture in a material often results in the anisotropy of elastic parameters, which are fundamental characteristics of any solid and are directly or indirectly linked to other physical and mechanical properties. Therefore, comprehensive evaluation of the material's texture and elastic state is critical for ensuring structural reliability, predicting performance under service loading conditions, and preventing failure. However, such comprehensive studies remain limited, likely due to their technological complexity and time-consuming nature.

Conventional methods for texture determination, such as X-ray and neutron diffraction, provide high accuracy but are destructive, require meticulous sample preparation, and are applicable only in laboratory settings. Moreover, they often yield information limited to the surface layers. Similar limitations apply to standard methods for assessing elastic properties (mechanical testing, nanoindentation).

In contrast, the USTA method is non-destructive, rapid, and capable of probing the bulk material, including various regions of complex-shaped samples in multiple geometric directions, including those inaccessible for conventional ultrasonic (US) measurements. Furthermore, USTA allows for the acquisition of comprehensive information about both the textural and elastic states of materials without the need for additional investigative methods and within acceptable error ranges for engineering

applications. As such, USTA is a promising technique for integrated studies of textural and associated elastic properties of anisotropic, spatially inhomogeneous materials, as demonstrated by the findings of this work.

The present study investigates: 1) model Cu-37Zn brass alloy samples in the form of rectangular parallelepipeds ("bulk" specimens) and thin plates of the same alloy subjected to high-energy shock compression (HESC) followed by UIT under ambient and cryogenic temperatures (air-UIT and cryo-UIT, respectively); 2) massive specimens and plates of 51Ti31Zr18Nb, 51Ti31Zr10Nb8Ta, 51Zr31Ti18Nb, and 51Zr31Ti10Nb8Ta alloys in the initial state and after UIT; 3) fine-diameter (~1 mm) Inconel 718 alloy wire subjected to combined hydrogenation and UIT.

The following key findings were established:

- HESC of bulk Cu-37Zn specimens induces a copper-to-brass crystallographic transition and a significant intensification of the [111] diffraction lines in the deformation direction already at $\varepsilon = 11.02\%$. At $\varepsilon = 18.8\%$, these effects become more pronounced. Moreover, HESC increases Young's modulus E in both the deformation and transverse directions, correlating with the texture evolution, as the [111] direction corresponds to the maximum of E . This behavior is typical of high-strain-rate uniaxial compression.
- Subsequent UIT at the ambient temperature (air-UIT) results in a reverse brass-to-copper texture transformation due to the alternating component of UIT, which detaches the texture elements formed after HESC from their anchoring points. In contrast, UIT at the cryogenic temperatures (cryo-UIT) of bulk specimens under similar conditions does not alter the texture type but affects only the values and anisotropy of the elastic parameters. This behavior is associated with the suppression of defect mobility, their accumulation, the impediment of dislocation glide, and the predominance of twinning as the primary deformation mechanism, which collectively promote the retention of brass-type texture in the samples.
- Air-UIT of isotropic Cu-37Zn plates results in the formation of a brass-type texture after only 20 seconds of treatment, whereas cryogenic UIT preserves the

characteristic copper-type texture even after 60 seconds of exposure. The observed twinning and shear bands in the cryo-UIT-treated sample contribute to the development of a brass-type texture, while stress relaxation, atypical dislocation activity induced by ultrasonic vibrations, and the formation of dislocation cells in the room-temperature UIT-treated sample promote the formation of a copper-type texture. The results obtained for both bulk and plate Cu-37Zn samples are in good agreement.

- yielded reference data on elastic properties, their spatial heterogeneity and anisotropy, Vickers hardness, and plasticity as characterized by Yu.V. Milman's approach of 51Ti31Zr18Nb, 51Ti31Zr10Nb8Ta, 51Zr31Ti18Nb, and 51Zr31Ti10Nb8Ta alloys, both in the initial state and after UIT. The effects of Zr, Nb, and Ta concentrations and UIT on these parameters, including their anisotropy and inhomogeneity, were determined. Ta-containing alloys exhibited significantly higher inhomogeneity in these characteristics. The influence of Ta on elastic modulus values and their anisotropy depends on the initial Zr and Ti contents. UIT was shown to reduce the magnitudes, anisotropy, and spatial variability of most mechanical properties, especially Young's modulus E , which is of particular relevance to their practical applications. The study employed specialized software for averaging ultrasonic velocities and mechanical properties in spatially inhomogeneous and anisotropic materials, allowing for the development of a methodology to extract isotropic values for non-uniform Ti- and Zr-based polycrystals.
- For the first time, the USTA method was applied to study the elastic, textural, and principal mechanical properties of fine-diameter (~ 1 mm) Inconel 718 alloy wire subjected to combined hydrogenation and UIT. Due to the axial texture of the wire, it was sufficient to measure v_{ij} only in the radial direction, with polarization vectors in the axial and tangential directions. Alongside USTA, tensile tests and EBSD analyses were conducted. USTA data revealed that hydrogenation, and especially UIT, resulted in deviation of the (111) poles on the pole figure from the axial to the radial direction. This was accompanied by a

decrease in Young's modulus E and an increase in shear modulus G , leading to a hardness increase (up to 5–6%) and axial strengthening, in qualitative agreement with mechanical test results. The plasticity index δH decreased by no more than 0.8–0.9%. In pre-treated and UIT-processed samples, hydrogenation led to a further increase in hardness. EBSD results confirmed a combined effect of surface UIT and hydrogenation on grain structure and crystallographic texture, consistent with USTA data and indicating that texture evolution is the primary mechanism governing changes in elastic and mechanical properties of Inconel 718 wire, ultimately contributing to its axial strengthening.

The results demonstrate the efficacy of the USTA method for layer-by-layer analysis of elastic, textural, and principal mechanical properties in anisotropic polycrystals and underscore the potential for broader use of directional deformation treatments such as UIT in tailoring the service performance of metallic materials.

Key words: Crystallographic texture, elastic properties, the ultrasonic texture analysis method, anisotropic and heterogeneous materials, elastic anisotropy, Inconel 718, non-destructive testing, mechanical properties, ultrasonic impact treatment, Ti-Zr medical alloys, microstructure, high-energy deformation.

LIST OF PUBLICATIONS OF ANASTASIIA HALKINA

1. O.I. Zaporozhets, B.N. Mordyuk, V.A. Mykhailovskyi, **A.A. Halkina**, M.O. Dordienko, A.P. Burmak, E. Langi, L.G. Zhao, Tailoring elastic, mechanical and texture properties of Cu-37Zn brass by ultrasonic impact treatment applied at ambient and cryogenic temperatures, *Materials Today Communications* 38 (2024) 108325, Zaporozhets), <https://doi.org/10.1016/j.mtcomm.2024.108325>
2. O.I. Zaporozhets, B.N. Mordyuk*, V.A. Mykhailovskyi, A.A. Halkina, V.F. Mazanko, S.P. Vorona, Ultrasonic nondestructive evaluation of texture and elastic properties of Cu-37Zn brass subjected to shock compression and ultrasonic impact treatment, *Materials Characterization* 226 (2025) 115223. <https://doi.org/10.1016/j.matchar.2025.115223>

The research results were presented at the following conferences

1. Zaporozhets O.I., Mordyuk B.N., Mykhailovskyi V.A., Halkina A.A., Dordienko M.O. Texture evolution of and changes in elastic parameters of the Cu-37%Zn alloy after ultrasonic and impulse high-speed impact treatments. Proceedings of the Conference “Modern Problems of Metal Physics and Metallic Systems” (May 25–27, 2021). – Kyiv, Ukraine, 2021. – P. 33.
2. Zaporozhets O.I., Mordyuk B.N., Mykhailovskyi V.A., Halkina A.A., Dordienko M.O. Elastic properties of 51Ti31Zr18Nb, 51Ti31Zr10Nb8Ta, 51Zr31Ti18Nb, and 51Zr31Ti10Nb8Ta alloys in the initial state and after ultrasonic impact treatment. Proceedings of the Conference “Modern Problems of Metal Physics and Metallic Systems” (May 25–27, 2021). – Kyiv, Ukraine, 2021. – P. 34.
3. O.I. Zaporozhets, B.M. Mordyuk, V.A. Mykhailovskyi, **A.A. Halkina**, M.O. Dordienko, A.P. Burmak, E. Langi, L.G. Zhao. The influence of temperature regimes of ultrasonic impact treatment on elastic, texture and mechanical properties of Cu–37Zn brass alloy plates, *Functional Materials*

for Innovative Energy (FMIE-2023). Тези доповідей конференції (20-21 вересня 2023 р.). – Київ, 2023. – С. 75.

Table of Contents

INTRODUCTION	15
CHAPTER 1. STATE OF THE ART ON THE MATERIALS UNDER STUDY .	23
1.1 The texture formation process in Cu-Zn alloys	23
1.2 The elastic properties of 51Ti31Zr10Nb8Ta, 51Ti31Zr18Nb, 51Zr31Ti10Nb8Ta, 51Zr31Ti18Nb Alloys for Biomedical Applications	28
1.3 The texture, elastic and mechanical properties of Inconel 718 Wires subjected to combined influence of ultrasonic impact treatment and hydrogenation	32
Conclusions for the Chapter 1	36
CHAPTER 2. METHODS AND OBJECTS	38
2.1 The basis of ultrasonic texture analysis	38
3.1 Ultrasonic measurements and Ultrasonic impact treatment	43
2.3 X-ray Texture Analysis.....	48
3.3 Electron Backscatter Diffraction	50
2.4 Tensile Testing.....	52
2.5 Transmission Electron Microscopy	54
2.6 Electrochemical Hydrogen Charging	55
2.7 Characterization of the investigated materials.....	56
CHAPTER 3. RESULTS AND DISCUSSION.....	58
3.1 Texture evolution and changes in elastic and related mechanical properties of Cu-37Zn plates and massive specimens after high-energy shock compression and ultrasonic impact treatment.....	58
3.2 The influence of chemical composition and ultrasonic impact treatment on the elastic and the main mechanical properties of 51Ti31Zr10Nb8Ta, 31Ti51Zr10Nb8Ta, 51Ti31Zr18Nb, 31Ti51Zr18Nb medical alloys	81

3.3 The influence of ultrasonic impact treatment on the elastic and mechanical properties, and on susceptibility to hydrogen embrittlement of Inconel 718 alloy thin wires.....	90
THE MAIN RESULTS AND CONCLUSIONS.....	96
LIST OF REFERENCES.....	98
LIST OF ABBREVIATIONS	114

INTRODUCTION

Relevance of the Topic. In recent decades, there has been a growing interest in methods of intensive plastic deformation (IPD), which enable the formation of ultrafine-grained and nanostructured states in bulk billets of metals and alloys, creating unique physico-mechanical properties of the materials [1, 2]. Most IPD methods lead to the formation of structural heterogeneity, in particular, texture, which can cause anisotropy of the elastic properties of the material. Elastic properties, being fundamental characteristics of solid bodies, directly or indirectly interact with other physico-mechanical properties of materials.

The analysis of the texture and elastic state of materials, as well as the assessment of their heterogeneity and anisotropy, is essential for ensuring the stability of structures and preventing accidents. Understanding the relationship between the texture and elastic properties allows for predicting their behavior in different geometric directions, as demonstrated in the works with the author's participation [3, 4].

Obtaining such comprehensive information using traditional methods is possible only through separate analysis of elastic and texture characteristics. The most common approaches for determining elastic parameters (EP) include mechanical testing and nanoindentation. However, these methods are destructive, time- and effort-consuming, and in case of nanoindentation provides data only for surface layers. Additionally, assessing the anisotropy and heterogeneity of EP requires multiple applications of these methods on samples with different orientations, which further complicates the process and extends the research time.

Texture state evaluation is possible using classical texture determination techniques, such as X-ray or neutron diffraction. However, these methods also have limitations, including being destructive, labor-intensive, costly, and often incapable of providing a volumetric analysis of the material. Furthermore, layer-by-layer examination requires preparation of a lot of samples. And the texture dependence of the EP can be obtained by combination of these method with the previously discussed ones.

In this context, the method of ultrasonic texture analysis (USTA) is a promising tool for obtaining comprehensive information about the texture and EP of materials, as well as their heterogeneity and anisotropy. The accuracy of USTA is quite sufficient for most technical tasks, considering all its advantages. USTA is characterized by high speed, relative simplicity, and the ability to investigate the volume of material non-destructively with minimal error, making it highly useful for practical applications. This method also allows for the analysis of products with various geometric shapes (e.g., thin plates or complex-shaped structures with limited access), making it an important tool for scientific and technical research.

Research Aim and Objectives. The aim of the present dissertation is to provide a comprehensive characterization of the texture, elastic properties, as well as their spatial heterogeneity and anisotropy in the selected materials after the application of various technological factors, using ultrasonic measurements and the method of Ultrasonic Texture Analysis (USTA).

The **objects** of the study include the following materials:

1. The model alloy Cu-37Zn in the form of rectangular parallelepipeds with dimensions of $(4-6) \times (5-8) \times (7-10)$ mm³ was studied in the initial (textured) state, after two subsequent single impacts (the method of high-energy shock compression - HESC) resulting in 11.02% and 18.8% deformation, as well as after subsequent ultrasonic impact treatment (UIT) at room (air-UIT) and cryogenic (cryo-UIT) temperatures.
2. The model alloy Cu-37Zn in the form of thin plates with dimensions of $7 \times 7 \times 0.38$ mm³ was examined in the initial (isotropic) state and after UIT at room and cryogenic temperatures.
3. Medical 51Ti31Zr18Nb, 51Ti31Zr10Nb8Ta, 31Ti51Zr18Nb, and 31Ti51Zr10Nb8Ta alloys in the form of bulk samples and thin plates, both in the initial state and after UIT.
4. Small-diameter wires ($d < 1$ mm) of the Inconel 718 superalloy subjected to combined electrochemical hydrogen charging UIT.

To achieve this goal, the following tasks were systematically addressed:

1. Precise measurements of the material density (ρ) and the volumetric US velocities (v_{ij}) were performed in both the as-received state and after the applied treatments. The ultrasonic velocities were additionally measured at different sections of the samples to assess local variations.
2. Based on the obtained values of v_{ij} and ρ , effective elastic constants C_{ij}' were calculated, as well as the values, heterogeneity, and anisotropy of Young's modulus (E), shear modulus (G), bulk modulus (B), Poisson's ratio (ν), and the Pugh's ratio (B/G) in orthogonal directions at different regions of the samples.
3. For the Cu-37Zn massive specimens and Inconel 718 wires, based on the values of v_{ij} , ρ , and effective elastic coefficients C_{ij}' , the **orientation distribution coefficients** W_{ijk} were calculated, and **pole figures (PF)** for the main crystallographic directions were constructed. In cases where it was not possible to obtain PFs from ultrasonic measurements (e.g., for plates), additional texture characterization methods, such as X-ray or electron backscattering diffraction (EBSD), were applied.
4. Conclusions were drawn regarding the impact of the studied technological regimes on the investigated textural, elastic and some mechanical characteristics of the materials.

Research Methods. Different methods were employed to investigate the texture and elastic properties depending on the material type and sample geometry. The USTA method was applied to bulk samples of the Cu-37Zn alloy and wires of the Inconel 718 superalloy. The texture of Cu-37Zn alloy plates was also characterized using X-ray diffraction analysis EBSD. The structural state of this alloy was further analyzed by transmission electron microscopy (TEM) and selected area electron diffraction (SAED).

For the Inconel 718 wires, in addition to UTA, uniaxial tensile tests were performed to assess mechanical properties. Texture analysis of the wire cross-section was conducted using EBSD.

Ultrasonic measurements were used to determine the absolute values, anisotropy, and heterogeneity of elastic moduli and certain mechanical properties of

the alloys 51Ti31Zr10Nb8Ta, 51Ti31Zr18Nb, 51Zr31Ti10Nb8Ta, and 51Zr31Ti18Nb.

Subject of the Research.

1. Assessment of the potential to influence the texture and elastic state of Cu-37Zn samples using various methods and modes of high-speed directed treatments.
2. Effect of chemical composition and ultrasonic surface impact treatment (USIT) on the elastic and key mechanical properties of medical-grade alloys 51Ti31Zr10Nb8Ta, 31Ti51Zr10Nb8Ta, 51Ti31Zr18Nb, and 31Ti51Zr18Nb.
3. Evaluation of the potential to enhance hydrogen embrittlement resistance of thin Inconel 718 wires through radial ultrasonic surface impact treatment (USIT).

The reliability of the results obtained in this work is ensured by the use of high-sensitivity experimental techniques, as well as the application of a set of independent experimental and theoretical methods, the outcomes of which are in mutual agreement. The experiments were conducted using state-of-the-art equipment at the Department of Physical Foundations of Surface Engineering of the G.V. Kurdyumov Institute for Metal Physics of the NAS of Ukraine, at the SPM&RS Center of the NAS of Ukraine based at the same institute, and in the EBSD research laboratory of the Institute of Mechanics and Engineering in France.

Scientific Novelty

1. For the first time, an unusual brass-to-copper texture transition was observed under air-UIT. This effect is associated with the influence of the alternating component of the UIT, which facilitate the movement of fixed dislocation segments by breaking their fixation points. The study shows the possibility to obtain required texture and elastic state of the material by choosing the proper combination of high-rate deformation methods.
2. The feasibility of UIT to reducing the anisotropy and heterogeneity of the elastic and mechanical properties of Ti-Zr-based medical alloys has been demonstrated.

3. For the first time, the effectiveness of USTA method has been demonstrated for investigating the elastic, textural, and key mechanical properties of axially textured wire samples of Inconel 718-type alloys.
4. The texture factor plays a key role in the change of the elastic properties of thin Inconel 718 alloy wire subjected to hydrogen charging and/or the UIT.
5. The potential of UIT as a means of enhancing the resistance of Inconel 718 wires to hydrogen embrittlement (HE) at the surface has been demonstrated.

Scientific and Practical Significance. It was established that UIT can initiate a reverse texture transition from brass-type to copper-type in bulk Cu–37Zn alloy. This opens new opportunities for tailoring the texture and elastic state of the material, which is promising for controlling mechanical properties in engineering applications.

Generalized reference data on the elastic and mechanical properties of medical β -type Ti-Zr-Nb-Ta alloys with various compositions have been provided, which may serve as a basis for comparison with theoretical predictions. It has been shown that USIT reduces the degree of elastic anisotropy and heterogeneity in this class of alloys, which is critical for improving the functional reliability of biomedical implants. The observed increase in Young's modulus (E), shear modulus (G), and Vickers hardness (HV) in Ta-containing alloys after USIT may indicate a change in phase stability, which should be considered in the development of thermomechanical processing techniques.

The effectiveness of USTA method has been demonstrated as a fast and informative tool for assessing the texture and elastic state of complex engineering materials, including in directions inaccessible to direct ultrasonic measurements. The necessity of considering the texture factor as a key parameter affecting the elastic characteristics of thin Inconel 718 wires after combined hydrogen charging and USIT has been demonstrated. This opens the possibility for targeted texture engineering to achieve desired elastic and mechanical properties, particularly for improving resistance to degradation in hydrogen-containing environments.

The author's personal contribution. The formulation of research objectives, discussion, and interpretation of the obtained results were carried out in collaboration

with the scientific supervisor, Candidate of Physical and Mathematical Sciences, Senior Researcher O.I. Zaporozhets. The author independently conducted the analysis of scientific literature, took part in experimental US investigations were performed, the acquired data were processed, and scientific publications and conference presentations were prepared.

During an international research internship in France, supported by the “Nadiya” (“Hope”) scholarship program, the author directly participated in EBSD analysis of Inconel 718 alloy wires.

In co-authored publications, the following contributions were made personally by the author:

- In [3]: analysis of pole figures obtained via X-ray diffraction was performed; texture types of Cu-37Zn alloy plates in both initial and deformed states were identified; elastic and mechanical properties were calculated based on ultrasonic data; illustrative material and the English version of the publication were prepared.
- In [18]: pole figures for the main crystallographic directions were constructed based on ultrasonic measurements; orientation dependencies of Young’s modulus were determined; spatial variations in elastic properties in mutually perpendicular directions across different regions of the samples were analyzed; the levels of anisotropy and heterogeneity were assessed; conclusions were formulated regarding the influence of structural, particularly textural, factors on the observed changes.

The author also translated all published scientific articles into English.

Validation of Research Results. The results of the thesis have been presented in 7 scientific publications, including 2 articles in international peer-reviewed journals indexed in the Scopus database, and 5 conference abstracts published in proceedings of scientific conferences.

Core Research Theses Submitted for Defense

1. The comparing of pole figures (111) obtained after each deformation step with those typical for copper- and brass-type texture has shown that the specimen after HESC to $\varepsilon = 18,8\%$ is brass-type textured and the following air-UIT leads to inverse brass-copper texture transition. The explanation is as follows.

The alternating component the UIT plays a key role in the reverse texture transition from brass to copper in bulk Cu-37%Zn alloy samples by detaching dislocation segments from their pinning points.

2. The UIT reduces the elastic anisotropy of the 51Zr31Ti18Nb alloy from 15% to 1.1% and decreases the average Young's modulus from 87.36 GPa to 85.31 GPa. In the case of the 51Ti31Zr18Nb alloy, the maximum anisotropy remains unchanged after UIT (5.2%), while the average Young's modulus decreases by 2.63 GPa. For the 51Ti31Zr10Nb8Ta alloy, the maximum anisotropy of the Young's modulus remains high after UIT (-8.95% compared to 10.44% before UIT), although a redistribution between the directions of maximum and minimum values occurs, as evidenced by the change in the sign of anisotropy. In the 51Zr31Ti10Nb8Ta alloy, UIT causes a slight increase in the maximum anisotropy of the Young's modulus (from 0.36% before UIT to 2.71% after UIT), while decreasing the average modulus by 5.22 GPa.
3. The USTA results show the decrease in (111) texture sharpness in the axial direction is observed after UIT, and an even greater decrease after subsequent hydrogenation. Considering that Inconel 718 belongs to materials with a positive anisotropy factor, i.e., the <111> directions correspond to the maximum Young's modulus (and correspondingly the minimum shear modulus), the decrease in the intensity of [111] poles correlates with a reduction in the value of E in this direction. This is confirmed by EBSD analysis, which shows a decrease in the fraction of [111]-oriented crystallites

along the wire axial direction after the UIT combined with hydrogen charging.

Structure and Scope of the Thesis. The dissertation consists of an introduction, three chapters, conclusions, a list of references and a list of abbreviations. The total length is 114 pages.

Relation of the Research to Scientific Projects

Executor of the project, Project №1230 1A "High-strength states as a result of special interatomic interaction in high-entropy solid solutions with martensitic transformation", all-Ukrainian, G. V. Kurdyumov Institute for Metal Physics of the N.A.S. of Ukraine, 2020-2021, Presidium of the N. A. S. of Ukraine, <https://www.nas.gov.ua/UA/Messages/Pages/View.aspx?MessageID=5468>

CHAPTER 1. STATE OF THE ART ON THE MATERIALS UNDER STUDY

1.1 The texture formation process in Cu-Zn alloys

It is well known that there are two texture types in FCC metals and alloys – so called “metal-type” and “alloy-type” of texture (combination of orientations $\text{Cu}\{112\}\langle 111\rangle$, $\text{S}_3\{123\}\langle 634\rangle$, $\text{Bs}\{110\}\langle 112\rangle$) and ($\text{Bs}\{110\}\langle 112\rangle$, $\text{G}\{110\}\langle 001\rangle$, respectively) [5, 6]. They were quantitatively described for the first time in [7] (Fig. 1). In this study the textures of aluminum, copper and 70/30 brass were examined. Similar texture types were observed in the number of other fcc-metals and its’ alloys at the different operational conditions [2-9], the whole history of investigations of texture in FCC materials were generalized in the overview [10].

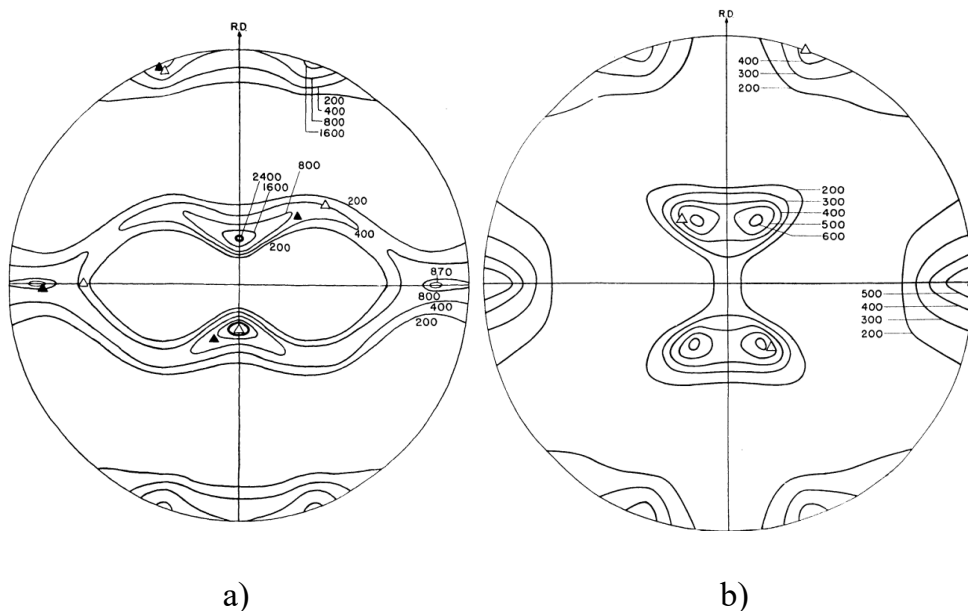


Figure 1. (111) pole figures for the inside texture of rolled copper (a) and 70/30 brass (b) [7]

The scientists have agreed that the development of one or another texture type depend on the stacking fault energy (SFE) of the material. It was firstly confirmed in [8], in which the authors investigated the texture development in pure silver under different rolling temperatures to vary SFE. It was found that with a low temperature of deformation (0°C) the rolling texture is completely (110) [112] (“alloy-type”), being identical with the rolling textures normally obtained in common silver, and with a high temperature of deformation (200°C), the rolling texture is primarily of the (123) [412] (“copper type”). It is remarkable that alloy-type texture was formed at lower

temperature. This tendency was noticed in several studies [7, 8] and finally led to the conclusion that high- and medium-SFE materials generally prone to form metal-type texture, and low-SFE ones form the alloy-type [9]. In [9] a series of alloy systems of known stacking fault energy were examined, namely pure metals aluminium, silver, gold and copper, and on the alloys of Cu-Zn, Cs-Al, Cu-Ge, Ag-Al and Ag-Au. Since that study SFE has been stated as a fundamental factor governing the change in rolling texture of FCC-materials. This statement was confirmed in the modern studies [10 and the references therein]. In [10] three materials, pure aluminium, Al-4 wt.% Mg, α -brass have been chosen to understand the evolution of texture and microstructure during rolling in order to understand the general trend in the evolution of microstructure and crystallographic texture as a function of SFE in a range of FCC materials with different SFE values. The authors [10] observed the clear change of rolling texture from metal-type to alloy-type is evident with decreasing SFE from pure Al to α -brass.

Even more, different texture types are noticed to be formed in the same material at the different deformation degrees. Remarkably, that texture formation at the early deformation stages starts with metal-type texture, and then the transition to alloy-type occurs at higher deformation degree [5]. In [5] materials from medium to low SFE were investigated, namely commercially pure Cu, Cu-10%Zn and Cu-30%Zn. It was found that the textures of the copper-zinc alloys both show a similar initial development to that of copper but a transition occurs above a reduction of about 40 per cent. This indicates that an additional deformation mode has become active. The features of the transition are consistent with those expected if the additional deformation mode were mechanical twinning. Almost the same observations were made in [11] for pure Cu and 70/30 brass, which showed similar textures up to a strain of 1.6, nevertheless that each one is characterized by very different SFE value. Noticeably, that in the materials with high SFE (pure aluminium in the mentioned study [10]) the brass-type texture can even not be formed, and in the medium-SFE material (Al-4 wt.% Mg) the metal-type texture exists up to 98% degree of deformation. At the same time, in the low-SFE α -brass the alloy-type texture formed from the very early deformation stages.

The investigated fcc-materials have been shown a strong temperature

dependence of texture formation process. In [12] the comparison between room temperature rolled and cryogenically rolled pure copper was conducted. It appears that after the cryogenic deformation the texture resembles a Brass type, while the pure metal type texture was observed after room temperature rolling.

Lowering deformation temperature make enhances deformation twinning, so that brass-type texture is more likely to be formed. Additionally, that is why texture formation process usually starts with copper-texture, and the transition to brass-type occurs at the later deformation stages, when slip is no longer possible. The mechanical twinning mechanism for rolling texture transition from the copper-type to the brass-type as proposed by Wassermann [13] and later confirmed in [14]. It is shown by the authors that if mechanical twinning and deformation faulting on the $\{112\}(111)$ orientation of the rolling texture component are prevented or nullified, for example, by cross rolling, the resulting deformation texture is essentially the same for both high- and low-SFE metals.

Since mechanical twinning is more likely to occur not only at the lower temperatures, but as well at higher deformation rate, it has been expected to be a third possible way of obtaining copper-brass transition [15, 16]. In [15], fast rolling was performed on brass containing 5% zinc by weight, using a roller speed of 25 m/min and achieving approximately 50% thickness reduction per pass, resulting in a total reduction of 94% over four passes. In contrast, slow rolling was carried out at a roller speed of about 3.5 cm/min, with each pass reducing the thickness by around 10%, requiring 30 passes to reach the same total reduction of 94%. The study confirmed that increasing the deformation rate produces a similar effect on texture as lowering the rolling temperature.

The grain size dependencies of the texture formation process were observed as well. It was shown in several studies [5, 17] that copper-brass texture transition occurs earlier in the materials with finer grain size than in the coarse-grained ones. Even more, in [17] it was also shown that texture formation process occurs stage by stage and there is an exact sequence of deformation components, which are involved into the texture formation process (Fig. 2).

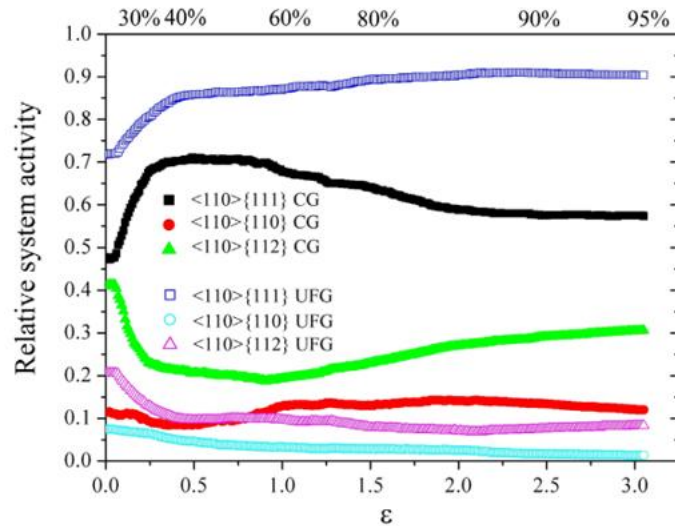


Figure 2. Relative activity of the acting slip and twinning systems in Cu-10%Zn alloy [17]

In the studies with author's participation [3, 18] both low temperature and high-speed deformation conditions were applied. In [3] initially isotropic thin plates made of low-SFE Cu-37Zn alloy were deformed by air-UIT and cryo-UIT. As it is expected, observed twinning and shear bands in cryo-UIT-ed specimen provide to the formation of the brass-type texture while the stress relaxation, unusual dislocation activity stimulated by ultrasonic vibrations and dislocation cell formation in the air-UIT-ed specimen leads to the copper-type texture.

It should be noted that the effect of UIT is also heterogeneous across the height of the specimen [18, 19] and is characterized by the presence of alternating and cumulative components of deformation [20]. The alternating component permeates the entire volume [19] of the material, while the static component is concentrated in the near-surface layer, hence their contributions to the overall deformation of the specimen significantly depend on its thickness. With the change in sample thickness, the maximum stresses developed by the static and alternating components also change accordingly. This leads to the assumption that the effect of identical UIT regimes on massive specimens and plates of the same material can qualitatively differ. In order to assess the effect of the changing ratio between alternating and static components of the UIT in the next study [18] authors have increased the thickness of specimens. In [18] the same alloy (Cu-37%Zn as in [3]) but in the form of massive rectangular parallelepiped were investigated after single shock impact, and following air- and cryo-

UIT (applied not one by one, but separately on different groups of specimens). In contrast to the previous study [3], specimens were initially copper-type textured, and after single impact a copper-brass transition occurred. Then, after air-UIT the inverse brass-copper transition was observed, while the specimens after cryo-UIT remained brass-type texture. The possible explanation proposed by the authors lies into the influence of alternating deformation component of the UIT. As explained above [5, 17], deformation components are involving one by one in texture formation process in fcc-materials. The alternating UIT-component allows moving dislocation segments fixed after single impact by breaking their fixation points. As a result, texture formation process returns to its previous stage, namely to the copper-type texture. To our knowledge, such inverse texture transition was obtained for the first time after dynamic deformation. Previously, such transition was obtained in [21] 70% thickness reduction of by cold rolling of high-purity copper followed by quenching in ice water after each 10%.

It has to be noted that texture of the material generally has significant influence on its elastic and mechanical properties [3, 4, 18, 19], and that's why it is crucially important to control and operate the textural state in it. The study [18] has shown a great and relatively easy way to obtain a proper texture state in the investigated brass alloy, and also to change already formed texture, which might be very useful for operation purposes.

To my knowledge, there are no other studies dealing with texture formation in FCC-metals under dynamic alternating loading, while it opens the great possibilities to operate the texture formation process and to obtain a required state of the material. Using that kind of treatment, it might be possible dealing with not only initially isotropic material, but with deformed one as well.

Considering all the above, it is important to develop such techniques, and as well the methods of controlling texture and elastic state. The ultrasonic texture analysis method (USTA) applied in the mentioned works [3, 4, 18, 19] has shown itself as a very convenient way to investigate texture, elastic and related mechanical properties at the same time without using additional techniques.

This method enables the analysis of the entire set of mentioned properties in a non-destructive and rapid way across different regions of the sample and along various geometrical directions. Additionally, it allows for the extraction of information from the entire volume of material within the insonified area. In contemporary scientific literature, such comprehensive data on texture and elastic characteristics are virtually absent, despite the fact that all technological treatments directly affect these properties.

So, there are two directions of great interest: the development of the methods of treatment being able to create a required texture/structure state of the material, and – in the same time – the methods to control it. If to develop both methods simultaneously, it will be the best way.

1.2 The elastic properties of 51Ti31Zr10Nb8Ta, 51Ti31Zr18Nb, 51Zr31Ti10Nb8Ta, 51Zr31Ti18Nb Alloys for Biomedical Applications

Throughout the history of alloy development, the predominant strategy has involved selecting a single base (solvent) element and incorporating minor additions of alloying elements (solutes) to tailor specific material properties. Over millennia, this approach has enabled the creation of a vast range of alloys. However, the scope for discovering fundamentally new systems using this traditional methodology has become increasingly limited—particularly with respect to enhancing structural and functional performance parameters [22].

A significant conceptual breakthrough in alloy design occurred in the early 2000s, with the introduction of multi-principal element alloys, which expanded the exploration space beyond conventional binary or ternary systems [23–28]. These alloys incorporate several major elements in comparable proportions, often resulting in surprisingly simple solid-solution phases such as disordered face-centered cubic (FCC) or body-centered cubic (BCC) structures [22]. While originally applied to high-entropy systems, this strategy has proven valuable for developing advanced biomedical titanium alloys based on Ti, Zr, Nb, Ta, and Mo.

Such expanded compositional freedom has enabled the discovery of alloys with outstanding mechanical and biological performance. Among these, Ti-based multi-

element alloys, particularly those containing Zr, Nb, Ta, and Mo, have attracted increasing interest due to their exceptional corrosion resistance, high strength-to-modulus ratio, biocompatibility, and favorable fatigue behavior [29-31]. These alloys are viewed as promising alternatives to Ti6Al4V, which—despite comprising approximately 80% of titanium implants [32]—contains cytotoxic Al and V, and has a relatively high elastic modulus (~ 110 GPa), substantially exceeding that of human bone (10–30 GPa) [33, 34]. Stainless steels and Co–Cr alloys, which are also used for bone implants, present challenges such as the release of allergenic or potentially carcinogenic ions (e.g., Co, Ni, Cr, Fe), which may trigger hypersensitivity reactions or necessitate revision surgery in up to 5% of patients [35-38].

In order to overcome the challenges associated with the use of the abovementioned alloys, researches were focused on the third-generation near- β and β -type titanium alloys, such as Ti–13Nb–13Zr, Ti–35.3Nb–5.7Ta–7.3Zr (TNTZ), and Ti–24Nb–4Zr–7.9Sn (T2248), which offer improved biocompatibility and reduced stiffness. However, strength limitations persist in some of these systems [39, 40].

The mechanical behavior and phase stability of these Ti–Zr-based alloys are primarily influenced by valence electron concentration (VEC) and the atomic size mismatch parameter δ [41]. Depending on these parameters, titanium alloys may exhibit α , $\alpha+\beta$, metastable β , or stable β microstructures at room temperature [42]. A direct proportional relationship between VEC and modulus has been observed in multi-principal Ti-based alloys, so that β -type titanium alloys with lower VEC values tend to have lower elastic moduli, while $\alpha+\beta$ alloys generally possess higher strength and stiffness [43]. This determines the potential of developing low-VEC compositions for orthopedic applications.

Among the most intensively studied Ti–Zr–Nb-based biomedical alloys are compositions that include additional elements such as Ta and Mo (e.g., TiZrNbTa, TiZrNbHfTa, TiZrNbHfMo, and TiZrNbHfTaMo) [44-46, 47-49]. These systems exhibit superior strength, attributed in part to shear modulus mismatches between constituent elements [50, 47, 48]. For instance, tensile strengths of ~ 970 MPa and 1200 MPa have been reported for TiZrNbTa and TiZrNbHfTa alloys, respectively, with

elongations exceeding 12% [44, 49]. Mo-containing alloys achieve compressive strengths above 1.4 GPa but often suffer from reduced tensile ductility [45, 46].

Nonetheless, many of these alloys exhibit elastic moduli 83–103 GPa that remain higher than ideal for osseointegration. This is largely due to the high VEC values of elements like Ta and Mo, which increase stiffness of an alloy. As shown in [32], omitting high-VEC elements such as Mo and Ta in Ti–Zr–Nb systems can substantially reduce modulus. For example, the Ti₄₅Zr₄₅Nb₁₀ alloy exhibited low stiffness and favorable in vivo bone integration after 12 weeks in rat femurs, demonstrating that strategic compositional tuning can improve mechanical compatibility.

Similarly, [49] demonstrated that removal of Mo from a Ti–Zr–Nb–Ta–Mo alloy lowered the δ parameter and quadrupled ductility while preserving strength. Although the resulting modulus (116 ± 6 GPa) remained above that of bone, it was significantly lower than in the Mo-containing alloy (153 GPa), offering a more balanced solution of implants. In the present work, Ti–Zr–Nb–Ta alloys such as 51Ti–31Zr–18Nb and 51Ti–31Zr–10Nb–8Ta achieved Young's moduli of 83.34 and 80.6 GPa, respectively, which are markedly lower than abovementioned equiatomic counterparts. Conversely, Zr-enriched variants like 31Ti–51Zr–18Nb and 31Ti–51Zr–10Nb–8Ta showed slightly higher modulus (89.65 and 91.42 GPa), despite greater δ values, suggesting that δ alone does not fully predict elastic response.

Element-specific roles in these alloys have also been clarified. Titanium (Ti) serves as the biocompatible base and stabilizes α -phase structures, while Niobium (Nb) supports β -phase formation and contributes to shear softening. Tantalum (Ta) promotes β -phase stability but increases modulus at higher concentrations. Zirconium (Zr), meanwhile, suppresses ω -phase formation and enhances ductility, synergizing with Nb and Ta to support elastic softening [29, 41-43, 51, 52].

This was also evident in [29], where increasing Zr and Ta while reducing Ti and Nb resulted in enhanced strength, modulus, and microhardness—trends corroborated by findings from the present study.

Tane et al. [51, 52] further showed that the lowest moduli in Ti–Nb–Ta–Zr alloys occur near the $\beta \rightarrow \alpha''$ transformation, where shear elastic constants soften significantly.

Alloys excessively stabilized in the β -phase (e.g., via high Nb or Ta content) tended to show higher stiffness, while near-transforming compositions reached modulus values as low as 35 GPa in the [001] direction of single crystals.

Thus, VEC and δ affect modulus not directly, but through their influence on intrinsic elastic constants and phase stability.

Further optimization in [41] studying non-equiatomic Ti(25+x)–Zr25–Nb25–Ta(25–x) alloys. Increasing Ti at the expense of Ta decreased δ from 4.72% to 4.65% and transformed brittle behavior into ductile. For example, Ti40–Zr25–Nb25–Ta10 and Ti45–Zr25–Nb25–Ta5 exhibited tensile strains above 18% and strengths exceeding 900 MPa—among the few multi-element Ti alloys achieving both strength and ductility.

Mechanical behavior can also be tuned via control of texture state. In [53], the lowest modulus (47 GPa) among bulk Ti alloys was achieved through cold rolling and texture development in Ti–13Nb–13Zr, highlighting the role of martensitic transformation and anisotropy rather than β -phase stabilization alone.

Theoretical work in [54] confirmed an inverse relationship between elastic anisotropy and VEC in the 4.1–4.8 range. Alloys such as Ti45Zr45Nb5Ta5 showed pronounced anisotropy and low directional modulus, suggesting that anisotropic elasticity can be exploited for biomedical design. Although the formation and stabilization of the β -phase remain a priority, considering that the loading conditions on the final product are not always uniaxial and it is not always possible to select a single desired direction with a minimum Young's modulus (E), there is a growing interest in the possibility of minimizing E using natural elastic anisotropy of these alloys, as well as various thermomechanical treatments.

At the same time, most studies remain limited to as-cast or annealed conditions [55, 56–58]. Thermomechanical treatments, which can enhance texture and lower stiffness, are underutilized but promising [53, 54]. Moreover, with increasing strain rate, Ti-based alloys exhibit quasi-linear strain hardening and adiabatic softening, which are desirable characteristics for implant applications. [59, 60]. Additionally, surface modifications offer additional routes for tuning mechanical performance. Shot

peening, for instance, reduced modulus from 85 to 65 GPa in β -Ti to a depth of 400 μm [61]. In this context, UIT deserves particular attention due to its influence on the subsurface structure, texture, and elastic properties [62, 63]. Further investigation of the potential of UIT as a tool for tailoring the mechanical properties of biomedical titanium alloys is warranted, taking into account the specific requirements for implant materials. This is especially relevant given that most current studies on SMAT focus primarily on surface chemical composition and morphology [64, 65], while its effect on the elastic anisotropy of materials remains insufficiently explored.

1.3 The texture, elastic and mechanical properties of Inconel 718 Wires subjected to combined influence of ultrasonic impact treatment and hydrogenation

Hydrogen can cause embrittlement in metals and alloys, a phenomenon first documented nearly 150 years ago. Back in 1874, Johnson [66] observed a substantial reduction in the fracture strain of steel and iron samples after immersion in hydrogen-containing solutions. Since that time, more than 38,000 research papers have addressed this topic [67], underlining the engineering relevance, multidisciplinary nature, and complexity of hydrogen embrittlement (HE). A comprehensive review describing HE and shedding light on its potential mechanisms is available in [68 and the references therein].

A wide array of studies have aimed at resolving the challenges posed by HE. Among the strategies explored to enhance HE resistance are thermal treatments [69], alloying [70, 71], and application of protective coatings [72-74]. However, these solutions often involve considerable cost and intricate processing steps, prompting a search for more efficient and broadly applicable preventative methods [75, 76].

Broadly, efforts to address HE can be grouped into two main strategies: (1) reducing hydrogen ingress and limiting its diffusion—often by incorporating hydrogen traps—and (2) enhancing the intrinsic strength, ductility, and fracture resistance of the material, including its resistance to hydrogen-induced cracking.

To develop such strategies, a thorough mechanistic understanding of HE is

essential. Notably, V.G. Gavriljuk and colleagues have made significant theoretical contributions by proposing an electron-centered viewpoint on hydrogen embrittlement. Their analysis, detailed in a recent review [77] and a monograph [78], focuses on two predominant mechanistic models:

1. Hydrogen-enhanced decohesion (HEDE) — wherein hydrogen reduces the cohesive strength of atomic bonds ahead of the crack tip, facilitating crack propagation without dislocation involvement.
2. Hydrogen-enhanced localized plasticity (HELP) — where hydrogen increases dislocation mobility, reduces elastic moduli by increasing the density of free electrons, and enables dislocation motion under lower applied stress, leading to localized plasticity and consequent fracture.

These two mechanisms are not mutually exclusive. According to the authors, they can act in tandem: HELP contributes to elevated local stresses ahead of a crack tip due to easier dislocation movement, while HEDE promotes crack advancement by weakening atomic cohesion in that same region [77].

Ab initio calculations and experimental observations both support that hydrogen enhances the density of states at the Fermi level in metals, resulting in metal-specific changes in their elastic moduli [77]. In elements such as iron, nickel, and titanium, hydrogenation generally causes a drop in elastic properties due to bond weakening and increased dislocation activity. In contrast, in niobium, the elastic response may differ due to its negative crystallographic anisotropy factor. In nickel, hydrogen also affects miscibility and phase stability. These diverse behaviors suggest that HE arises not from a universal mechanism but rather from a combination of dislocation activity, local chemical environment, short-range atomic ordering, and electronic structure. This multifactorial nature is particularly evident in complex alloys like Inconel 718 and other nickel-based superalloys.

A recent investigation [79] highlighted the crucial role of precipitation phases in determining the HE response of Inconel 718. It was shown that the presence of coherent γ'' precipitates exacerbates HE sensitivity by promoting planar slip and localized deformation, conditions favorable for crack initiation under hydrogen exposure. On the

other hand, the incoherent δ phase enables cross-slip and promotes more uniform deformation, thereby helping to suppress hydrogen-induced fracture. The phase morphology, volume fraction, and distribution substantially affect both hydrogen trapping behavior and fracture modes, shifting failure from intergranular to transgranular depending on the precipitate type. These findings underscore the importance of precise control over precipitation—through heat treatment or thermomechanical processing—for optimizing HE resistance in Inconel 718 [79].

A detailed understanding of the electronic and structural foundations of HE is essential for developing effective engineering countermeasures. In practice, a significant portion of contemporary research is focused on exploring strategies to reduce hydrogen uptake and retard crack propagation through microstructural modifications. A widely explored direction involves modifying the surface to limit hydrogen absorption and transport. Several surface engineering techniques—such as shot peening, laser treatment [80, 81], and ultrasonic nanocrystal surface modification (US-NMM) [82]—have been proposed to this end. These processes not only enhance surface quality but also promote grain refinement and increase dislocation density near the surface, creating effective hydrogen traps and slowing its deeper penetration.

The role of grain size in HE resistance has also been examined. In [83], experiments on Inconel 625 showed that reducing grain size, together with increasing the amount of grain boundary carbides, decreases hydrogen uptake—although only below saturation levels. Similarly, [84] noted that finer grains (and thus a higher grain boundary area) can reduce HE susceptibility in Fe-Ni alloys, although this remains debated. In face-centered cubic (FCC) metals, where bulk hydrogen diffusion is relatively slow, grain boundaries may act as both barriers and fast transport paths, depending on the boundary type [85]. Nevertheless, many studies agree that grain refinement generally benefits HE resistance [69].

According to [86], fine-grained structures inherently show greater resistance to HE than coarse-grained ones. In [87], it was also found that twin boundaries do not accommodate hydrogen atoms; thus, increasing the density of twins may reduce hydrogen sensitivity.

Given this, UIT offers a promising means of enhancing HE resistance. UIT not only improves surface quality but also induces grain refinement and increases twin density in the near-surface zone. As noted in [87], twins are less prone—or even immune—to hydrogen trapping, making UIT an especially valuable tool.

Another key strategy for improving HE resistance involves modifying the bulk crystallographic texture. Texture plays a crucial role in determining hydrogen behavior [88] due to the anisotropic nature of both crack propagation and hydrogen diffusion [89]. A number of studies have examined how texture affects HE resistance in ferritic steels. For example, in Fe–18Ni–Co steel, hydrogen-induced cracks predominantly form and propagate in grains with $\langle 100 \rangle$ //normal direction (ND) orientation, whereas $\langle 111 \rangle$ and $\langle 110 \rangle$ //ND orientations inhibit crack growth [90]. As demonstrated in [91], hydrogen diffusion varies with crystallographic orientation—it is fastest along $\langle 111 \rangle$ and slowest along $\langle 100 \rangle$. In API 5L X70 pipeline steel, a texture dominated by $\{011\}$ //ND grains enhances resistance to HE, whereas strong $\{001\}$ //ND textures are highly vulnerable to cracking [89].

Texture can be developed both during conventional thermomechanical processing and through the UIT. Furthermore, UIT improves surface condition, reducing hydrogen ingress. These dual benefits make UIT especially relevant for HE mitigation. Investigating UIT's effectiveness in this context is, therefore, of high interest.

It must be emphasized, however, that texture induces anisotropy in elastic and mechanical properties. In combination with localized hydrogen accumulation, this may lead to uneven fracture resistance. Thus, meticulous control of texture and its anisotropic effects is essential, including performing layer-by-layer and directional analyses.

USTA offers significant promise in this area, as it allows simultaneous assessment of elastic, mechanical, and textural properties without requiring complementary techniques. The fundamental principles of USTA were covered in Chapter 1 and will not be repeated here. It is worth noting, however, that for small-diameter wire samples with axial texture, USTA enables evaluation of properties along

directions inaccessible to standard methods—such as along the wire axis. Traditional approaches for such analysis are destructive and surface-focused, lack volumetric insights, and involve complex procedures.

In summary, UIT emerges as a valuable technique for mitigating hydrogen embrittlement, while USTA stands out as a comprehensive method for characterizing the effects of UIT and hydrogen exposure on materials. This makes further investigation in this direction especially relevant.

Finally, although much research has been devoted to the influence of various deformation treatments on HE resistance, similar studies involving thin wire specimens remain scarce.

Conclusions for the Chapter 1

1. Ultrasonic texture analysis (USTA) is a promising method for investigating the full range of textural, elastic, and mechanical properties of anisotropic and spatially heterogeneous materials. Its advantages include rapid implementation, relative simplicity, the ability to probe bulk material non-destructively, and the capacity to determine the complete set of the aforementioned characteristics without relying on additional techniques — all within acceptable error margins for engineering applications.
2. Ultrasonic impact treatment (UIT) is a promising material processing technique that, due to the presence of an alternating deformation component, can induce effects that are difficult or impossible to achieve using conventional static methods. There is a growing interest in dynamically oriented processing (or deformation) methods, particularly at cryogenic temperatures, as such treatments often lead to effects not attainable through static deformation alone.
3. Ti–Zr–Nb–Ta alloys demonstrate excellent combination of biocompatibility, corrosion resistance, and mechanical strength, making them strong candidates for medical implant applications. However, their elastic modulus often remains higher than that of natural bone, which can lead to stress

shielding and implant failure. UIT is a promising technique to reduce elastic stiffness by modifying subsurface texture and anisotropy. Thus, combining optimal alloy composition with post-processing methods like UIT may offer a balanced solution for next-generation biomedical implants.

4. UIT can be an effective method for increasing resistance to hydrogen embrittlement due to the possibility of implementing two approaches at once - improving surface quality and, accordingly, preventing hydrogen absorption and diffusion in the material, as well as increasing the strength and ductility of the material in certain directions by creating a texture.

CHAPTER 2. METHODS AND OBJECTS

2.1 The basis of ultrasonic texture analysis

Ultrasonic texture analysis (USTA) was systematically developed several decades ago; the theoretical background presented in this chapter is based primarily on the works of C.M. Sayers [92].

If we consider the textured aggregate, there is a correspondence between the previously discussed elastic constants of crystal C_{ij} and the elastic constants of the entire anisotropic sample C'_{ij} . The relationship between them is derived using the transformation of the crystal's coordinate system 0-XYZ into the sample's coordinate system 0-xyz through Euler angles (Fig. 3).

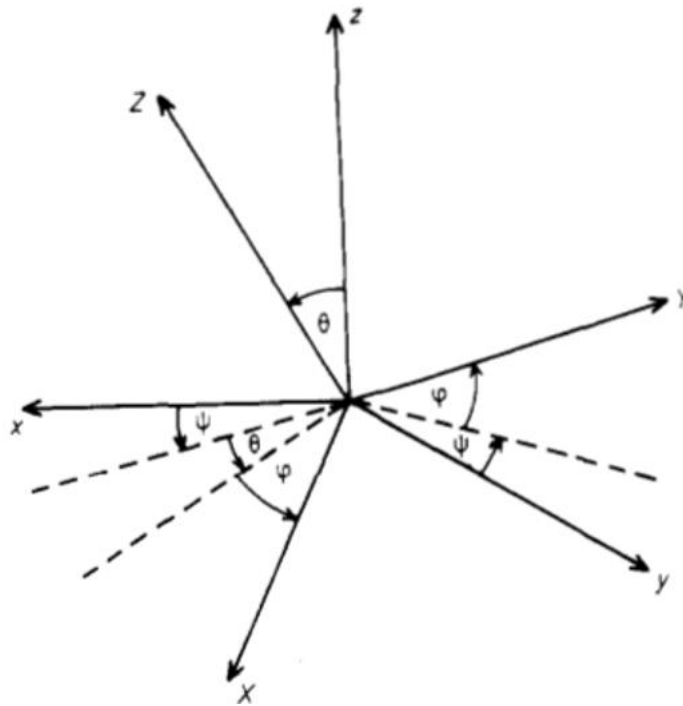


Figure 3. The orientation of the crystallite coordinate system 0-XYZ with respect to the sample coordinate system 0-xyz specified by the Euler angles ψ , θ , ϕ [92]

For an anisotropic polycrystalline sample, this requires a knowledge of the elastic constants of a crystallite in the reference frame of the sample. Under a change of axes from X,Y,Z to x,y,z where

$$x = l_1X + l_2Y + l_3Z$$

$$y = m_1X + m_2Y + m_3Z$$

$$z = n_1X + n_2Y + n_3Z$$

the elastic constants C'_{ij} in the sample frame are given in terms of those in the crystal frame C_{ij} by

$$\begin{aligned} C'_{11} &= C_{11} - 2C\langle r_1 \rangle & r_1 &= l_1^2 + l_2^2 + l_3^2 \\ C'_{22} &= C_{11} - 2C\langle r_2 \rangle & r_2 &= m_1^2 + m_2^2 + m_3^2 \\ C'_{33} &= C_{11} - 2C\langle r_3 \rangle & r_3 &= n_1^2 + n_2^2 + n_3^2 \\ C'_{44} &= C_{44} + C\langle r_4 \rangle & r_4 &= m_2^2 + m_3^2 + n_1^2 \\ C'_{55} &= C_{44} + C\langle r_5 \rangle & r_5 &= n_2^2 + n_3^2 + m_1^2 \\ C'_{66} &= C_{44} + C\langle r_6 \rangle & r_6 &= l_2^2 + l_3^2 + l_1^2 \\ C'_{23} &= C_{12} + C\langle r_7 \rangle & r_7 &= m_1n_1 + m_2n_2 + m_3n_3 \\ C'_{31} &= C_{12} + C\langle r_8 \rangle & r_8 &= l_1n_1 + l_2n_2 + l_3n_3 \\ C'_{12} &= C_{12} + C\langle r_9 \rangle & r_9 &= l_1m_1 + l_2m_2 + l_3m_3 \end{aligned}$$

It is assumed that the polycrystalline aggregate has orthorhombic symmetry, i.e., it is assumed to possess three orthogonal mirror planes given by the planes xy , yz , and zx . This is the symmetry of a rolled sheet, for example. The angular brackets in equation (4) indicate an average over all the crystallites in the sample, i.e., an average over the crystalline orientation distribution function $W(\xi, \psi, \phi)$, C is given by $C = C_{11} - C_{12} - 2C_{44}$.

In terms of θ, ψ , and ϕ the direction cosines are given by [92]:

$$l_1 = -\sin \psi \sin \varphi + \cos \psi \cos \varphi \cos \theta$$

$$l_2 = -\sin \psi \cos \varphi - \cos \psi \sin \varphi \cos \theta$$

$$l_3 = \sin \theta \cos \psi$$

$$m_1 = \cos \psi \sin \varphi + \sin \psi \cos \varphi \cos \theta$$

$$m_2 = \cos \psi \cos \varphi - \sin \psi \sin \varphi \cos \theta$$

$$m_3 = \sin \theta \sin \psi$$

$$n_1 = -\sin \theta \cos \varphi$$

$$n_2 = \sin \theta \sin \varphi$$

$$n_3 = \cos \theta$$

Expanding $r(\xi, \psi, \phi)$ as:

$$r(\xi, \psi, \varphi) = \sum_{l=0}^{\infty} \sum_{m=-1}^1 \sum_{n=-1}^1 R_{lmn} Z_{lmn}(\xi) \exp(-im\psi) \exp(-in\varphi).$$

Therefore:

$$\langle r \rangle = \int_0^{2\pi} \int_{-1}^1 \int_0^{2\pi} r(\xi, \psi, \varphi) \omega(\xi, \psi, \varphi) d\psi d\xi d\varphi = 4\pi^2 \sum_{l=0}^{\infty} \sum_{m=-1}^1 \sum_{n=-1}^1 R_{lmn} W_{lmn}$$

Through simple transformations and considering ultrasound velocities, we can then obtain [93]:

$$C'_{11} = \rho v_{11}^2 = K + \frac{4}{3}\mu + C^a \frac{12}{35} \sqrt{2}\pi^2 \left(W_{400} - \frac{2}{3} \sqrt{10} W_{420} + \frac{1}{3} \sqrt{70} W_{440} \right) \quad (1)$$

$$C'_{22} = \rho v_{22}^2 = K + \frac{4}{3}\mu + C^a \frac{12}{35} \sqrt{2}\pi^2 \left(W_{400} + \frac{2}{3} \sqrt{10} W_{420} + \frac{1}{3} \sqrt{70} W_{440} \right) \quad (2)$$

$$C'_{33} = \rho v_{33}^2 = K + \frac{4}{3}\mu + C^a \frac{32}{35} \sqrt{2}\pi^2 W_{400} \quad (3)$$

$$C'_{44} = \rho v_{23,32}^2 = \mu - C^a \frac{16}{35} \sqrt{2}\pi^2 \left(W_{400} + \sqrt{\frac{5}{2}} W_{420} \right) \quad (4)$$

$$C'_{55} = \rho v_{13,31}^2 = \mu - C^a \frac{16}{35} \sqrt{2}\pi^2 \left(W_{400} - \sqrt{\frac{5}{2}} W_{420} \right) \quad (5)$$

$$C'_{66} = \rho v_{12,21}^2 = \mu + C^a \frac{4}{35} \sqrt{2}\pi^2 \left(W_{400} - \sqrt{70} W_{440} \right) \quad (6)$$

$$C'_{23} = K - \frac{2}{3}\mu - C^a \frac{16}{35} \sqrt{2}\pi^2 \left(W_{400} + \sqrt{\frac{5}{2}} W_{420} \right) = K - \frac{5}{3}\mu + C'_{44} \quad (7)$$

$$C'_{13} = K - \frac{2}{3}\mu - C^a \frac{16}{35} \sqrt{2}\pi^2 \left(W_{400} - \sqrt{\frac{5}{2}} W_{420} \right) = K - \frac{5}{3}\mu + C'_{55} \quad (8)$$

$$C'_{12} = K - \frac{2}{3}\mu + C^a \frac{4}{35} \sqrt{2}\pi^2 (W_{400} - \sqrt{70} W_{440}) = K - \frac{5}{3}\mu + C'_{66} \quad (9)$$

where K i μ – bulk modulus and Poisson ratio of an isotropic polycrystal, respectively; ρ – the material's density; C^a – the anisotropy factor calculated using the elastic coefficients of single crystals. The index a indicates the averaging method: ($a = V$) – according to Voigt, ($a = R$) – according to Reuss, ($a = H$) – according to Hill. In this case

$$C^V = C_{11} - C_{12} - 2C_{44} \quad (10)$$

$$C^R = \frac{50(C_{11} - C_{12} - 2C_{44})(C_{11} - C_{12})C_{44}}{[3(C_{11} - C_{12}) + 4C_{44}]^2}, \quad (11)$$

$$C^H = \frac{C^V + C^R}{2} \quad (12)$$

In the present work C^a is calculated according to Eq.12.

In the Eq. (1-9) $v_{ij,ji}$ – transverse ultrasound velocities averaged over symmetric indices ($i, j = 1, 2, 3$):

$$v_{ij,ji} = \frac{v_{ij} + v_{ji}}{2}, \quad (13)$$

As can be seen from equations (1–9), ultrasonic (US) velocities are analytically related to the effective elastic constants C_{ij} and the orientation distribution function coefficients W_{ijk} (hereafter referred to as texture coefficients). The concept of USTA is based on determining these texture coefficients from the measured material density and ultrasonic wave velocities in specific directions. Using the obtained values of W_{ijk} , it is possible to construct pole figures (PFs) for the main crystallographic directions of cubic crystals — [100], [110], and [111] [94]:

$$w(\xi, \psi) = \frac{1}{\sqrt{2\pi}} \{W_{000}\bar{P}_0^0(\xi) + W_{400}\bar{P}_4^0(\xi) + [W_{420}(\bar{P}_4^2(\xi) + \bar{P}_4^{-2}(\xi))] \cos(2\psi) + W_{440}(\bar{P}_4^4(\xi) + \bar{P}_4^{-4}(\xi)) \cos(4\psi)\}$$

Here $\bar{P}_l^m(\xi) = \sqrt{\frac{(2l+1)(l-m)!}{2(l+m)!}} P_l^m(\xi)$ is the associated Legendre function and $\xi = \cos(\theta)$,

θ, ψ - the Euler angles. The value $\psi = 0$ corresponds to the RD.

The relative intensity of the corresponding diffraction lines is then calculated from the pole figures (PFs) as $\Delta I_{ijk} = I_{ijk(\max)} - I_{ijk(\min)}$

Calculation of the extreme values of Young (E) and shear (G) moduli, Poisson ratio (η) are made using following expressions [95]:

$$\frac{1}{E} = S'_{11} = S'_{11}l_1^4 + S'_{22}l_2^4 + S'_{33}l_3^4 + (S'_{44} + 2S'_{23})l_2^2l_3^2 + (S'_{55} + 2S'_{31})l_1^2l_3^2 + (S'_{66} + 2S'_{12})l_1^2l_2^2$$

$$\frac{1}{G_{12}} = S'_{66} = 4(S'_{11}l_1^2m_1^2 + S'_{22}l_2^2m_2^2 + S'_{33}l_3^2m_3^2) + (l_2m_3 + m_2l_3)^2S'_{44} + (l_3m_1 + m_3l_1)^2S'_{55}$$

$$+ (l_1m_2 + m_1l_2)^2S'_{66} + 8(S'_{12}l_1m_1l_2m_2 + S'_{23}l_2m_2l_3m_3 + S'_{13}l_1m_1l_3m_3)$$

$$S'_{12} = S'_{11}l_1^2m_1^2 + S'_{22}l_2^2m_2^2 + S'_{33}l_3^2m_3^2 + S'_{12}(l_2^2m_1^2 + l_1^2m_2^2) + S'_{13}(l_1^2m_3^2 + l_3^2m_1^2)$$

$$+ S'_{23}(l_3^2m_2^2 + l_2^2m_3^2) + S_{44}l_2m_2l_3m_3 + S_{55}l_2m_2l_3m_3 + S_{66}l_1l_2m_1m_2$$

$$\eta_{12} = -\frac{S'_{12}}{S'_{11}}$$

where S'_{ij} are the effective compliances $n_i, m_i, l_i (i=1..3)$ are the direction cosines. The matrix of direction cosines is following [95]

$$[n_{kl}] = \begin{bmatrix} l_1 & l_2 & l_3 \\ m_1 & m_2 & m_3 \\ n_1 & n_2 & n_3 \end{bmatrix}$$

The following formulas allow calculating the elastic moduli directly from measured ultrasonic velocities, averaged over propagation directions; accordingly, isotropic elastic moduli averaged over the volume of the crystal are obtained [96, 97].

$$\bar{E} = \rho \bar{v}_t^2 \frac{(3a^2 - 4)}{(a^2 - 1)}$$

$$\bar{G} = \rho \bar{v}_t^2$$

$$\bar{\mu} = \frac{(a^2 - 2)}{2(a^2 - 1)}$$

$$\theta = \frac{h}{k} \left(\frac{9Np}{4\pi M} \right)^{\frac{1}{3}} \left(\frac{1}{\bar{v}_l^3} + \frac{2}{\bar{v}_t^3} \right)^{-\frac{1}{3}},$$

$$HV = 2(B^2G)^{0.855} - 3 \quad (10)$$

$$\delta_H = 1 - 14.3(1 - \eta - 2\eta^2)HV/E \quad (11)$$

where \bar{v}_l – The longitudinal ultrasonic velocity averaged over propagation directions; \bar{v}_t – The transverse ultrasonic velocity averaged over polarization directions, $\bar{v}_t = \frac{v_{t1} + v_{t2}}{2}$; $a = \frac{\bar{v}_l}{\bar{v}_t}$; \bar{E} , \bar{G} , B , $\bar{\mu}$ – Young's modulus, shear, and bulk modulus, and Poisson's ratio averaged over the volume of the crystal, respectively; θ – Debye temperature; h – Planck's constant; k – wave number; N – Avogadro's number; M – molecular mass.

We have briefly discussed the theoretical background of USTA, which is used to investigate the properties of specific materials of interest in this study. The following section presents the ultrasonic measurement methodology, the equipment used for USTA and US, as well as the specific features of applying them to specimens of different geometrical shapes, including bulk rectangular parallelepipeds, thin plates, and wires.

3.1 Ultrasonic measurements and Ultrasonic impact treatment

US measurements were carried out in the frequency range of 10–30 MHz using the pulse-echo method and an automated apparatus created by scientific supervisor Zaporozhets O.I. and described in detail [3, 4, 18, 19]. The software for ultrasonic (US) measurements and subsequent processing of experimental data was developed by M.O. Dordiienko, Leading Engineer of Department No. 29 at the Kurdyumov Institute for Metal Physics of the NASU, and V.A. Mykhailovskyi, Ph.D. in Physics and Mathematics, Researcher of the same department.

The longitudinal (v_l) and two transverse (v_{tmax} and v_{tmin}) ultrasonic velocities in the UIT direction had been measured. Mean arithmetic values $v_t = (v_{tmax} + v_{tmin})/2$ and measured density (ρ) were used for calculations. A schematic representation of an elastically anisotropic polycrystalline specimen, taking the form of a rectangular

parallelepiped, is shown in Fig. 1. Axes aligned along the rolling (RD), transverse (TD), and normal (ND) directions are distinguished by the Arabic numerals 1, 2, and 3, respectively. In this study, the ND direction coincided with the deformation (the UIT and HESC impact) direction. Six transverse ultrasonic velocities (v_{ij}) ($i, j = 1, 2, 3$) can be measured (as shown in Fig. 4). The first subscript in the v_{ij} indicates the propagation direction of the ultrasonic wave, and the second one specifies the direction of its polarization vector. Additionally, three longitudinal ultrasonic velocities along the orthogonal directions can be measured as well. Ultrasonic velocities were determined through the employment of both transmission and reflection methodologies, concurrently with the measurement of the acoustic path length Δh and time delay τ associated with either a singular or paired reflected radio impulse(s). The instrumental error of v_l and v_t was less than 10^{-3} r.u. for $\Delta h = 1$ mm. To minimize it, the reported experimental data were averaged based on 7–10 ultrasonic measurements for each treated specimen studied. Concurrently, the density of the specimens was gauged via the differential hydrostatic weighing method, employing a quartz standard. This assessment yielded an error within the range of 10^{-3} r.u. with the specimen mass registering at 1 g. To increase the determination accuracy of the ρ changes of the processed samples, the weight of the initial samples in air and in liquid was determined relative to the corresponding weight of the initial sample with a mass of up to 10 g.

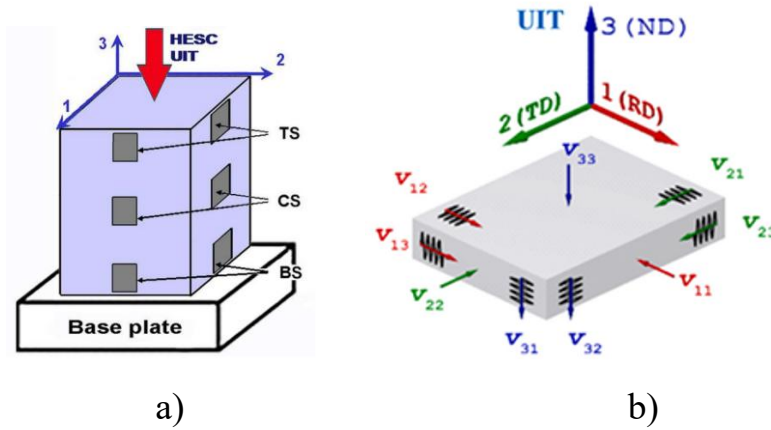


Figure 4. Schematic view of HESC, UIT and US measurements: a – the scheme of specimen with the areas of US measurements in the top (TS), central (CS), and base (BS) sections, the HESC and UIT directions, b – schematic view of a rolled specimen of cuboid shape for measurement of bulk-wave ultrasonic velocities and texture analysis of anisotropic polycrystals.

All bulk specimens were subjected to UIT in the ND, and US velocities were then measured layer-by-layer from RD and TD on three sections of specimen as shown in the Fig. 4. The UIT was carried out under the supervision of B.N. Mordyuk, Doctor of Physics and Mathematics, Head of Department No. 29 of the Kurdyumov Institute for Metal Physics of NASU. The impact treatment was performed by V.F. Mazanko, Doctor of Technical Sciences, Senior Researcher of Department No. 50, and S.P. Vorona, Junior Researcher of the same department.

The apparatus used for the UIT processing was shown in [20]. It consists of an ultrasonic generator with a power output of 0.6 kW and frequency $f = 21$ kHz. The UIT apparatus contains a plane impact punch and plane anvil both made of WC-Co hard alloy. Additionally, the UIT apparatus is pressed onto the specimen by the spring, and the spring force was chosen to be $P \sim 90$ N in this study. When ultrasonic vibrations are on, the plane impact punch positioned between the vibrating ultrasonic horn and the specimen situated on the anvil starts to produce repetitive impacts with a frequency $f \sim 1$ kHz. In the used UIT loading unit, the treated specimen is free to expand radially due to the absence of constraint in the described UIT scheme. This feature affects the resulting stress state and UIT-straining behavior of the treated specimens, which are different in comparison with those produced in other UIT loading units containing the

holder restricting the specimen expansion [98, 99]. It should also be noted that a specific feature of the applied UIT technique is that the high-frequency contact between the specimen, the punch, and the concentrator leads to a reduction in the friction coefficient without lubrication. As a result of the deformation, a hourglass-like shape of the specimen is formed.

The brass specimens (both massive and plates) were subjected to UIT at ambient (air-UIT) and cryogenic (cryo-UIT) temperatures, but the Cu-37Zn massive specimens were subjected to high energy shock compression (HESC) first. The scheme of HESC was similar to that given in the fig.4a, but in the ND a single impact with a flat striker was performed when a load weighing 10.5 kg fell freely on it from a height of 1.0 m and 1.75 m to deform the sample by 11.02% and 18.8%, respectively. The scheme of treatment steps is shown in the Fig. 5.

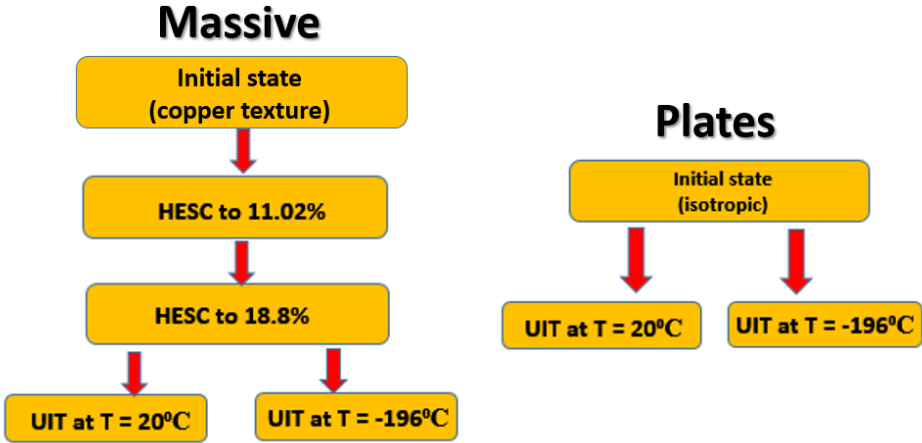


Figure 5. The scheme of treatment steps for massive specimens and plates made of Cu-37Zn alloy

In case of bulk specimens, the whole set of 9 bulk US velocities is possible to measure, while for thin plates, the US measurements are possible only in the ND (namely, only v_{33} , v_{31} , and v_{32}), which is not enough to conduct USTA. For texture examination in the Cu-37Zn alloy plates the X-ray diffraction and EBSD methods were used (described in the next subsections).

In case of axially textured thin wires considering their small thickness, the only velocities propagating in the radial direction are possible to obtain by US

measurements (namely, v_{11} and v_{12} or v_{22} and v_{21}), which is also not enough for texture analysis, since we need at least three values of v_{ij} , obtained from at least two orthogonal planes. Since we are dealing with axially textured wires, we have additional equalities between velocities, namely $v_{11} = v_{22}$, $v_{21} = v_{12}$, $v_{32} = v_{31}$, $v_{23} = v_{13}$. Then, using above-described mathematical relationships (namely, the eq.(1-9)), we can calculate the whole set of 9 v_{ij} -values as like as for usual bulk specimen. It leads to important possibility to obtain the values of v_{ij} and related elastic properties in all directions despite the fact that ND is inaccessible for conducting US measurements. The scheme of US measurements, UIT and appropriate coordinate system of wires is given in the Fig.6

In order to confirm USTA results by direct methods of texture analysis the EBSD from the cross section of wires was conducted.

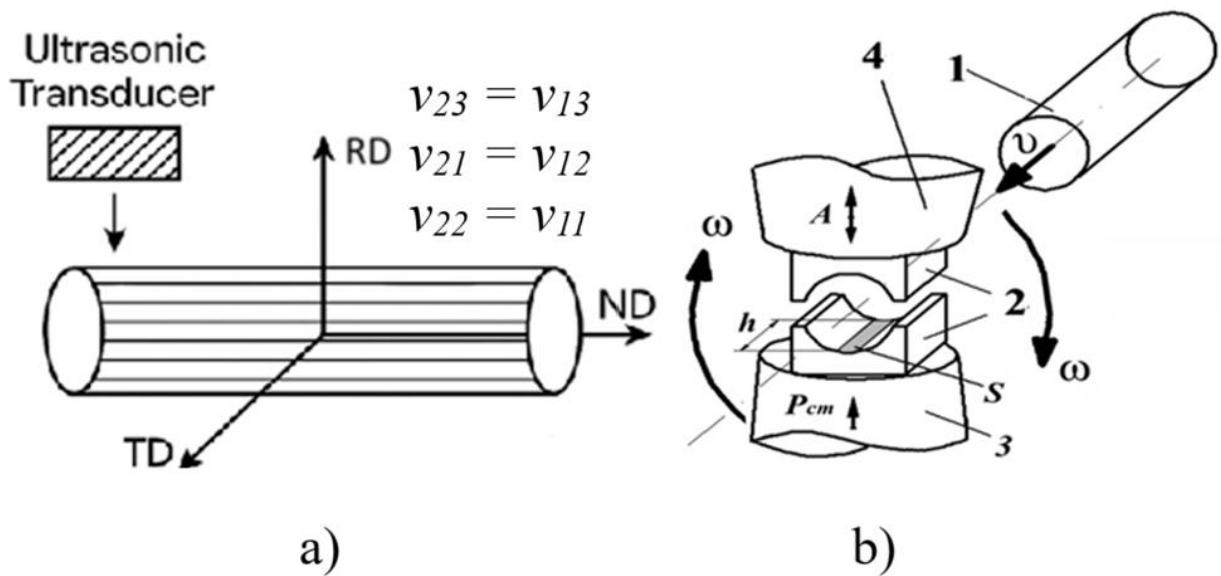


Figure 6. The scheme of US measurements with the appropriate coordinate system (a) and the UIT (b) of the wires of Inconel 718 alloy

These wires were subjected to hydrogenation from the radial direction before/after UIT (the sequence of treatment was different of the different specimens in order to find the best combination helping to protect the material from HE). The detailed description of investigated specimens and applied treatment are given in the 2.6 subsection.

2.3 X-ray Texture Analysis

This method utilizes X-ray diffraction (XRD) to measure the distribution of orientations of grains within a sample. X-ray diffraction is based on Bragg's law [100, 101]:

$$n\lambda = 2d \sin \theta$$

where n is an integer, λ is the X-ray wavelength, d is the interplanar spacing, and θ is the diffraction angle.

When a polycrystalline sample has a random grain orientation, the diffraction pattern exhibits isotropic intensity. However, in textured materials, certain crystallographic planes are preferentially aligned, leading to an anisotropic diffraction intensity distribution, which is captured in diffractograms. A diffractogram is a plot of diffracted X-ray intensity as a function of the diffraction angle (2θ) (see Fig.7).

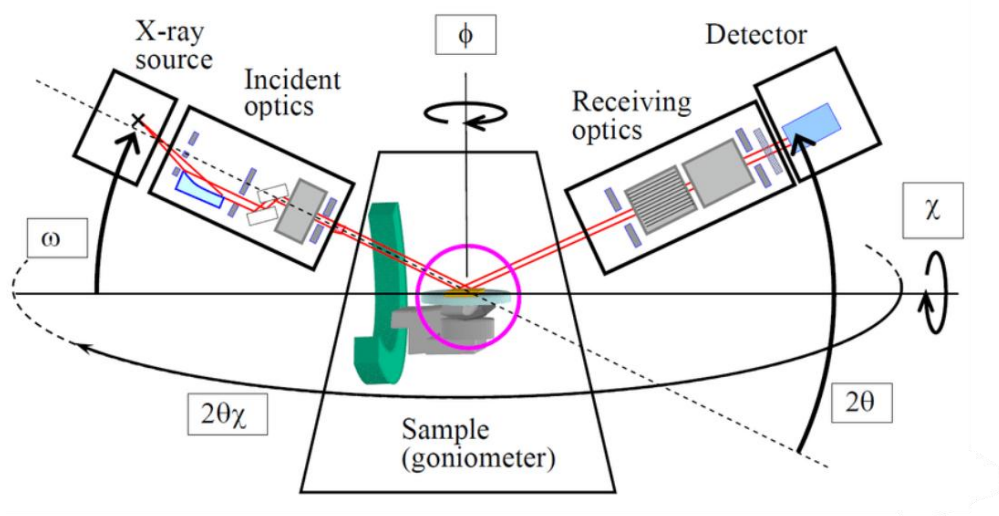


Figure 7. A schematic illustration of 5-circle goniometer system [101].

To extract meaningful texture information from diffractograms, several key aspects must be analyzed:

- ✓ Peak Positions (2θ Values):

The position of diffraction peaks corresponds to specific crystallographic planes. Any shifts in peak positions may indicate strain, residual stresses, or variations in lattice parameters.

✓ Peak Intensities:

In a randomly oriented polycrystalline sample, diffraction peak intensities match standard reference values. In textured materials, deviations from standard intensities indicate preferred orientation of certain grains. Peaks corresponding to specific planes may be significantly enhanced or suppressed.

✓ Peak Width:

Broader peaks suggest smaller grain sizes, lattice strain, or a distribution of orientations. Narrow peaks indicate well-defined, highly oriented grains.

✓ Asymmetry and Splitting of Peaks:

Asymmetric peaks or peak splitting may indicate multiple texture components or phase transformations. Such features can be analyzed using deconvolution techniques to separate overlapping peaks.

✓ Texture Index Calculation:

The Texture Index (J) quantifies the degree of orientation within a sample. Higher values indicate stronger texture, while $J = 1$ represents a random orientation.

✓ Comparing Diffractograms at Different Sample Orientations:

By collecting diffractograms at different tilt angles, variations in peak intensity can be mapped to determine pole figures and reconstruct the full texture using the Orientation Distribution Function (ODF).

In this study X-ray diffraction method of texture analysis was used for Cu-37Zn thin films since USTA was inapplicable in this case. X-ray analysis of the surface layers was conducted using a Rigaku Ultima IV diffractometer with copper radiation ($\text{Cu K}\alpha$, $\lambda = 0.15418 \text{ nm}$). The Bragg-Brentano focusing scheme was employed. The scan was performed at a step size of 0.04° with record time at each point of 2 sec and 2θ kept in the range of 20° and 100° . Analysis of the acquired X-ray spectra, as well as quantitative and qualitative phase analysis were performed using PDXL software, the

international diffraction database ICDD (PDF-2), and the open crystallographic database COD. The calculation of coherent scattering regions (CSR) and the degree of crystallographic lattice deformation was executed utilizing the Holder-Wagner method [10,33–35]: $\beta \cos\theta = \varepsilon(4\sin\theta) + k\lambda/D$, (11) where β , θ , λ , D and ε are the physical broadening of full width at half maximum (FWHM) of the diffraction peak, the Bragg angle, the wavelength of the radiation, crystallite size and internal strain, respectively. The author acknowledges Dr. X and colleagues for conducting Ph.D, Associate Professor, Senior scientist at the NTUU “Igor Sikorsky Kyiv Polytechnic Institute” A.P. Burmak for conducting X-ray structural analysis of Cu-37Zn alloy samples.

3.3 Electron Backscatter Diffraction

Unlike X-ray diffraction, EBSD enables spatially resolved texture analysis by mapping grain orientations on a microstructural scale. EBSD is performed in a Scanning Electron Microscope (SEM), where a highly focused electron beam interacts with a polished sample surface, producing backscattered electrons that diffract according to the crystal structure [102]. These diffracted electrons form Kikuchi patterns, which contain information about the crystal orientation at each scanned point.

To obtain high-quality EBSD data, proper sample preparation and instrumental settings are essential:

✓ Sample Preparation:

The sample surface must be highly polished, often using mechanical polishing followed by ion milling to remove surface damage.

✓ SEM Parameters:

The sample is tilted to 70° relative to the electron beam to optimize diffraction conditions. Accelerating voltage typically ranges between 15-30 kV to enhance Kikuchi pattern visibility. Low beam currents help prevent excessive heating or damage to the sample.

✓ EBSD Detector:

A phosphor screen detects Kikuchi patterns, which are captured by a high-sensitivity camera. Real-time software processes and indexes these patterns to determine the crystal orientation at each scanned point.

✓ EBSD Data Acquisition

EBSD scans consist of a grid of measurement points, where each point produces a Kikuchi pattern. These patterns are indexed to obtain local orientation data, which are compiled into orientation maps. The SEM stage moves systematically, collecting Kikuchi patterns across the selected area. Orientation data are stored as Euler angles, which define the crystal orientation relative to the sample coordinate system. Pole Figures are constructed from EBSD data, similar to X-ray texture analysis, but with higher spatial resolution. Inverse Pole Figures show the preferred orientation of a specific sample direction relative to the crystal axes. EBSD can distinguish between high-angle and low-angle grain boundaries, providing insight into recrystallization and deformation processes. Multiphase materials can be analyzed by comparing Kikuchi patterns to known crystallographic databases, allowing phase mapping.

EBSD generates color-coded maps, where each grain is assigned a color based on its crystallographic orientation. These maps help visualize texture variations across a sample. Kikuchi Pattern Quality (Band Contrast) images highlight areas with well-defined diffraction patterns (e.g., strain-free grains) versus regions with distorted patterns (e.g., deformed or amorphous zones).

Grain size histograms and misorientation angle distributions provide statistical insights into texture evolution and mechanical properties.

By analyzing pole figures and inverse pole figures, dominant texture components can be identified. The Orientation Distribution Function (ODF) is used to quantify texture strength and preferred grain orientations.

In this study EBSD was used for Cu-37Zn thin films and Inconel 718 wires to obtain orientation maps, direct and inverse PF, and in case of Inconel 718 the fraction of crystallites of the main cubic orientation [100], [110], and [111], And in case of Cu-37Zn thin films for grain size distribution as well.

EBSD was conducted using the SEM JEOL 7800 equipped with an Oxford Nordlys II S EBSD detector and post-processed with HKL Channel 5.0 EBSD software. The specimen was tilted at an angle of 70° and maintained at a working distance of 10 mm. The accelerating voltage and microscope step size were 20 kV and 0.5 μm, respectively. EBSD analysis was utilized to extract crystallographic information about individual grains and the corresponding misorientation angles of grain boundaries. The grain size in the specimens was estimated using the diameter of a circle with an equal surface area.

The author acknowledges the team of Electron Microscopy Laboratory No. 43 of of the Kurdyumov Institute for Metal Physics of NASU – for the professional preparation of Inconel 718 alloy wires for research in France and for their advisory support in selecting analysis parameters, and as well Jean-Marc Olive, Ph. D, Senior scientist CNRS 12M, and Arnaud Proietti, Ph. D, the specialist of the Electron Microscopy Laboratory at the CNRS – for the organization, highly qualified technical and methodological assistance during EBSD analysis of Inconel 718 wires.

2.4 Tensile Testing

By applying an increasing uniaxial tensile force to a specimen until failure, critical mechanical parameters can be extracted [103].

Assuming a uniform distribution of the external force throughout the body, then there is a portion of the external force (F) that runs through any cross-sectional area (A) of the body and an internal force (F') that opposes this external action. This internal force in any given cross-section is known as “Stress” and can be expressed as [103]:

$$\sigma = \frac{F}{A}$$

Relative strain describes the relative elongation or compression of an element with respect to its original length.

The strain of an element with an original length L and a change of length ΔL is defined as [103]:

$$\epsilon = \frac{\Delta L}{L}$$

The main steps of tensile testing:

1. Specimen Preparation:

- Standardized specimens are used to ensure uniform stress distribution.
- Surface finish and dimensions follow ASTM or ISO standards.

2. Test Procedure:

- The specimen is gripped and stretched at a constant strain rate.
- Stress-strain data (Fig.8) are recorded until failure.

The analysis of stress-strain curve allows to obtain the Young's modulus of the material (as stress divided by strain in the elastic region of the curve) and the main mechanical properties as well. The list of these properties and the corresponding point on the curve are given below:

- Yield Strength: Stress at which permanent deformation begins.
- Ultimate Tensile Strength: Maximum stress before necking occurs.
- Fracture Point: Stress at which the material breaks.

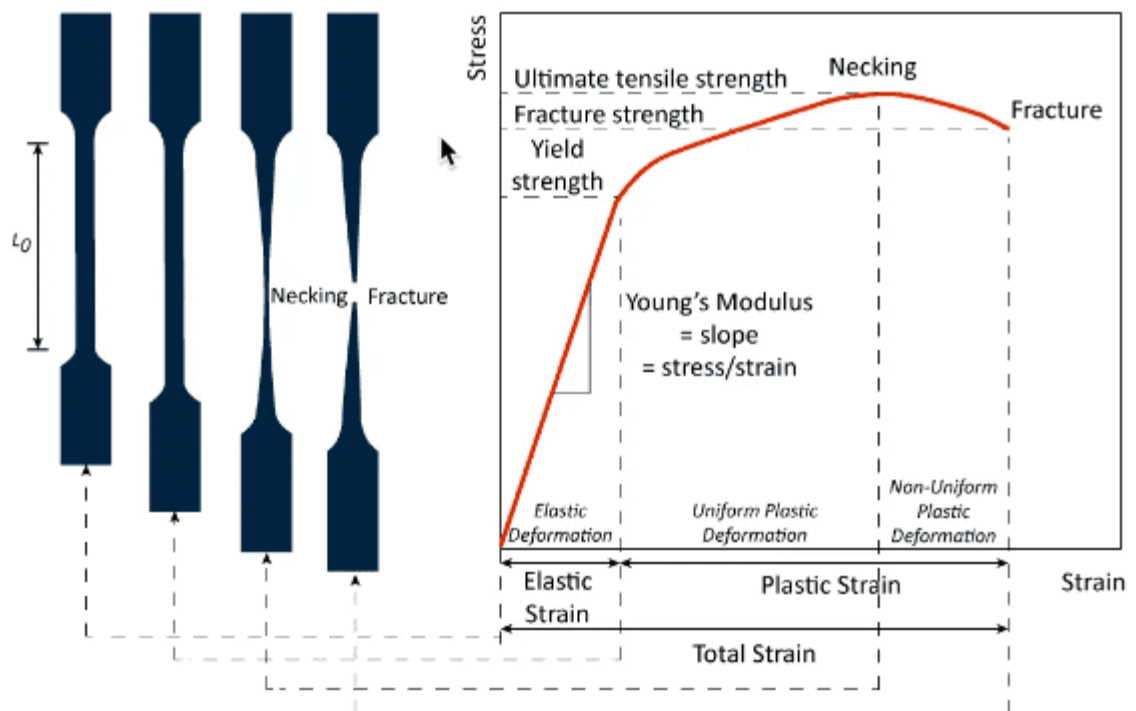


Figure 8. Schematic representation of tensile deformation stages and corresponding stress-strain behavior of ductile materials [104]

In this study tensile testing was applied to Inconel 718 wires after WQ, annealing at the different temperatures and subsequent hydrogenation and/or UIT. These experiments were organized and conducted by B.N. Mordyuk, Doctor of Physics and Mathematics, Head of Department No. 29 of the Kurdyumov Institute for Metal Physics of NASU and Doctor Sciences, Senior Researcher, and Head of Laboratory of Physics of Construction Materials No. 44, V.M. Shyvaniuk.

2.5 Transmission Electron Microscopy

Transmission Electron Microscopy (TEM) is a high-resolution technique used to analyze the microstructure, defects, and crystallography of materials at the nanometer and atomic scales [105]. TEM operates by passing a highly accelerated electron beam (typically 100-300 kV) through a thin specimen (Fig. 9). As electrons interact with the material, they experience scattering, diffraction, and absorption, forming a complex contrast pattern that reveals fine structural details.

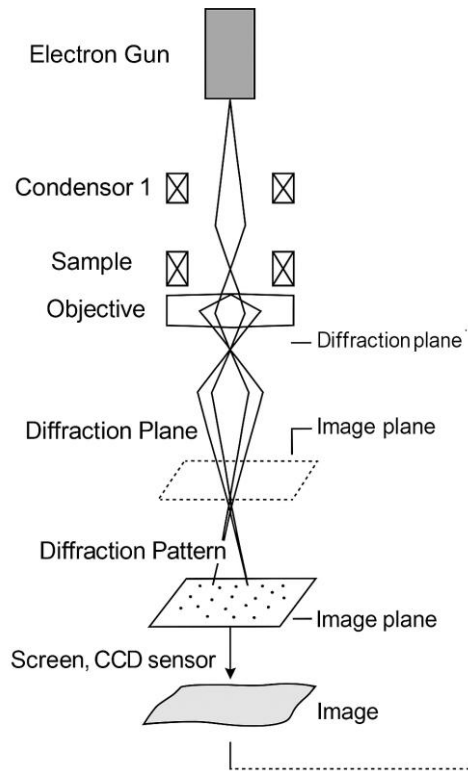


Figure 9. Schematic diagram of electron beam path and image formation in a transmission electron microscope TEM [105]

In this study TEM using a JEOL-CX-II 100 microscope was applied to observe the microstructures of the Cu-37Zn thin plates specimens. The plane-view TEM foils were prepared according to a standard procedure using an electrolytic polishing technique. The one-side polishing technique was used to less deformed samples to obtain the microstructural data from the top surface layers of $\sim 30\text{--}50\ \mu\text{m}$.

2.6 Electrochemical Hydrogen Charging

Electrochemical hydrogen charging is a widely used method for hydrogenating metallic materials, including thin wires ($<1\ \text{mm}$), by utilizing an electric current to promote hydrogen evolution at the specimen surface immersed in an electrolyte [106]. The wire acts as the cathode in an electrochemical cell, typically in an aqueous acidic solution (e.g., H_2SO_4 , HCl) or neutral solutions with added catalytic agents (e.g., thiourea, arsenic trioxide) to enhance hydrogen entry.

Under cathodic polarization, hydrogen ions (H^+) are reduced to atomic hydrogen at the wire surface. Some of the adsorbed hydrogen atoms diffuse into the metal lattice, while others recombine to form molecular hydrogen. The current density, charging time, temperature, and electrolyte composition are carefully controlled to achieve desired hydrogen concentrations and diffusion profiles.

This technique is especially useful for simulating hydrogen embrittlement phenomena, studying hydrogen transport mechanisms, and pre-charging samples for mechanical or spectroscopic evaluation. It is relatively simple to implement and enables localized or uniform hydrogenation, depending on setup geometry and current distribution. In this work the hydrogen charging of Inconel 718 wires were organised by Doctor Sciences, Senior Researcher, and Head of Laboratory of Physics of Construction Materials No. 44, V.M. Shyvaniuk.

2.7 Characterization of the investigated materials

In this subsection the description of investigated specimens of all used materials will be briefly given.

The Cu-37%Zn specimens in the form of rectangular parallelepipeds with dimensions of (4-6) x (5-8) x (7-10) mm were used. Specimens were cut from the sheet cold-rolled to a 70 % thickness reduction and underwent stress-relieving annealing at 320 ° C for 0.5 h. These specimens had a copper-like texture in their initial state and were subjected to HESC at $\varepsilon = 11.02$ % and after to $\varepsilon = 18.8$ %.

Cu-37%Zn alloy plates were with dimensions of 7×7×0.38 mm³. The reduction in specimen thickness allows for the enhancement of their homogeneity across the post-treatment height.

The Ti-Zr alloys specimens of two geometric shapes were used: rectangular parallelepipeds with dimensions of (4.5-5.9)x(5-6)x(8-9) mm³ and plates with a thickness 1.5-1.7 mm. The production of the initial specimens was carried out in a vacuum arc furnace using a non-consumable electrode on a copper water-cooled tray in an argon atmosphere at a constant excess pressure of $P = 0.05$ MPa. To purify the argon atmosphere, in one of the crucibles of the tray, a Ti-Zr getter (50/50 wt. %) was

pre-melted. The weight of the cylindrical ingots was 30 g (weight deviation did not exceed 0.01%). To homogenize the chemical composition, 7 remeltings were performed. The uniformity of the specified chemical composition of the ingots was confirmed by analyzing two extreme parts of the cylindrical specimens using a VRA-20 X-ray fluorescence spectrometer (Germany). The results of the chemical analysis confirmed the volume uniformity of the melted alloys' specified composition and the low content of impurities in it. According to X-ray structural-phase analysis (XSPA), all melted alloys in the as-cast state had a single-phase FCC structure.

In the table 1 the composition of the investigated alloys is presented.

table 1. Alloys' composition (at. %)					
Specimen №	Ti	Zr	Nb	Ta	Short name
1	51	31	18	-	1TZN
2	51	31	10	8	2TZNT
3	31	51	18	-	3ZTN
4	31	51	10	8	4ZTNT

The specimens of Inconel 718 were in the form of thin wires with the thickness of 1mm (radial direction) and with the length of about 5 mm (axial direction). They were subjected to water quenching (WQ) from 1030°C with subsequent annealing at 870°C. After that the specimens were subjected to electrochemical hydrogen charging and UIT in different sequences from the radial wire direction.

CHAPTER 3. RESULTS AND DISCUSSION

3.1 Texture evolution and changes in elastic and related mechanical properties of Cu-37Zn plates and massive specimens after high-energy shock compression and ultrasonic impact treatment

In this sub-chapter the comparison between the influence of UIT on plates and massive specimens of the same Cu-37Zn alloy will be given.

As described in the Chapter 2, Cu-37Zn massive specimens were initially copper-type textured, then after HESC copper-brass transition occurred, which is common feature for this case. The copper-brass texture transition was also obtained in [107] in the pure Cu after a single high-speed shock, even though copper-type texture is preferable for medium-SFE materials such as Cu [5].

In Fig. 10, the normalized pole figures of the specimen in its initial state (Fig. 10, a), after HESC to $\varepsilon = 11.02\%$ (Fig. 10, b) and HESC to $\varepsilon = 18.8\%$ (Fig. 10, c) are shown, and Fig. 11 demonstrates the relative intensity of diffraction line $\Delta I_{(111)}$. To identify the type of texture the following figures were compared to [17].

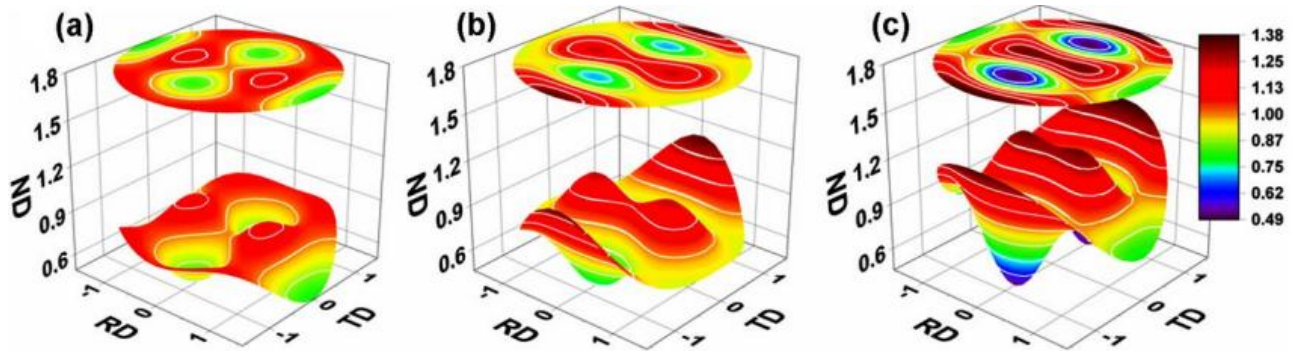


Figure 10. The normalized pole figures (111) for the specimens in initial state (a), after HESC to $\varepsilon = 11.2\%$ (b) and after HESC to $\varepsilon = 18.8\%$ (c).

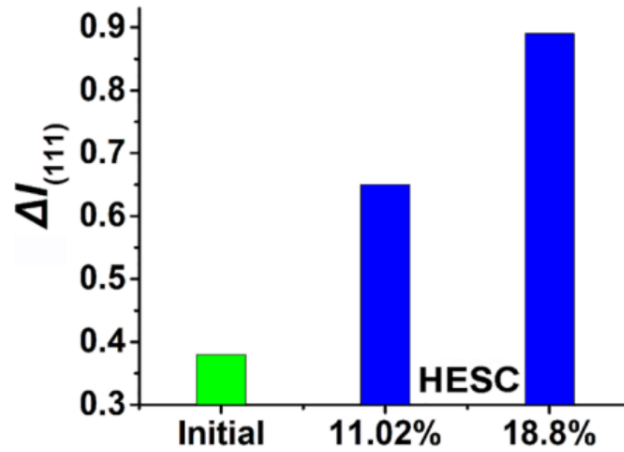


Figure 11. The relative intensity of diffraction line $\Delta I_{(111)}$ for the specimens in the initial and HESC processed states

In Fig. 12, the normalized PF (111) for the specimens after HESC to 18.8% (Fig. 12, a), air-UIT (Fig. 12, b), and cryo-UIT (Fig. 12, c)) are shown. As mentioned above, the specimen after HESC to $\varepsilon = 18.8\%$ is brass-type textured. The following air-UIT process leads to an inverse brass-copper texture transition. This effect is accompanied by some texture scattering which is also indicated by decreasing of $\Delta I_{(111)}$ (Fig.13)

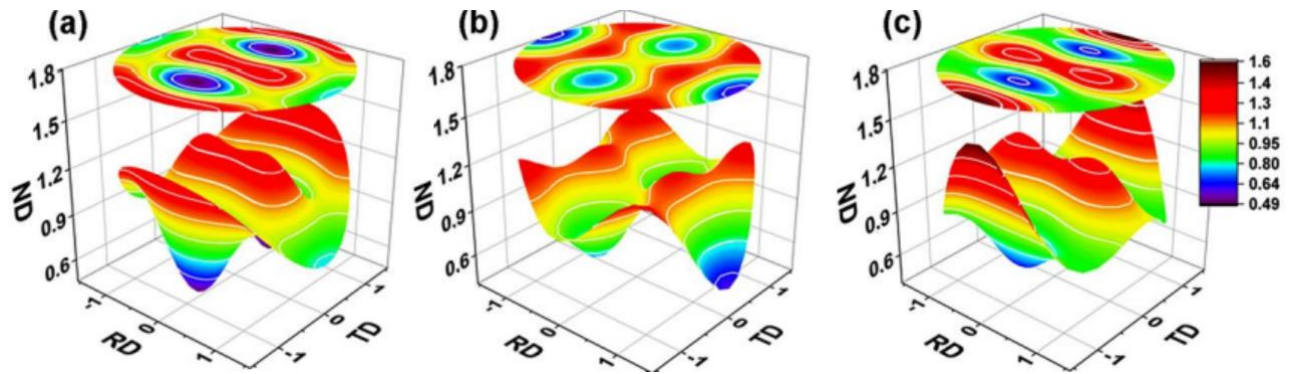


Figure 12. The (111) pole figures for the specimens after HESC to $\varepsilon = 18.8\%$ (a), air-UIT (b), and cryo-UIT (c).

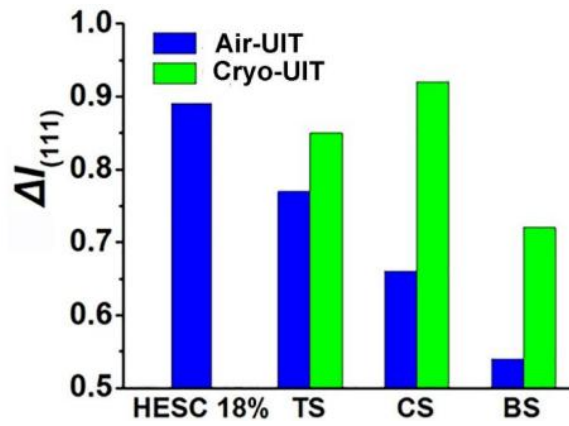


Figure 13. The relative intensity of diffraction line $\Delta I_{(111)}$ for various sections of the specimens after HESC and following air-UIT and cryo-UIT.

Such texture transition is untypical for Cu-Zn alloys, and there is little data about it in modern scientific literature. It was only reported in [21], where high-purity copper was cold rolled to an overall 70% thickness reduction by a step-like rolling/quenching in ice water after each 10%. The authors explained this effect as follows: during 70% cold rolling, the new dislocation-free grains with Cube orientation formed at 60% strain owing to discontinuous dynamic recrystallization and then rotated toward Copper components. In the present study, the inverse brass-copper texture transition for the first time was obtained by UIT. The possible explanation can be as follows.

During the deformation of FCC alloys, texture evolution follows a sequence from copper-type to brass-type. This transition occurs gradually over a strain range, with its onset and extent primarily governed by the material's stacking fault energy (SFE). In lower SFE materials, the transition begins earlier and it spans a wider strain range due to restricted cross-slip and recovery whereas it starts at a higher strain in higher SFE alloys, but follows a similar progressive evolution [5]. So, the presence of brass-type texture suggests that the material has reached the later stages of its deformation-induced texture evolution. Our experimental results indicate that the alternating component of UIT can lead to a shift from brass-type back to copper-type texture. We suggest that alternating component of UIT may facilitate dislocation movement by breaking fixation points, which alters the deformation mechanisms and influences texture evolution. However, further investigation is necessary to understand all the underlying mechanisms. This process is accompanied by decreasing texture

sharpness (Fig. 13) as the result of grain refinement usual for the UIT [108]. In contrast, cryo-UIT causes much less texture scattering and also random height distribution of $\Delta I_{(111)}$ possibly because of the liquid nitrogen influence on the contact between the specimen and horn/base plate.

In contrast to this, the specimen after the cryo-UIT is still brass-type textured which is indicated by the PF (Fig. 12, c). The absence of texture changes after cryo-UIT can be explained as follows. According to current understanding [5, 17 and the references therein], a brass-type texture forms due to twinning. This is why the copper-brass transition occurs at later stages of deformation, when slip is no longer possible, or if it is suppressed for other reasons (e.g., low temperature and/or high deformation rate).

In the case of room temperature deformation, dynamic recovery processes may occur, which may result in a reverse brass-copper texture transition, especially in high or middle-SFE materials (like aluminium or copper, respectively). Moreover, some local deformation heating could also facilitate the accelerated structural relaxation in the studied alloy. Such deformation-induced heating was earlier observed in various metals either at UIT [109] or at applied US vibrations [110], as well as at highenergy impact straining [111]. Furthermore, the operative temperature for dynamic recrystallization was reported to be essentially diminished in the severely deformed materials and, particularly, in the materials that underwent so-called “megaplastic” deformation [112]. In the above-mentioned study [21] quenching was specifically applied after every 10% of deformation exactly to prevent dynamic recovery of rolled copper. In the case of the investigated Cu-37Zn alloy characterized by a low SFE, the main influence on the texture transition is exerted by the alternating component of the UIT. These vibrations can release dislocations and dislocation boundaries from their pinning points, increasing their mobility.

TEM observations of the microstructure formed of the studied specimens confirm the operation of different deformation mechanisms in the variously deformed specimens of the Cu-37Zn alloy (Fig. 14). Fig.14a shows the bright-field image of the HESC induced microstructure, which contains a highly dislocated matrix with

numerous dislocation tangles/bundles and shear bands initiated due to high-rate straining. The corresponding SAED pattern contains the spots, which are scattered both in azimuthal and radial directions. The microstructures of the HESC-treated specimens (Fig. 14, b), which underwent either air-UIT (Fig. 14, b) or cryo-UIT (Fig. 14, c) processes, are also shown in this figure and accompanied by the appropriate SAED patterns. As seen, a highly misoriented ultrafine-grained microstructure with grains/subgrains of 20–50 nm in size is formed after the air-UIT process (Fig. 14, b). The diffraction spots become more azimuthally scattered beginning to create a ring-shaped SAED pattern. On the contrary, the cryo-UIT resulted in another type of microstructure evolution due to the involving twinning process (Fig. 14, c). The highly dislocated matrix is observed to be subdivided by numerous twins, which thickness ranges from 15 to 40 nm. The corresponding SAED pattern contains additional twinning-related spots accompanying the spots from the FCC lattice. At the same time, the spots' scattering is essentially lower than that in the air-UIT-processed specimen (Fig. 14, b).

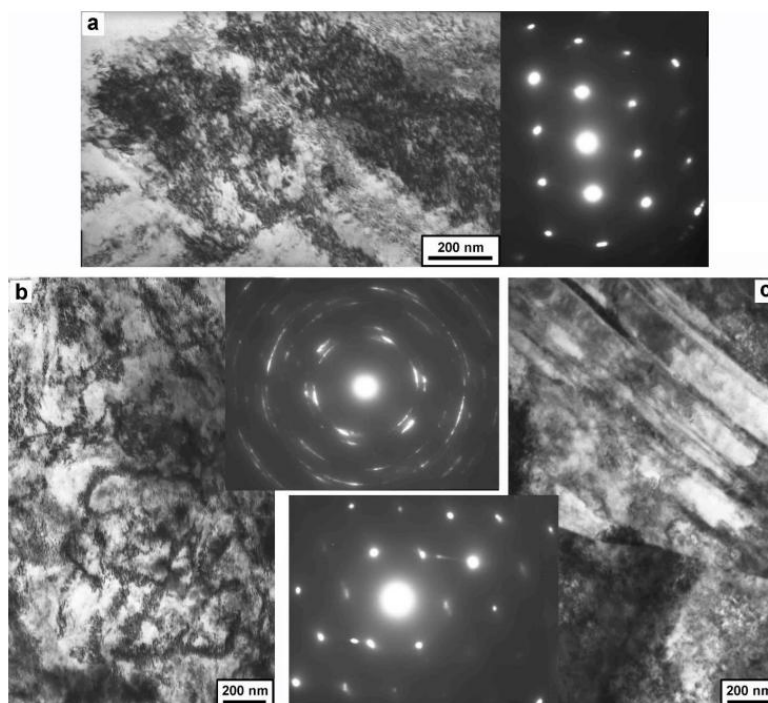


Figure 14. Bright-field TEM images of the microstructure and corresponding SAED patterns of the Cu-37Zn alloy specimens after HESC (18.8%) (a) and the following air-UIT (b) and cryo-UIT (c) processes.

These observations are consistent with the involving deformation mechanisms. Indeed, at cryogenic temperatures, dislocation cross-slip, dynamic recovery, and recrystallization are known to be substantially inhibited due to reduced thermal activation, restricting dislocation mobility. This leads to defect accumulation, which hinders further conventional slip and promotes contribute to the enhancement of deformation twinning. As a result, the brass-type texture is preserved due to the reduced contribution of slip-driven texture evolution.

The investigated Cu-37Zn alloy, like all low-SFE ones, is generally prone to form the brass-type texture via deformation twinning even at room temperature static treatment [5, 113]. Particularly, the deformation-induced texture evolution was discussed for the same Cu37Zn alloy subjected to cold rolling [113], and deformation twinning was concluded to be the main mechanism of the brass-type texture formation. Noteworthy, since the presence of twinning was proven even for the case of static deformation at the ambient temperature, the high-rate low-temperature deformation applied in the present study is much more expected to cause twinning [114].

This result shows the possibility of obtaining the required texture state by choosing the proper combination of the above-mentioned high-rate deformation methods taking the specimen's geometry into account.

Similar UIT regime was applied to Cu-37Zn alloy plates. As described in Chapter 2, plates were isotropic in the initial state and were not subjected to HESC before UIT.

In the Fig. 15, the [111] pole figure for Cu-37Zn alloy plates in the initial state (Fig. 15, a), after cryo-UIT for 20 sec (Fig. 15, b) and for 60 sec (Fig. 15, c) and after air-UIT for 20 sec (Fig. 15, d) and for 60 sec (Fig. 15, e) are shown. It is evident that even after 60 s of air-UIT, a copper-type texture is formed, whereas after only 20 s of cryo-UIT, a brass-type texture has already developed, despite the latter requires higher deformation degrees [46]. Furthermore, the intensity of diffraction lines $\Delta I_{[111]}$ for the same UIT duration is significantly lower after cryo-UIT in comparison to air-UIT. This observation suggests greater texture scattering in the case of cryo-UIT due to more

substantial refinement of the grain structure occurred with the involvement of more deformation mechanisms.

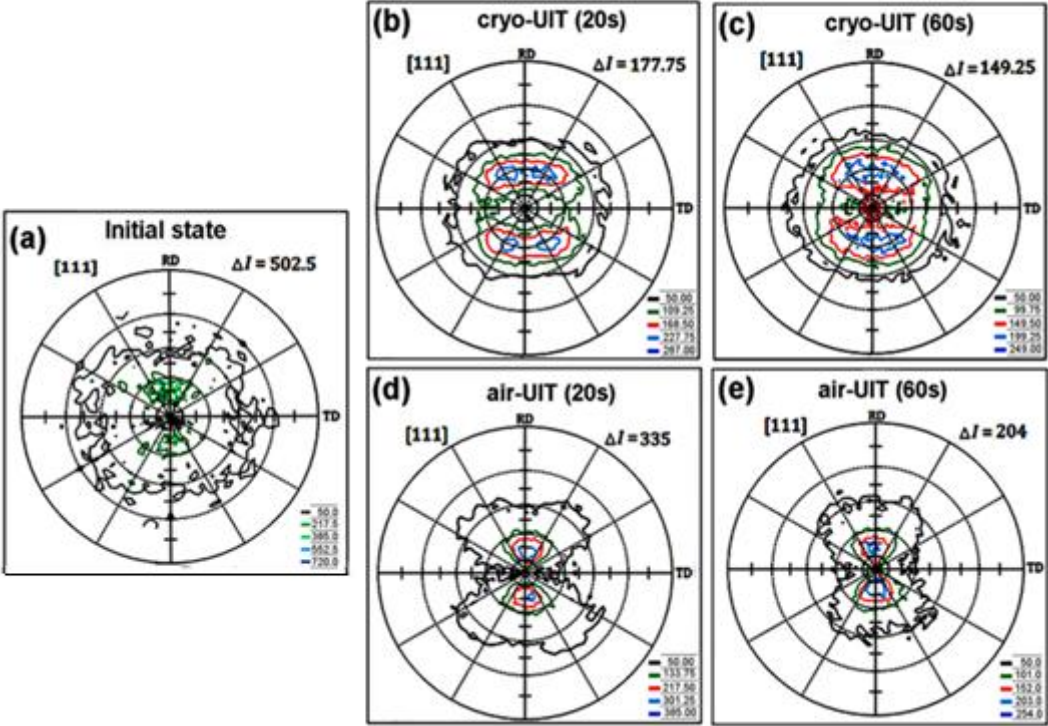


Figure 15. The [111] pole figures characterizing the texture evolution of Cu-37Zn alloy plates in the initial state (a), after cryo-UIT for 20 sec (b) and for 60 sec (c) and after air-UIT for 20 sec (d) and for 60 sec (e)

It can be confirmed by higher accumulated strains after cryo-UIT (Fig. 16) indicating that the Cu-37Zn alloy seems prone to more straining at cryogenic temperatures. This observation correlates to the literature data and was explained by the more intensive deformation twinning in the cryogenic conditions [114].

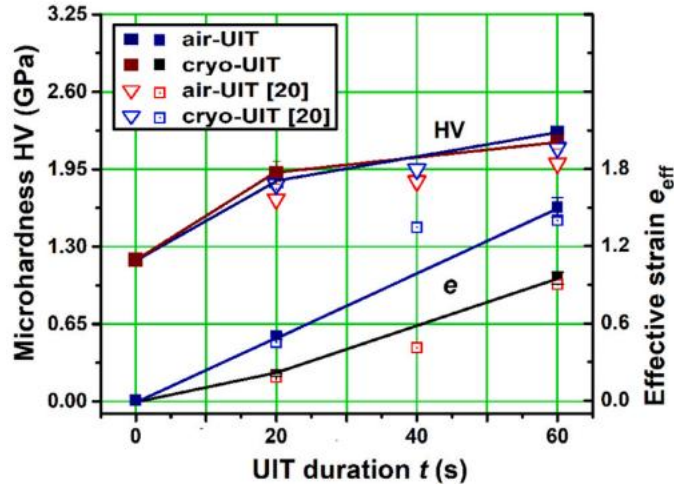


Figure 16. Experimental dependencies of accumulated strain e_{eff} and surface microhardness HV on the UIT process duration.

These findings are substantiated by the results of microstructural analysis of the same specimens, which are presented below (see Fig. 17). XRD pattern (Fig. 17, b1) and EBSD inverse pole figure and image quality maps (Fig. 17, b2) indicate that air-UIT for 20 s increases the fraction of (111) crystallites and reduces those of (200) and (220) in the ND, while also exerting a slight influence on the grain structure in the TD (EBSD). Meanwhile, a similar cryo-UIT regime leads to significant grain structure refinement (Fig. 17, c2), decreases the fractions of (111) and (200) crystallites, and increases the fraction of (220) ones (Fig. 17, c1). The appropriate histograms of grain boundary misorientation angle characterize the grain structure in the initial state and formed after UIT carried out in different temperature regimes. Interesting that the applied deformation scheme results in a significant predominance of the low-angle grain boundaries ($2^\circ < \text{LAGBs} < 15^\circ$) in comparison with the high-angle grain boundaries ($\text{HAGBs} > 15^\circ$). This observation can be explained by the influence of ultrasonic vibrations emitted during the UIT process (the so-called acoustoplastic effect first reported for Zn by Blaha and Langenecker [115]) and will be addressed below. However, the microstructure of the air-UIT-ed specimen contains double HAGBs as compared to that of the cryo-UIT-ed specimen. This should be accounted in the estimation of the grain/subgrain hardening. Analysis of the XRD peak broadening registered for the UIT-processed specimens shows a similar trend regarding the

grain/crystallite size. When compared to the crystallite size determined for the initial specimen ($D \sim 126$ nm), the estimated crystallite size decreased by more than two-fold (~ 54 nm) and slightly less (~ 104 nm) following cryo-UIT and air-UIT, respectively. Notably, an increase in the UIT duration resulted in an even smaller crystallite size (for instance, ~ 41 nm for air-UIT).

The trend observed in EBSD and XRD analyses is corroborated by TEM observations (Fig. 18). The microstructures depicted in Fig. 18 for the investigated Cu-37Zn plate specimens in their initial, air-UIT, and cryo-UIT processed states are supplemented with their corresponding selected-area electron diffraction (SAED). SAED from the bright-field TEM image of the air-UIT processed specimen reveals numerous azimuthally dispersed spots, indicative of high misorientation among the formed cells/crystallites (Fig. 18, d). In the case of cryo-UIT process for 20 s, stacking faults (SFs) and deformation twins (TWs) frequently formed on the SFs intersections, which enhance the material's deformation ability [114], were observed, contributing to the microstructural features of the cryo-UIT processed Cu-37Zn alloy.

The thickness of the twin lamella did not exceed approximately 50–60 nm. Additionally, the intertwining regions exhibit a bimodal microstructure consisting of relatively large (250–500 nm) low-dislocation areas and other regions containing numerous nanoscale dislocation cells (< 10 –20 nm). As observed in the appropriate SAED pattern, new spots from TWs and SFs confirm the appearance of the HCP stacking (ABAB) within the FCC stacking (ABCABC) of the matrix material (Fig. 9b). The obtained results are in good correlation with those literature data reported for the cryogenically strained alloys possessing low SFE and thus prone to the formation of stacking faults, deformation twinning, and shear banding additionally to or instead of the dislocation activity [116-121]. The Cu-Zn alloys containing up to 38 wt% of Zn are single-phase alpha-brasses with fcc lattice and low SFE which decreases with the increase of Zn content [116, 121-123], and SFE of Cu37Zn alloy is lower than 7–14 mJ/m² (reported for Cu30Zn [124-126] and Cu32Zn [116, 121] alloys). Thus, no phase transformations were observed in this study conversely to the recently reported $\alpha \rightarrow \beta$ phase transition in the two-phase Cu-43Zn brass induced by high-strain rate

compression [126]. Further enhancement in twinning can be achieved by using plastic deformation processes applying high strain rates [114, 116-118, 121, 122, 127, 128].

Increasing the duration of the UIT process (60 s) results in a higher accumulated effective strain ($\bar{\epsilon} = 1.04$ for air-UIT and $\bar{\epsilon} = 1.41$ for cryo-UIT) coupled with a significant reduction in grain/crystallite size (Fig. 18, c, f). The microstructure of the cryo-UIT-processed specimen contains a large number of nano-twins and shear bands (SBs) facilitating significant grain/crystallite refinement (Fig. 18, c). A substantial fraction of nanoscale and ultra-fine dislocation cells (25–150 nm) have already formed in the air-UIT-processed specimen (Fig. 18, f). The ring-like SAED patterns are registered for these microstructures formed in the top surface layers of the severely deformed air-UIT and cryo-UIT-processed specimens (Fig. 18, c, f). These newly formed nanograins/nanocells remain highly dislocated, demonstrating their potential for further refinement through secondary subdivision under higher accumulated strains. Formation of nanocrystalline surface layers due to severe plastic deformation is well documented in the literature including for the cases of low-rate straining (ECAP [120]) or high-rate straining, such as dynamic-plastic-deformation [114], surface-mechanical-attrition treatment [123], sand-blasting [129], and the UIT [112, 114]. Moreover, a cryogenic temperature was shown to substantially inhibit the dislocation cross-slip, dynamic recovery, and recrystallization. This naturally promotes grain refinement owing to intersections of multi-system twins or shear bands (see, for instance, the twins' intersections in Fig. 9bcd and highly misoriented nano-scale grains in Fig. 18, c, f).

Regarding the influence of ultrasonic vibrations at the UIT processing, they exert significant effects on the sample together with the multiple high-frequency impact loads. It was shown in [115, 130, 131] that depending on their intensity the ultrasonic vibrations transmitted through the deformed material can result in either strengthening or stress relaxation or both processes simultaneously, due to their effects on the microstructure, i.e., dislocations of both types, vacancies, and subgrain/grain boundaries. Therefore, the UIT processing used in this study is believed to be able to change the involved deformation mechanisms thus promoting the formation of the

unusual copper-type texture in the specimen processed air-UIT for 60 s, i.e., experienced a relatively high strain extent (thickness reductions). Moreover, the air-UIT process seems to result in quick hardening owing to dislocation activity in the top surface layer, which then protects the deeper layers from straining. On the contrary, the cryo-UIT process leads to sequential straining throughout the sample depth to produce much higher overall thickness reduction owing to the involvement of deformation twinning and shear banding, which both lead to formation of brass-type texture. However, TEM observations of the cryo-UIT-ed specimens also confirm the formation of dislocation tangles.

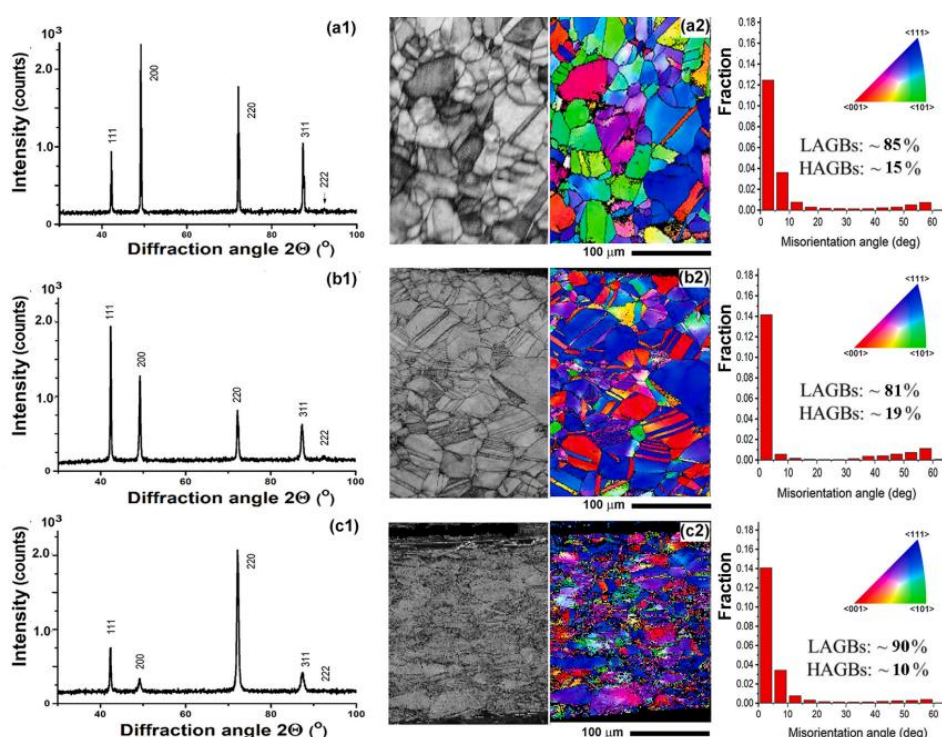


Figure 17. XRD patterns (a1-c1) and EBSD inverse pole figures and quality maps with histograms of GB misorientation angle (a2-c2) of the microstructure of the studied Cu-37Zn plate specimens in the initial state (a1, a2), and after air-UIT for 20 sec (b1, b2) and cryo-UIT for 20 sec (c1, c2)

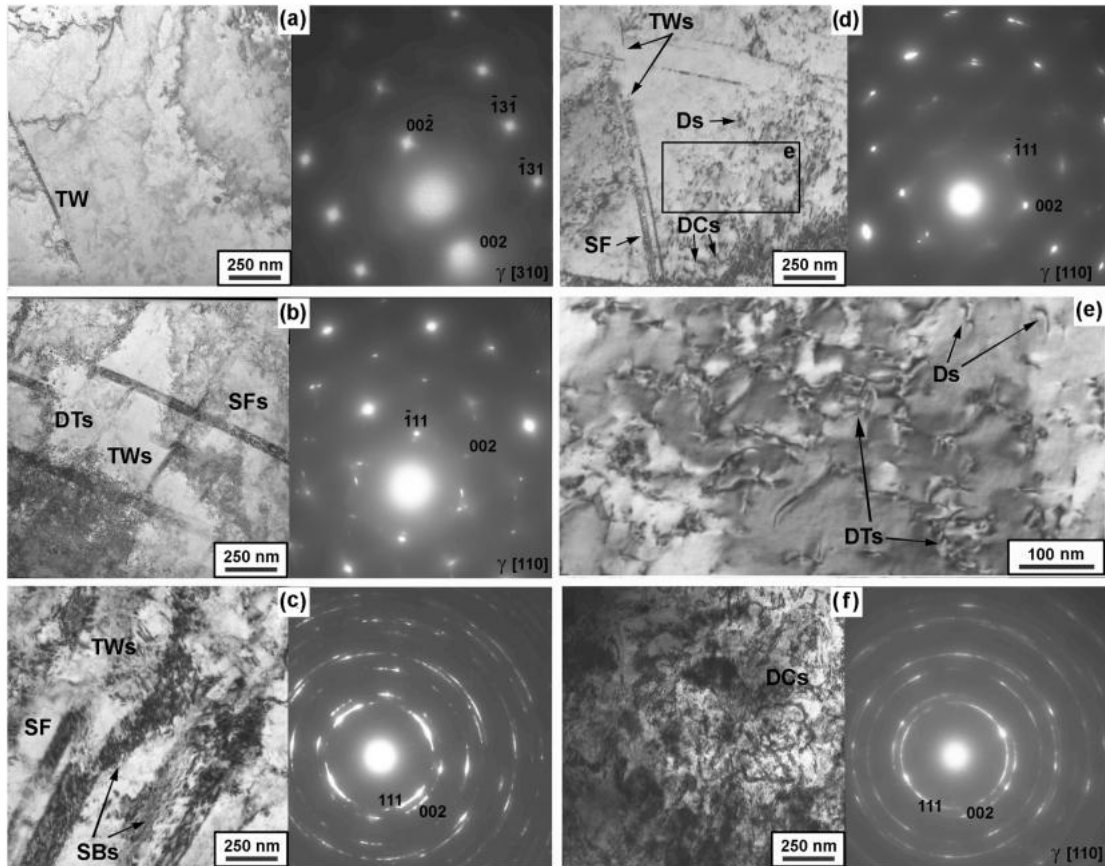


Figure 18. TEM observations supplemented with the SAED patterns of the microstructure of the studied Cu-37Zn plate specimens in the initial state (a) and after cryo-UIT for 20 s (b) and 60 s (c) and air-UIT for 20 s (d, e) and 60 s (f).

It is well-known that texture has a huge influence on the elastic and mechanical properties of the material. Now it will be demonstrated on the investigated Cu-37Zn alloy specimens, both massive and plates.

In order to better understanding the elastic behavior of polycrystalline material and it's dependence of texture state, is important to know the orientation surfaces of the elastic moduli for a single-crystal of this material. The orientation surfaces of the Young modulus (E) and shear modulus (G) of the Cu-37Zn single crystal was reconstructed in this study based on the literature data [132] and shown in Fig. 19.

It is evident that the Young's modulus (E) and shear modulus (G) exhibit extreme opposite values in the [100] and [111] crystallographic directions, while the [110] direction presents intermediate values for E , G . The elastic anisotropy of a polycrystalline aggregate and its changes following directional plastic deformation,

such as UIT, are directly influenced by this aforementioned fact. In this context, the values of elastic parameters and other physical-mechanical characteristics are influenced by the orientation of the entire set of crystallites in the chosen geometric direction. Information about such texture features can be obtained through EBSD and XRD methods. The results obtained using these methods are presented in Figs. 6 and 8. XRD pattern (Fig. 17, b1) and EBSD inverse pole figure and image quality maps (Fig. 17, b2) indicate that air-UIT for 20 s increases the fraction of (111) crystallites and reduces those of (200) and (220) in the ND, which expectedly leads to an increase in E -values in this direction. Meanwhile, a similar cryo-UIT regime leads to decrease the fractions of (111) and (200) crystallites, and increase the fraction of (220) ones (Fig. 17, c1), which also leads to the increase in E , but less than in case of air-UIT-ed specimens.

Regarding other elastic and mechanical properties of investigated brass plates (Fig. 20, b), bulk modulus (B), Poisson's ratio (η), and plasticity characteristic (δ_H) decrease, while G -modulus, and hardness (HV), G/B ratio experience an increase after air-UIT. In a similar UIT-duration, the cryo-UIT process brings an increase in B modulus, although η and δ_H remain largely unaffected. The influence of cryo-UIT on other elastic and mechanical properties is qualitatively similar to air-UIT, albeit slightly weaker (as depicted in Figs. 20 and 21). The impact of air-UIT becomes significantly more pronounced after 60 s of treatment.

At the same time, in case of massive specimens (Fig. 20, a), the E -values increased after air-UIT, and decreased after cryo-UIT (for these specimens the state after HESC is considered now as initial, and in the Fig. 20, a the values for the ND are presented in order to proper comparison with plates-specimens, where it is the only investigated direction). This difference is attributed to the different initial state of massive and plates (textured and isotropic, respectively), and also to the difference in the maximum stresses developed by the 'cumulative impact' and alternating components of the UIT depending specimen's thickness. Considering that E -modulus of massive specimens experiences reorientation after cryo-UIT (Fig. 23, f), namely, the shift of the E -maximum away from the ND direction and its decrease in the RD and

TD directions, its ND-value given in the Fig. 20 is expectedly lower since it is not maximum one any more.

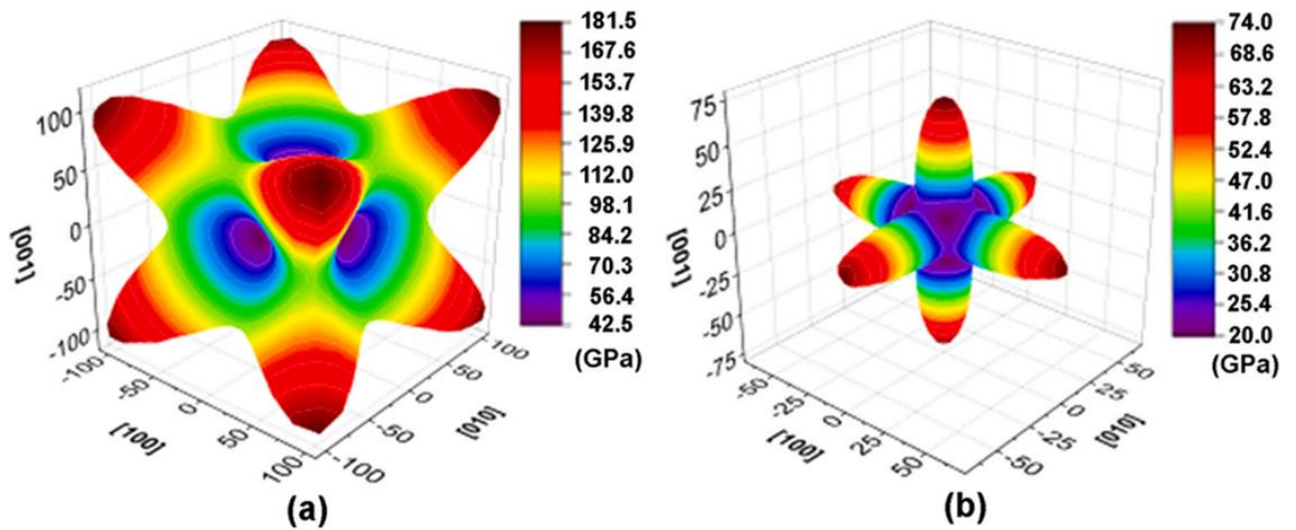


Figure 19. Surfaces of the Young modulus E (a) and shear modulus G (b) for the Cu-37Zn single crystal in the initial state reconstructed based on the literature data regarding the elastic constants [132]: $C_{11} = 131.1$ GPa; $C_{12} = 101.5$ GPa; $C_{44} = 73.8$ GPa, $B = 112.03$ GPa. The magnitudes of E and G in each direction is illustrated not only by color-coding according to each color scale but also by the distance from the center of the three-dimensional space.

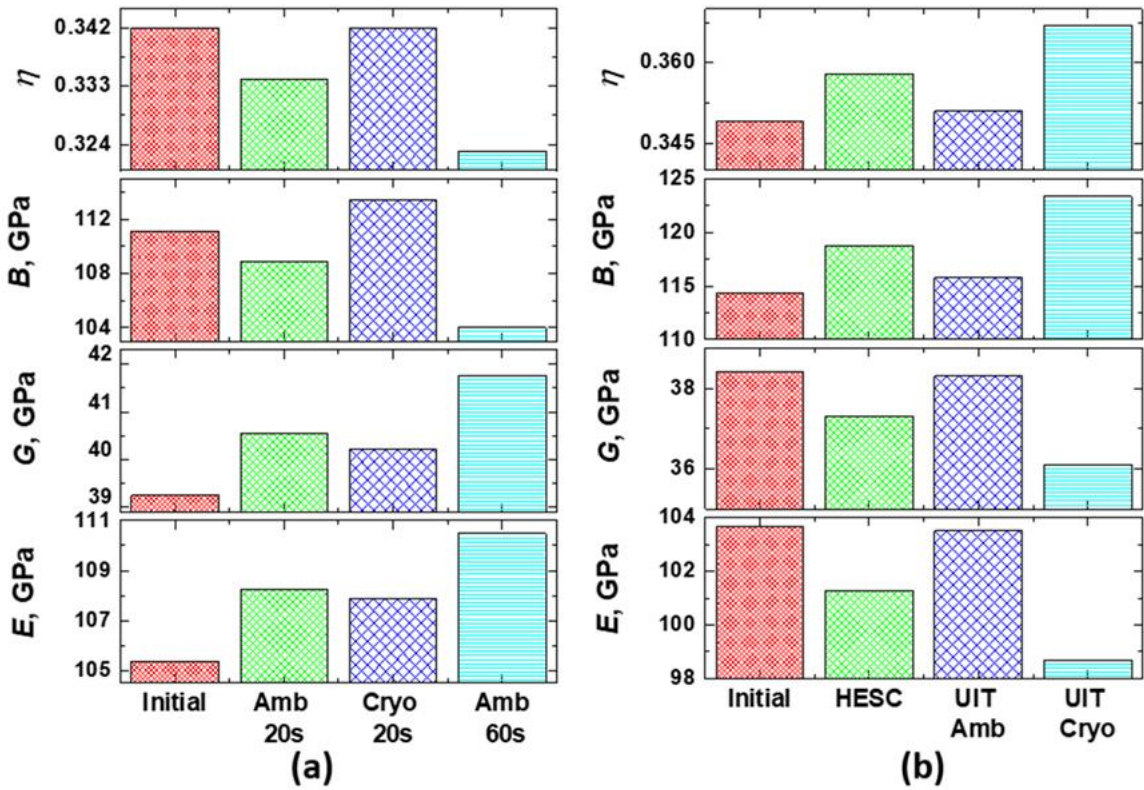


Figure 20. The elastic properties E , G , B , η of Cu-37Zn alloy massive specimens (a) and plates (b)

The effect of the UIT on mechanical properties of massive and plates brass specimens is qualitatively similar (Fig. 21), despite that it differs in case of elastic properties. The behavior of both EP and mechanical properties of massive specimens is more complex because of thickness, but as well this is the clear sign, that the mechanical properties depend not only on E modulus, but on the whole complex of EP pf the material. It should be noted that in terms of hardening of the investigated Cu-37Zn alloy specimens, the obtained results do not demonstrate any advantages of cryo-UIT at the applied regimes as compared to the air-UIT.

Various hardening mechanisms can be suggested to give a more precise explanation of the hardness behavior and to compose some kind of a general expression describing the hardening process [99]. First of all, Taylor's term of hardening should be included in a general hardening law. In the well-known expression based on the reciprocal square root of dislocation density ρ , other parameters (constant $\alpha \approx 0.2-1$, Taylor constant M , shear modulus G , and Burgers' vector b) should be chosen accordingly for γ and α' phases: $\Delta\sigma = \alpha M G b \rho^{-1/2}$. Further, a couple of terms of the

Hall-Petch type should be taken into account. Firstly, this well-known law of the reciprocal square root of the grain size D_g : $\Delta\sigma = \sigma_0 + K_1 D_g^{-1/2}$. Additionally, the dislocation cells (subgrains) are also an effective hardening factor, which should be taken into account for the argon-UIT processed specimens by applying the term with the reciprocal cell size D_c : $\Delta\sigma = K_3 D_c^{-1}$. Considering the EBSD data indicating the predominance of the LAGBs in the formed microstructure (Fig. 8c1-c3), it would be more appropriate to use the reciprocal grain size to make the estimations of the hardening instead of the standard Hall-Petch relation. The contribution of deformation twins to yield stress should be supplemented with a similar term corresponding to the inter-twin spacings: $\Delta\sigma = K_2 \Lambda^{-1/2}$. Then, using the appropriate material's constants and the well-known Tabor's relation connecting the yield stress and hardness of the material ($H \approx 3\sigma_Y$) a general expression describing hardness can be written by aggregation of the appropriate terms from the above-described list.

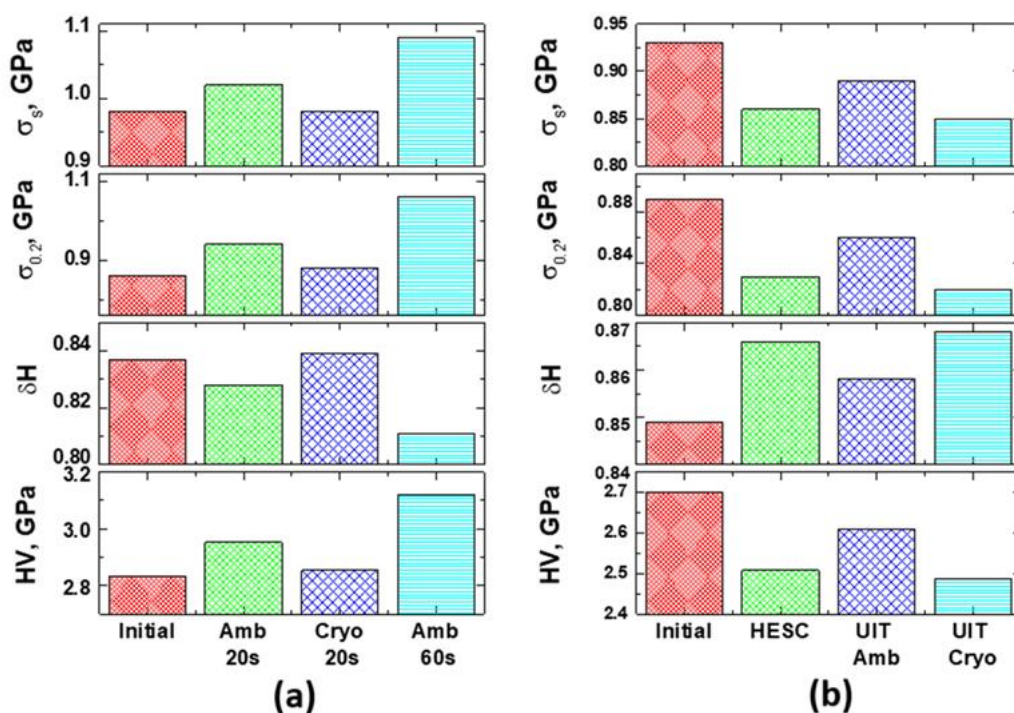


Figure 21. The main mechanical properties, namely Vicker's hardness H_v , plasticity parameter ΔH , yield ($\sigma_{0.2}$) and strength (σ_s) stresses of Cu-37Zn alloy massive specimens (a) and plates (b)

For the massive specimens USTA allows to analyze elastic and related

mechanical properties layer-by-layer in different geometric directions, which is of significant importance for production purposes. Such analysis for Cu-37Zn alloy massive specimens is given below.

In the Fig. 22, the 3D-surface of Young's modulus (Fig. 22, a), its values in orthogonal directions (Fig. 22, b), its extreme values (Fig. 22, c) and the anisotropy of Young's modulus (Fig. 22, d) after HESC are shown. As it is clear (Fig. 22, a) Young modulus is strongly anisotropic and its maximum is in the TD (Fig. 22, b). All of directional Young's moduli decrease after the first step of HESC and after the second step, E_1 is still almost the same as the initial state, but E_2 and E_3 increase significantly. It is probably caused by the establishment of crystallographic directions of maximum Young's modulus parallel to TD and ND indicated by increasing of the intensity maximums in PF (111) (Fig. 10) along with the increase of $\Delta I_{(111)}$ (Fig. 11).

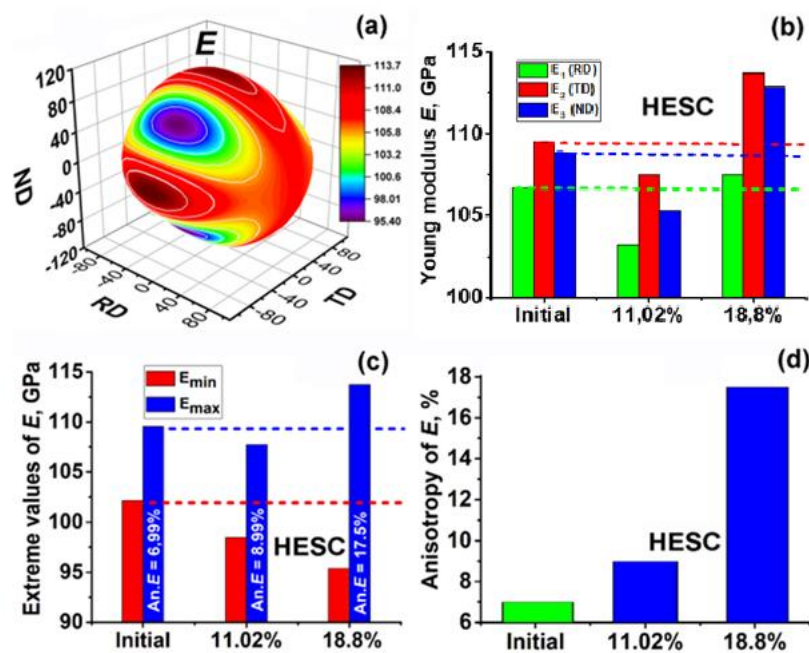


Figure 22. Young modulus of Cu-37Zn alloy after HESC: (a) the 3D-surface for HESC-processed (18.8%) specimen, (b) the values in the orthogonal directions ND, TD, RD, (c) the extreme values, (d) the anisotropy of Young's modulus.

In the Fig. 23 the 3d-surface of Young's modulus, its values in orthogonal directions and the extreme ones, and the anisotropy of E after air-UIT (Fig. 23, a-d)

and cryo-UIT (Fig. 23, e-h) are shown. In the first column of each graph the values after HESC to $\varepsilon = 18.8\%$ are shown.

Young's modulus after air-UIT is still anisotropic (Fig. 23, a) and its values in RD are also still smaller than the other for all examined sections (Fig. 23, b). We can also observe a gradual decrease in E-values in all orthogonal directions from TS to BS. The anisotropy of Young's modulus decreases twice after both cryo- and air-UIT (Fig. 23, c, g). However, after cryo-UIT there are no texture changes, in contrast to the air-UIT. So, this difference cannot be associated with texture transitions, but is probably caused by the increase in the grain boundary fraction as a result of grain refinement [133] which is usual in the case of high rate and/or cryogenic deformation [98, 114, 116, 122, 134].

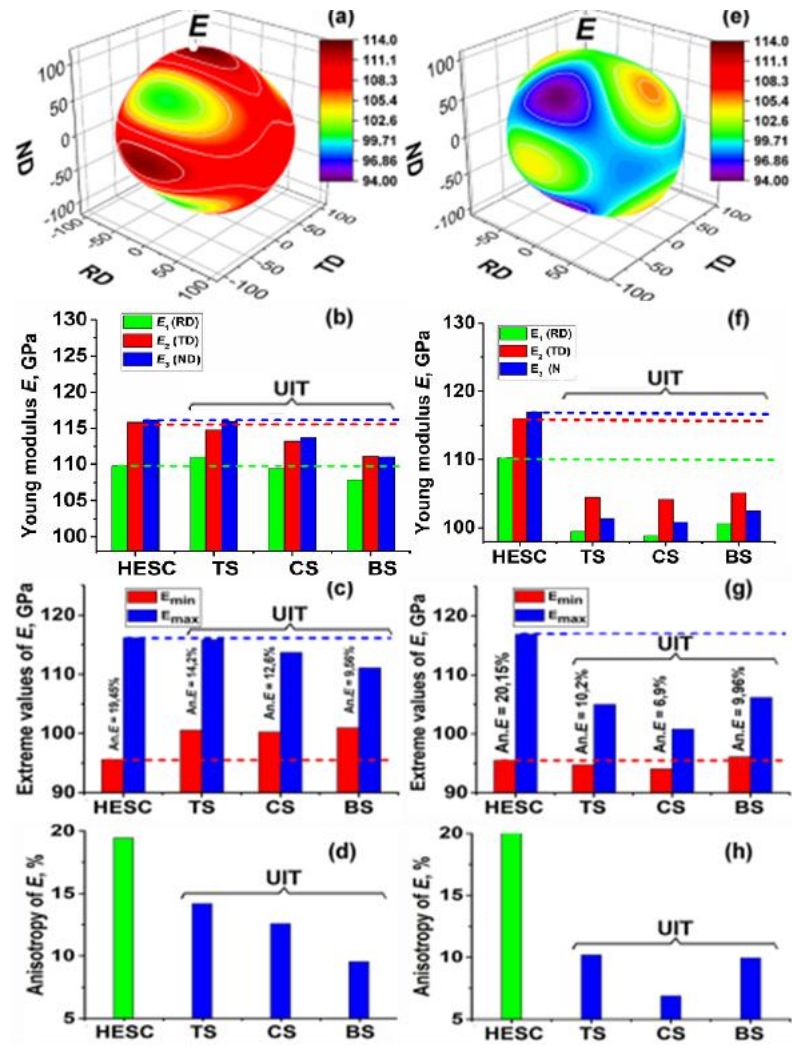


Figure 23. 3D-surfaces of Young's modulus E (a, e), its values in orthogonal directions (b, f) and the extreme ones (c, g), and the anisotropy of E (d, h) for various sections of specimens after air-UIT (a–d) and cryo-UIT (e–h) in comparison with those after HESC.

In the Fig. 24 the values of shear modulus and Poisson ratio in the orthogonal planes TD-ND ($G_{2,3}$ and $\eta_{2,3}$), RD-ND ($G_{1,3}$ and $\eta_{1,3}$) and RD-TD ($G_{1,2}$ and $\eta_{1,2}$) after all steps of treatment are shown.

Shear modulus after final step of HESC decreases the most significantly in the TD-ND plane (Fig. 24, a) and Poisson ratio correspondingly increases in similar plane (Fig. 24, b). There are no significant changes in the other orthogonal planes.

Considering that after air-UIT (Fig.24, c, d) $G_{2,3}$ and $\eta_{2,3}$ return practically to the level of their initial state, it can be assumed that this is associated, respectively, with the direct copper-brass and reverse of brass-copper texture transitions.

After cryo-UIT (Fig.24, e, f), in return, changes are in the RD-TD plane, which possibly indicates partly transition to a new deformation mechanism. This can be confirmed by drastic changes in Young modulus extreme values and deviation of its maximum from ND. While setting the directions as $\langle 111 \rangle \parallel \text{ND}$, the $\langle 112 \rangle$ directions are set into the rolling plane, and the $\{111\}$ plane is set parallel to it. Such reorientation is usual for FCC-metals during compressive deformation, including multiple shock compression during UIT [96]. Taking this into account, twinning $\{111\}\langle 112 \rangle$ seems to be a possible new deformation mechanism because this twinning system is characteristic of FCC-alloys [135].

In the Fig. 25 the calculated Vickers Hardness HV (Fig.25, a-c) and Milman's plasticity characteristic δ_H (Fig.25, d-f) of the specimens after each step of treatment are shown.

As seen, there is a slight decrease in HV values in all orthogonal directions after the first step of HESC (11.2%) and a return to the initial level (the RD-value) and even additional hardening (ND- and TD) compared to the initial level after the second HESC step. This result correlates well with the observed changes in the crystallographic texture type and intensity (Fig.3, Fig.4). The following UIT-induced changes are observed to vary greatly depending on the applied temperature (Fig. 11, c, e, d, f), as like as in the case of elastic properties (Fig.9, Fig.10).

After air-UIT, the HV values appear close to that observed after the second HESC step, especially for the ND and TD directions. However, it achieves its maximum in the RD direction, increasing gradually from TS to CS and BS. In contrast, after cryoUIT, the HV values become significantly lower than those after HESC. Additionally, they become equal across the ND, RD, and TD directions, i.e., demonstrating a negligible anisotropy. Since HV is mathematically dependent on elastic moduli (Eq. 14), these changes can be attributed to the shift of the E-maximum away from the ND direction and its decrease in the RD and TD directions (see Fig. 9f).

The corresponding changes in the Milman's plasticity characteristic, δH , exhibit the opposite trend according to Eq. 15.

As in the Cu-37Zn plates analyzed in the previous study [3], the massive samples showed virtually no changes in all investigated mechanical characteristics after cryo-UIT. Therefore, considering the material hardening, this cryogenic treatment has no advantages over air-UIT.

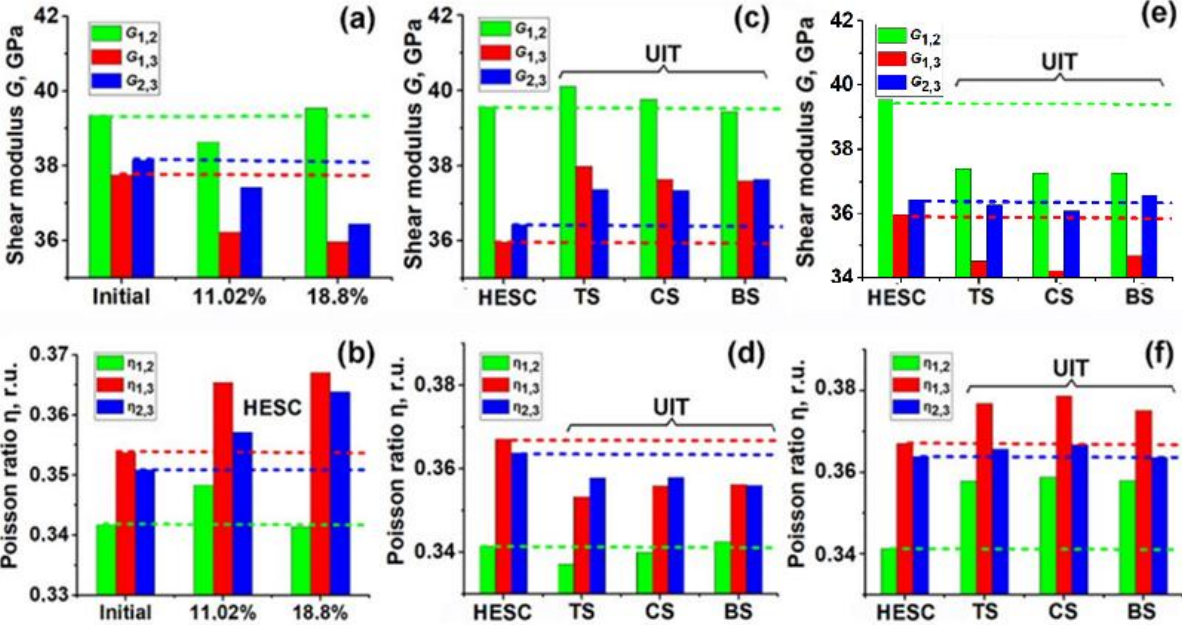


Figure 24. The values of shear modulus (a, c, e) and Poisson ratio (b, d, f) in the orthogonal planes for in the initial state, after HESC (a, b), and for various sections of specimens after air-UIT (c, d), and cryo-UIT (e, f).

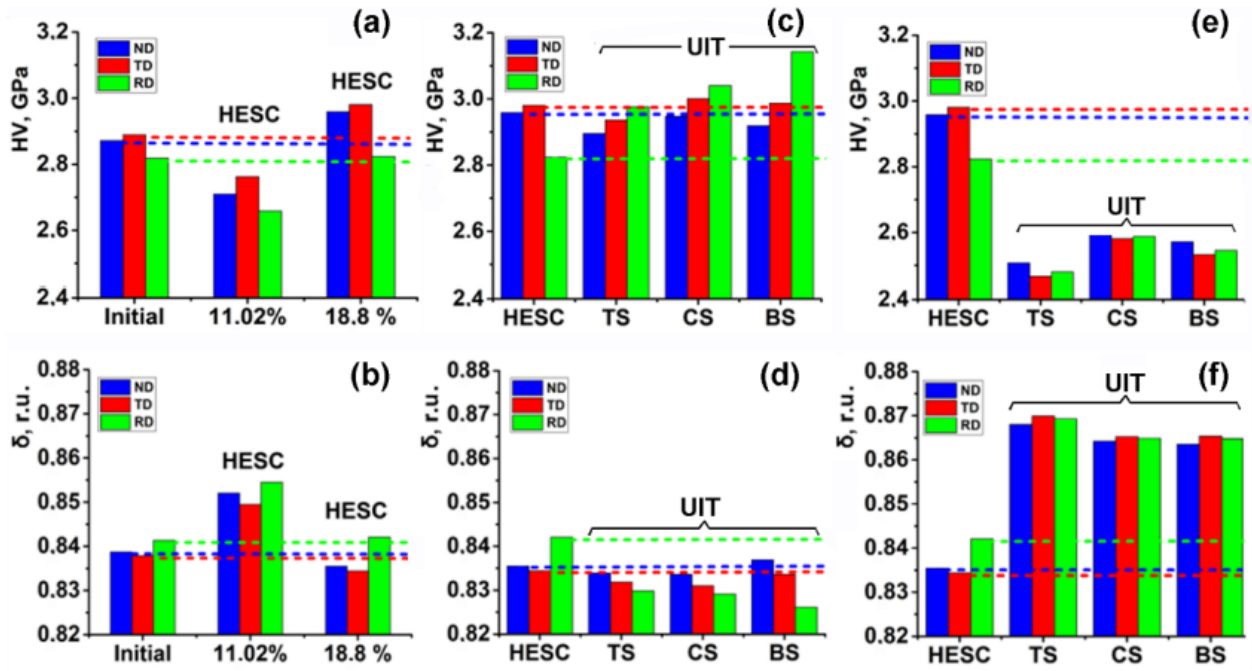


Figure 25. The values of Vickers hardness HV (a, c, e) and Milman's plasticity characteristics δ_H (b, d, f) in the orthogonal directions for the initial state and HESC (a, b), air-UIT (c, d), and cryo-UIT (e, f).

Conclusions for this subsection are as following:

- 1) HESC of massive specimens of Cu-37Zn alloy leads to copper-brass crystallographic transition even at $\varepsilon = 11,02\%$. At $\varepsilon = 18,8\%$ the brass-type texture becomes sharper. This effect is typical in case of high-rate directional compressive deformation of such alloys.
- 2) An unusual brass-copper texture transition was detected in the air-UIT processed brass specimens with a HESC pre-formed texture. The absence of this texture transition after cryo-UIT process of similar parameters is explained by the difference in the mechanisms of plastic deformation, i.e., dislocation activity at room temperature that was enhanced by the alternating component of UIT, and twinning at cryogenic temperature.
- 3) There are no texture-type changes after cryo-UIT, which is explained by suppressing the movement of defects, accumulation of defects and further complication of dislocation slip and the enhanced twinning, which, in turn, leads to the preservation of brass-type texture.

- 4) After HESC the significant increasing in Young's modulus anisotropy and its ND- and TD-values were revealed. This is probably associated with reorientation of crystallographic $\langle 111 \rangle$ directions corresponding to maximum E values along ND and TD.
- 5) Combination of HESC+UIT both at ambient and cryogenic temperature leads to almost twice decreasing of elastic anisotropy of the alloy. This is probably caused by the increasing of grain boundary fraction as a result of grain refinement which is usual in the case of high rate and/or cryogenic deformation.
- 6) There are changes of shear modulus G and Poisson ratio η after cryo-UIT in RD-TD plane, while in the case of air-UIT these changes were observed in ND-TD plane. This may indicate a partial transition to another deformation mechanism, namely twinning.
- 7) The observed correlation between the texture and elastic properties of the studied specimens indicates that the texture change is the main factor affecting the elastic moduli variations in the Cu-37Zn brass specimens that underwent the applied treatments.
- 8) Results show that the required texture and elasticity of the material state can be obtained by choosing the proper combination of the above-mentioned high-rate deformation methods.
- 9) As for plates, a greater texture scattering and the brass-type texture formation in the case of cryo-UIT, attributed to a more substantial refinement of the grain structure. Thus, the copper-type texture is formed after air-UIT and the brass-type texture is formed after cryo-UIT. The cryo-UIT processed specimen was confirmed to experience intensive twinning and further shear-banding, which are known to promote the brass-type texture. On the contrary, the microstructure registered after air-UIT contains mainly dislocation tangles and bundles that transform into dislocation nano-cells with the increase in the thickness reduction and facilitate the copper-type texture.
- 10) The difference between the influence of the UIT on the texture formation process in massive specimens and plates is explained by the different the

maximum stresses developed by the cumulative and alternating components in those kinds of specimens.

3.2 The influence of chemical composition and ultrasonic impact treatment on the elastic and the main mechanical properties of 51Ti31Zr10Nb8Ta, 31Ti51Zr10Nb8Ta, 51Ti31Zr18Nb, 31Ti51Zr18Nb medical alloys

In this subsection the influence of chemical composition and UIT on the elastic and related mechanical properties of four medical 51Ti31Zr10Nb8Ta, 31Ti51Zr10Nb8Ta, 51Ti31Zr18Nb, 31Ti51Zr18Nb alloys in the initial state and after UIT will be discussed. The Ti-Zr alloy specimens in the form of massive and plates ones were studied.

In the table 2 the values of parameters characterizing the collective behavior of the components of the investigated alloys are presented. These values were calculated using expressions presented in [136]. The data for the equiatomic alloy TiZrNbTa are provided for comparison in the rightmost column.

Element, %	Atomic radius, nm	Alloy				
		1	2	3	4 ZTNT	5 TZNT
Ti	0.1462	51	51	31	31	-
Zr	0.1603	31	31	51	51	-
Nb	0.1429	18	10	18	10	-
Ta	0.1430	0	8	0	8	-
Atomic incompatibility δ	-	4.68	4.68	5.06	5.06	4.8
Mixing enthalpy Δh_{mix}	-	1.63	1.36	1.92	1.65	2.5
Mixing entropy ΔS_{mix}	-	8.44	9.47	8.44	9.47	-
Pauling electronegativity $\Delta\chi$	-	0.14	0.13	0.17	0.16	-
Valent electron concentration VEC	-	4.18	4.18	4.18	4.18	4.5
$\Omega(\Delta S_{\text{mix}}, \Delta H_{\text{mix}})$	-	11.25	15.35	9.82	13.01	11.628

It is evident that the VEC for the investigated alloys is 4.18. This value is optimal for minimizing the Young's modulus of multicomponent alloys [137]. Along with it, according to study [54] the VEC = 4.18 corresponds to one of the highest values of

universal anisotropy index (A_u), and VEC of equiatomic alloy, in contrast, indicates much lower anisotropy.

Increasing the concentration of Zr by replacing with Ti leads to an increase in atomic incompatibility (δ) from 4.68% to 5.06%, and the partial replacement of Ta atoms with Nb reduces the enthalpy (Δh_{mix}) and increases the entropy (Δs_{mix}) of mixing.

A higher Zr content leads to an increase in hardness, E - and G -moduli, the G/B parameter, and reduced Poisson's ratio and plasticity characteristics δ_H (see Table 2). Collectively, this indicates that an increase in Zr content, along with the corresponding rise in (δ), leads to alloy strengthening. At the same time, the effect of Ta on these properties depends on the initial Ti and Zr content. For instance, the Ta-containing alloy 2TZNT has a lower Young's modulus (and related parameters) compared to the 1TZN alloy, whereas the Young's modulus of the 4ZTNT alloy is higher than that of the corresponding ternary alloy 3ZTN. A corresponding increase in Debye Temperature TD with increasing Zr-content and its decrease after Ta-addition indicates, respectively, increase and decrease in interatomic interaction forces in the investigated alloys, which correlates well with E -modulus changes.

Alloy	Debye temperature TD	E, GPa	G, GPa	B, GPa	η	G/B	HV, GPa	δ_H
1TZN	283,17852	83,34	30,55	102,00	0,364	0,3	2,63	0,832
2TZNT	265,05467	80,60	29,41	103,44	0,370	0,28	2,413	0,848
3ZTN	292,05992	89,65	33,41	94,24	0,341	0,35	3,394	0,770
4ZTNT	282,25338	91,42	34,23	92,49	0,335	0,37	3,626	0,750

The same trend applies to the anisotropy of all investigated elastic and mechanical properties, which, in their initial state, are significantly higher in Ta-containing alloys. In particular, for alloy 2TZNT, $\Delta E/\langle E \rangle$, $\Delta G/\langle G \rangle$, and $\Delta B/\langle B \rangle$ are higher than for the 1TZN alloy, while the anisotropy of 4ZTNT is less than for 3ZTN one. Note that this trend is applicable for different geometric directions (see Table 3).

The effect of partial Nb substitution for Ta may be associated with an increase in α -martensite inclusions in the β -phase alloy [138] and changes in the distribution of dendritic structures in the alloys [41].

Table 4. Elastic parameters (E , G , B , η , and G/B) and mechanical properties (HV , δ_H , $\sigma_{0.2}$, σ_S), their average values $\langle X \rangle$, heterogeneity ($\Delta X/\langle X \rangle$, indicated as $\langle X_{i-j} \rangle$) and anisotropy ($An.i-j$) for three directions of massive TiZrNb and TiZrNbTa alloys before UIT

Alloy	Parameter	E , GPa	G , GPa	B , GPa	η	G/B	HV , GPa	δ_H , r.u.	$\sigma_{0.2}$, GPa	σ_S , GPa
1TZN	$\langle RD \rangle$	85.11	31.28	101.70	0.360	0.31	2,755	0,824	0,91	0,99
	$\langle TD \rangle$	80.79	29.51	102.83	0.369	0.29	2,444	0,845	0,81	0,87
	$\langle ND \rangle$	84.47	31.05	100.69	0.360	0.31	2,749	0,823	0,91	0,99
	$\langle X \rangle$	83.45	30.61	101.75	0.363	0.30	2,65	0,83	0,88	0,95
	$\langle X3-2 \rangle$	82.63	30.27	101.76	0.365	0.30	2,60	0,83	0,86	0,93
	$\langle X3-1 \rangle$	84.79	31.16	101.20	0.360	0.31	2,75	0,82	0,91	0,99
	$\langle X2-1 \rangle$	82.81	30.33	102.36	0.365	0.30	2,60	0,83	0,86	0,93
	An.3-2,	4.45	5.09	2.10	2.47	6.67	-11,96	2,52	-11,63	-12,90
	An.3-1,	0.75	0.74	1.00	0.00	0.00	-0,22	-0,12	0,00	0,00
An.2-1,	5.20	5.82	1.10	2.47	6.67	11,75	-2,64	11,63	12,90	
2TZNT	$\langle X1 \rangle$	77.50	28.14	104.93	0.377	0.27	2,188	0,863	0,72	0,77
	$\langle X2 \rangle$	83.26	30.52	102.05	0.364	0.30	2,624	0,833	0,87	0,94
	$\langle X3 \rangle$	86.04	31.69	100.65	0.357	0.31	2,856	0,816	0,94	1,03
	$\langle X \rangle$	82.26	30.10	102.57	0.366	0.29	2,56	0,84	0,84	0,91
	$\langle X3-2 \rangle$	84.65	31.10	101.35	0.361	0.31	2,41	0,85	0,80	0,86
	$\langle X3-1 \rangle$	81.74	29.89	102.82	0.367	0.29	2,52	0,84	0,83	0,90
	$\langle X2-1 \rangle$	80.37	29.32	103.50	0.371	0.28	2,74	0,82	0,91	0,99
	An.3-2,	3.28	3.76	1.38	1.94	3.28	18,12	-3,54	18,87	19,88
	An.3-1,	10.44	11.87	4.16	5.45	13.79	26,49	-5,60	26,51	28,89
An.2-1,	7.17	8.11	2.78	3.51	10.53	8,47	-2,06	7,73	9,14	
3ZTN	$\langle X1 \rangle$	94.39	35.63	89.70	0.325	0.40	4,042	0,716	1,33	1,54
	$\langle X2 \rangle$	87.10	32.25	97.03	0.350	0.33	3,075	0,796	1,01	1,13
	$\langle X3 \rangle$	80.58	29.50	100.05	0.366	0.29	2,520	0,836	0,83	0,90
	$\langle X \rangle$	87.36	32.41	95.66	0.348	0.34	3,21	0,78	1,06	1,19
	$\langle X3-2 \rangle$	83.83	30.86	98.56	0.358	0.31	3,56	0,76	1,17	1,34
	$\langle X3-1 \rangle$	87.49	32.49	94.97	0.346	0.34	3,28	0,78	1,08	1,22
	$\langle X2-1 \rangle$	90.77	33.92	93.39	0.338	0.36	2,80	0,82	0,92	1,02
	An.3-2,	7.78	8.91	3.06	4.47	12.90	-27,17	10,58	-27,35	-30,71
	An.3-1,	15.79	18.82	10.91	11.87	31.88	-46,39	15,46	-46,30	-52,46
An.2-1,	8.03	9.96	7.85	7.41	19.18	-19,84	4,90	-19,57	-22,66	
4ZTNT	$\langle X1 \rangle$	91.73	34.38	92.19	0.334	0.37	3,667	0,747	1,21	1,38
	$\langle X2 \rangle$	92.00	34.45	93.11	0.335	0.37	3,640	0,751	1,20	1,37
	$\langle X3 \rangle$	92.06	34.67	89.09	0.328	0.39	3,872	0,725	1,28	1,47
	$\langle X \rangle$	91.93	34.50	91.46	0.332	0.38	3,73	0,74	1,23	1,41
	$\langle X3-2 \rangle$	92.03	34.56	91.09	0.332	0.38	3,65	0,75	1,21	1,38
	$\langle X3-1 \rangle$	91.90	34.52	90.64	0.331	0.38	3,77	0,74	1,25	1,43
	$\langle X2-1 \rangle$	91.86	34.41	92.65	0.335	0.37	3,76	0,74	1,24	1,42
	An.3-2,	0.06	0.64	4.41	2.11	5.26	-0,74	0,53	-0,83	-0,73
	An.3-1,	0.36	0.84	3.42	1.81	5.26	5,44	-2,99	5,62	6,32
An.2-1,	0.29	0.20	0.99	0.30	0.00	6,18	-3,52	6,45	7,04	

The UIT of massive specimens in the applied regime primarily leads to only slight residual compression (up to 0.1-0.14%) in the deformation direction, which can

be explained by the unattainability of the yield strength ($\sigma_{0.2}$) of the alloys during processing due to the absence of macroscopic stresses (σ_A). However, due to the alternating component of deformation during UIT, the moduli E , G , the G/B ratio, and HV decrease significantly, while the modulus B , Poisson's ratio, and plasticity parameter δ_H increase (see Table 4). The UIT in most cases is seen to decrease spatial inhomogeneity ($\Delta X / \langle X \rangle$) and anisotropy (An_{i-j}) of the specimens, including ones in different geometric directions. It is clearly possible to choose the E -minimum direction in order to fit the requirements for such alloys. Choosing between examined alloys, the 2TZNT alloy has lowest Young's modulus in the ND after UIT (74,64 GPa). Along with it, the 4TZNT alloy has the lowest anisotropy of E , but the E -values itself are a little higher. So that it is necessary to choose more important parameter in each case.

The results demonstrate the potential of UIT for reducing the anisotropy and heterogeneity of the elastic and mechanical properties of Ti-Zr-based biomedical alloys, as well as for decreasing the absolute values of their Young's modulus.

Table 5. Elastic parameters (E, G, B, η , and G/B) and mechanical properties (HV, δ_H , $\sigma_{0.2}$, σ_S) their average values $\langle X \rangle$, heterogeneity ($\Delta X / \langle X \rangle$, indicated as $\langle X_{i-j} \rangle$) and anisotropy (An.i-j) for three directions of massive TiZrNb and TiZrNbTa alloys after UIT

Alloy	Parameter	E, GPa	G, GPa	B, GPa	η	G/B	HV, GPa	δ_H , r.u.	$\sigma_{0.2}$, GPa	σ_S , GPa
1TZN	$\langle X1 \rangle$	79,18	28,86	103,00	0,372	0,280	2,341	0,851	0,77	0,83
	$\langle X2 \rangle$	79,86	29,15	102,15	0,370	0,285	2,408	0,846	0,79	0,85
	$\langle X3 \rangle$	83,41	30,55	102,96	0,365	0,297	2,602	0,836	0,86	0,93
	$\langle X \rangle$	80,82	29,52	102,70	0,37	0,29	2,45	0,84	0,81	0,87
	$\langle X3-2 \rangle$	79,52	29,01	102,57	0,37	0,28	2,37	0,85	0,78	0,84
	$\langle X3-1 \rangle$	81,30	29,71	102,98	0,37	0,29	2,47	0,84	0,82	0,88
	$\langle X2-1 \rangle$	81,64	29,85	102,56	0,37	0,29	2,51	0,84	0,83	0,89
	An.3-2, %	0,86	1,02	-0,83	-0,59	1,85	2,82	-0,62	2,82	3,23
	An.3-1, %	5,20	5,70	-0,03	-1,87	5,74	10,55	-1,87	10,55	11,66
An.2-1, %	4,34	4,69	0,80	-1,28	3,89	7,74	-1,25	7,74	8,44	
2TZNT	$\langle X1 \rangle$	81,63	29,88	101,41	0,366	0,295	2,541	0,837	0,84	0,91
	$\langle X2 \rangle$	79,64	29,01	104,44	0,373	0,278	2,326	0,854	0,77	0,82
	$\langle X3 \rangle$	74,64	26,99	105,84	0,382	0,255	2,007	0,875	0,66	0,69
	$\langle X \rangle$	78,64	28,63	103,90	0,37	0,28	2,29	0,86	0,76	0,81
	$\langle X3-2 \rangle$	80,64	29,44	102,93	0,37	0,29	2,43	0,85	0,80	0,86
	$\langle X3-1 \rangle$	78,13	28,44	103,63	0,37	0,27	2,27	0,86	0,75	0,80
	$\langle X2-1 \rangle$	77,14	28,00	105,14	0,38	0,27	2,17	0,86	0,71	0,76
	An.3-2, %	-2,47	-2,98	2,94	1,91	-5,93	-8,84	2,06	-8,84	-10,17
	An.3-1, %	-8,95	-10,16	4,27	4,44	-14,41	-23,50	4,46	-23,50	-26,47
An.2-1, %	-6,49	-7,18	1,33	2,53	-8,51	-14,74	2,40	-14,74	-16,41	
3ZTN	$\langle X1 \rangle$	84,77	31,29	97,26	0,355	0,322	2,901	0,807	0,96	1,06
	$\langle X2 \rangle$	85,08	31,48	95,26	0,351	0,330	3,004	0,797	0,99	1,10
	$\langle X3 \rangle$	86,08	31,95	93,77	0,347	0,341	3,143	0,785	1,04	1,16
	$\langle X \rangle$	85,31	31,57	95,43	0,35	0,33	3,02	0,80	1,00	1,11
	$\langle X3-2 \rangle$	84,93	31,39	96,26	0,35	0,33	2,95	0,80	0,97	1,08
	$\langle X3-1 \rangle$	85,43	31,62	95,52	0,35	0,33	3,02	0,80	1,00	1,11
	$\langle X2-1 \rangle$	85,58	31,72	94,52	0,35	0,34	3,07	0,79	1,01	1,13
	An.3-2, %	0,36	0,62	-2,08	-1,01	2,70	3,51	-1,31	3,51	4,18
	An.3-1, %	1,17	1,48	-1,55	-1,18	3,09	4,59	-1,52	4,59	5,33
An.2-1, %	-0,90	-1,19	1,75	1,13	-2,91	-4,13	1,46	-4,13	-4,81	
4ZTNT	$\langle X1 \rangle$	85,24	31,72	85,24	0,344	0,349	3,216	0,773	1,06	1,20
	$\langle X2 \rangle$	87,31	32,44	87,31	0,346	0,344	3,212	0,781	1,06	1,19
	$\langle X3 \rangle$	87,58	32,51	87,58	0,347	0,341	3,179	0,786	1,05	1,17
	$\langle X \rangle$	86,71	32,22	86,71	0,35	0,34	3,20	0,78	1,06	1,19
	$\langle X3-2 \rangle$	86,27	32,08	86,27	0,34	0,35	3,21	0,78	1,06	1,19
	$\langle X3-1 \rangle$	86,41	32,11	86,41	0,35	0,34	3,20	0,78	1,06	1,18
	$\langle X2-1 \rangle$	87,44	32,47	87,44	0,35	0,34	3,20	0,78	1,05	1,18
	AH.3-2, %	2,40	2,24	2,40	0,61	-1,51	-0,13	1,07	-0,13	-0,68
	AH.3-1, %	2,71	2,45	2,71	1,02	-2,54	-1,15	1,66	-1,15	-1,99
AH.2-1, %	0,31	0,20	0,31	0,41	-1,02	-1,02	0,59	-1,02	-1,31	

The volume-averaged spatial inhomogeneity ($\Delta X/\langle X \rangle$) and anisotropy ($An_{i,j}$) of elastic and related mechanical properties of "bulk" specimens of the investigated alloys before and after UIT are shown in the Figures 26 and 27.

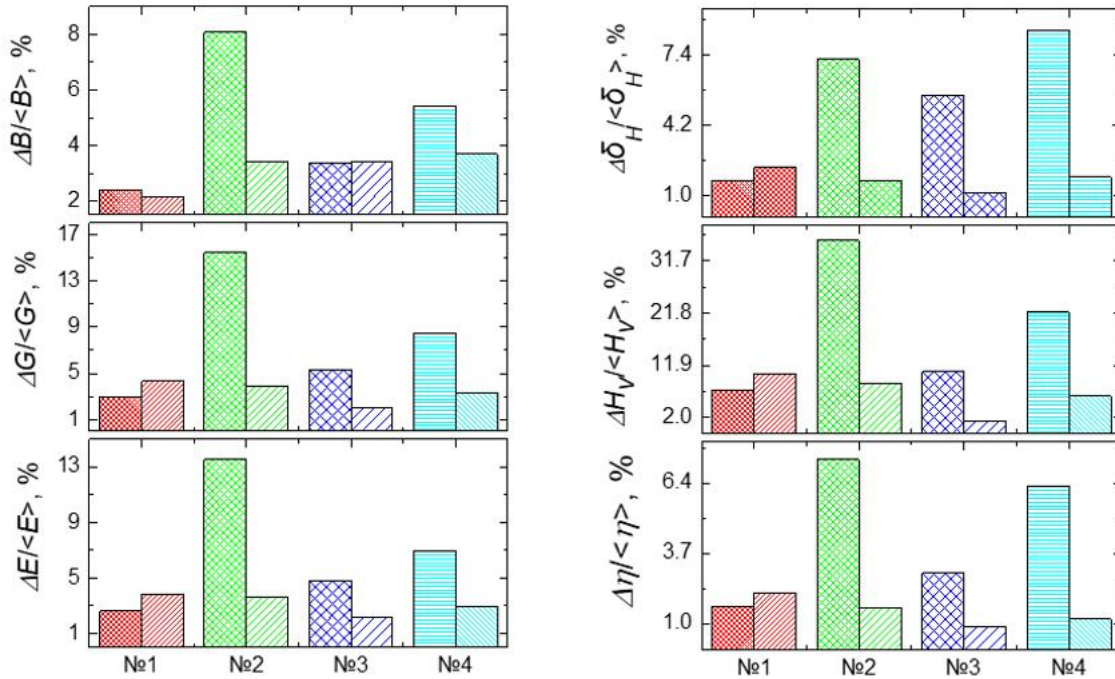


Figure 26. Spatial heterogeneity E , G , B , η , Vickers hardness HV , and plasticity characteristics (δH) for massive samples of TiZrNb alloys (№ 1, 3) and TiZrNbTa alloys (№ 2, 4) in the initial state and after UIT (left/right columns, respectively). UIT predominantly reduces heterogeneity within the volume of the samples.

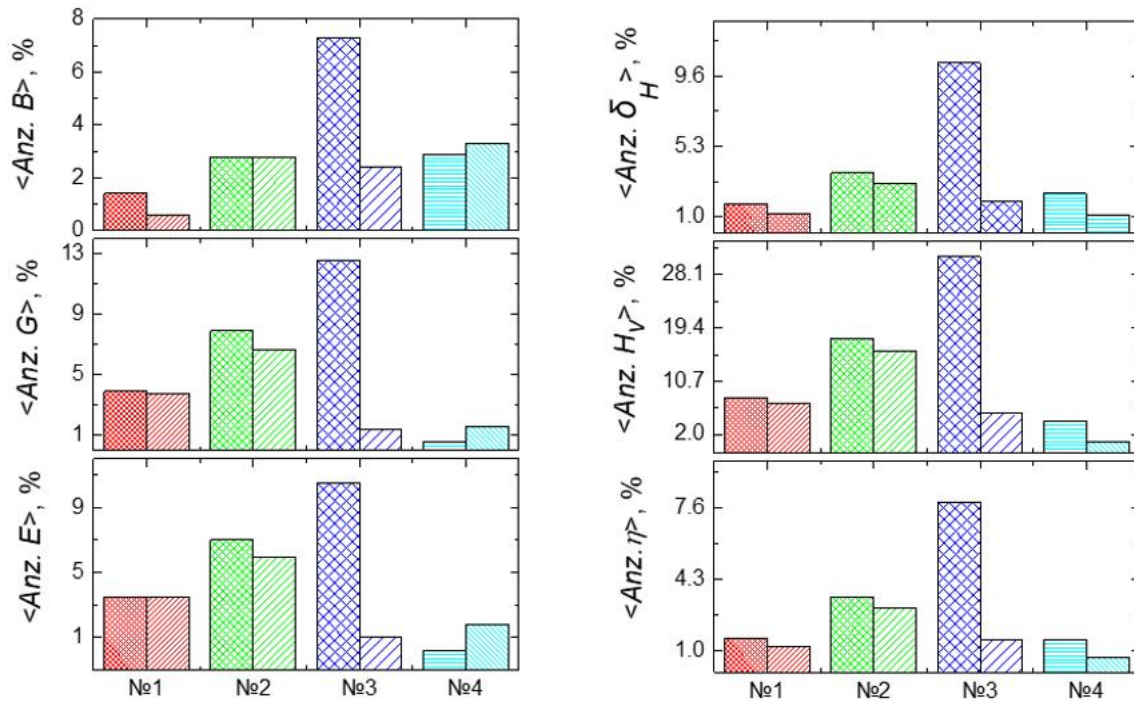


Figure 27. Anisotropy E , G , B , η , Vickers hardness HV , and plasticity characteristics (δ_H) for massive samples of TiZrNb and TiZrNbTa alloys in the initial state and after UIT (left/right columns, respectively). UIT predominantly reduces anisotropy within the volume of the samples by relaxing the fixators of texture elements.

In contrast to massive specimens, UIT of plates (Fig. 28) made of quaternary alloys with Ta additives (samples 2TZNT and 4ZTNT) strengthens the alloys (increasing E , G , and HV) due to the reduction in size in the deformation direction. The strengthening of Ta-containing alloys with decreasing thickness may be attributed to the onset of β -phase instability.

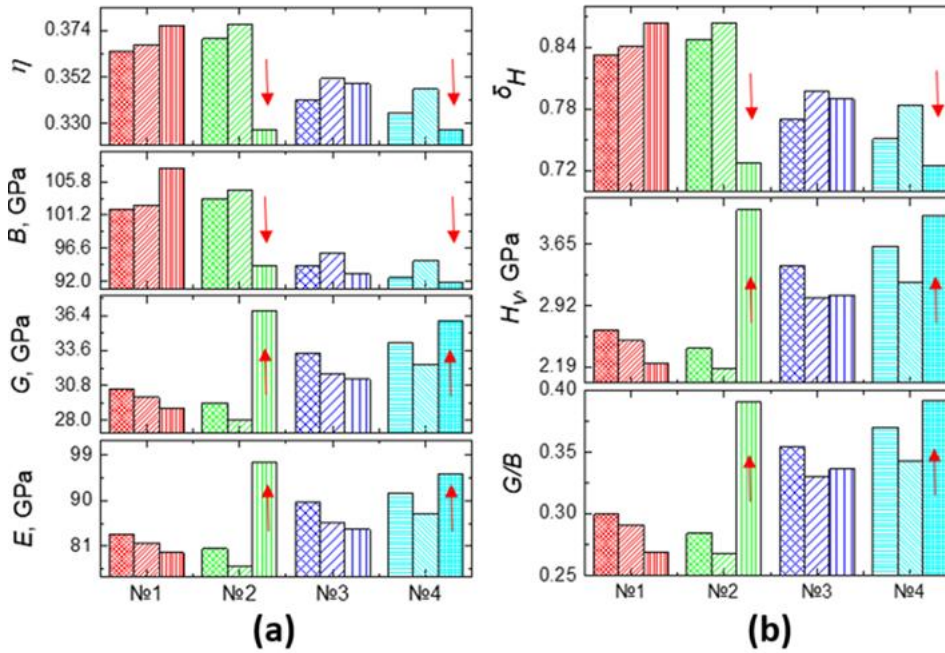


Figure 28. The elastic properties E , G , B , and η (a) and G/B , H_v and δ_H (b) of the TiZrNb and TiZrNbTa alloys in the initial state (the leftmost column), in the form of massive specimens after UIT (the middle column), and in the form of plates (the rightmost column).

Fig. 29 illustrates the relationship between η and G/B coefficient according to the work scheme [96], based on the results of our own US investigations of anisotropic and spatially inhomogeneous materials after averaging. The green markers represent data for TiZrNb and TiZrNbTa alloy specimens. It can be observed that the EP obtained in this study fit well on the $\eta(G/B)$ relationship, indicating that the averaging process is qualitative. This suggests that the applied method allows obtaining quantitative data on isotropic EP of anisotropic and elastic heterogeneous materials, which can be used for comparison with theoretical calculations. Comparison of the obtained results with literature data shows that isotropic values of moduli ($E = 77.1-95.34$ GPa; $G = 27.99-35.92$ GPa; $B = 91.81-104.63$ GPa), Poisson's ratio $\eta = 0.327-0.377$, and $HV = 2.504-3.996$ GPa are typical for multicomponent Ti-Zr-based alloys, so that they have potential applications in the medical field with further improvement, particularly by influencing the elastic anisotropy of directed deformations [139].

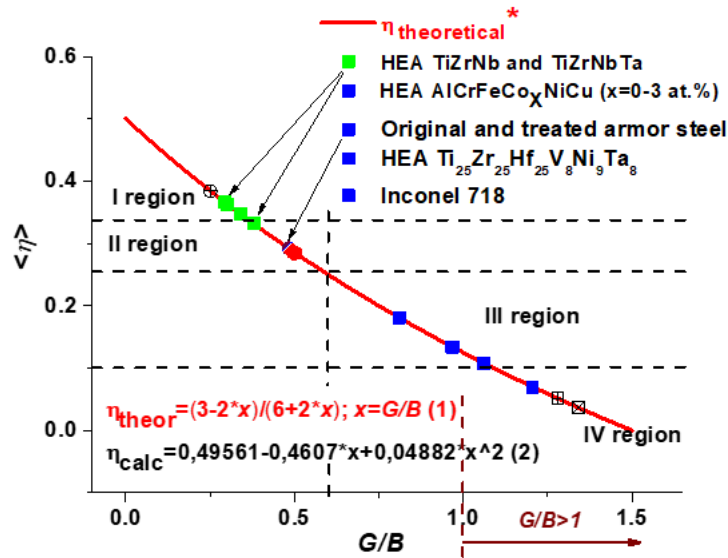


Figure 29. Dependence of the Poisson's ratio (η) on the G/B ratio according to the scheme proposed in [20] based on the results of our own ultrasonic (US) investigations of anisotropic and spatially heterogeneous materials after averaging. Green markers indicate data for samples made of TiZrNb and TiZrNbTa alloys.

A list of conclusions that can be drawn for this part is as following:

- 1) Increasing in Zr concentration by replacing Ti with Zr leads to an increase in Debye temperature T_D , E -, G -, B -moduli the G/B ratio, HV , and the δ_H parameter. These observations indicate strengthening of the alloy by increasing atomic incompatibility δ . These observations indicate alloy strengthening due to an increase in atomic size mismatch δ . The effect of Ta on the mentioned characteristics depends on the concentrations of Ti and Zr.
- 2) The UIT predominantly reduces the non-uniformity and anisotropy of all investigated alloys due to the effect of its alternating component. The change in specimens' thickness leads to the opposite results, which may be an indication of the onset of β -phase instability.
- 3) Reference data were obtained on the elastic parameters of inhomogeneous and anisotropic Ti- and Zr-based polycrystals, which are essential for comparison with corresponding theoretical calculations. A comparison of the obtained results with available literature data revealed that the studied multicomponent Ti-Zr-based alloys possess potential for biomedical applications, provided that

further optimization is undertaken—particularly through the control of elastic anisotropy and inhomogeneity under conditions of directional deformation.

3.3 The influence of ultrasonic impact treatment on the elastic and mechanical properties, and on susceptibility to hydrogen embrittlement of Inconel 718 alloy thin wires

In the Fig. 30 the results of mechanical tensile tests of Inconel 718 alloy after various thermo-mechanical treatments and hydrogenation are shown.

The UIT causes an increase in all studied characteristics, including ε , which indicates an increase in both strength and ductility of the alloy. Hydrogenation, as expected, reduces all characteristics, the subsequent UIT slightly restores $\sigma_{0,2}$, but further reduces σ_S and ε . At the same time, hydrogenation after UIT maintains the characteristics at a level higher than after WQ + annealing, and σ_S is higher even than that obtained after UIT. Therefore, the applied combination of hydrogenation + UIT is advantageous for this alloy. However, it should be noted that this result cannot be generalized without deeper investigations.

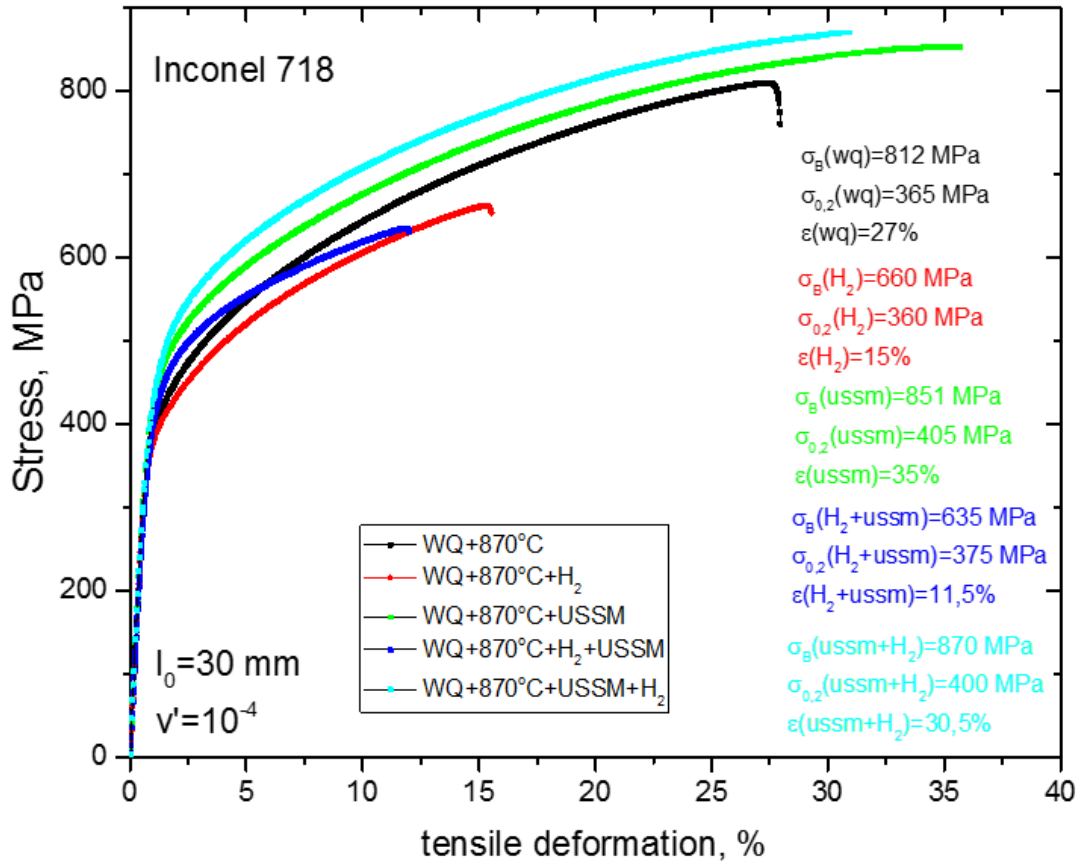


Figure 30. The stress-strain curves of Inconel 718 alloy wires after WQ, subsequent annealing at 870°C and further hydrogenation and UIT in different sequences

In the Fig. 31 the PF (111), relative changes in E - and G -moduli, and in the Fig. 32 the changes in E -, G -moduli, and HV hardness for the axial direction of the wire obtained by USTA results are shown. A decrease in (111) texture sharpness in the axial direction is observed after UIT, and an even greater decrease after subsequent hydrogenation. The anisotropy of Young's and shear moduli, as well as Young's modulus in the direction of the wire axis, decrease, while the shear modulus increases. This leads to an increase in the hardness of the material, which always depends on the complex of elastic characteristics.

It should be noted that Inconel 718 belongs to materials with a positive anisotropy factor, therefore the dependence of E - and G -moduli on crystallographic directions has the form shown in Fig. 33. The $\langle 111 \rangle$ directions correspond to the maximum value of Young's modulus (and the minimum value of G -modulus, respectively), and the $\langle 100 \rangle$ directions - vice versa. The $\langle 110 \rangle$ directions correspond

to intermediate values of the moduli. Therefore, a decrease in the (111) intensity correlate well with a decrease in the E value in this direction.

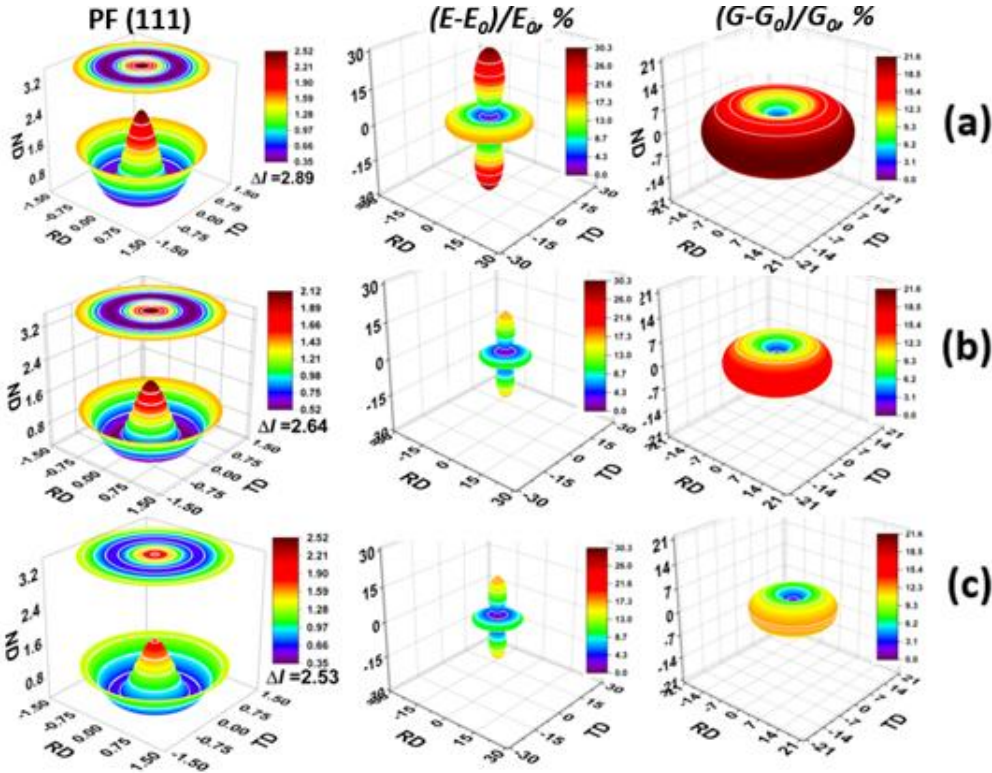


Figure 31. The PF (111), relative changes in E - and G -moduli of Inconel 718 alloy wires after WQ (a), WQ + UIT (b), and WQ + UIT + hydrogenation (c)

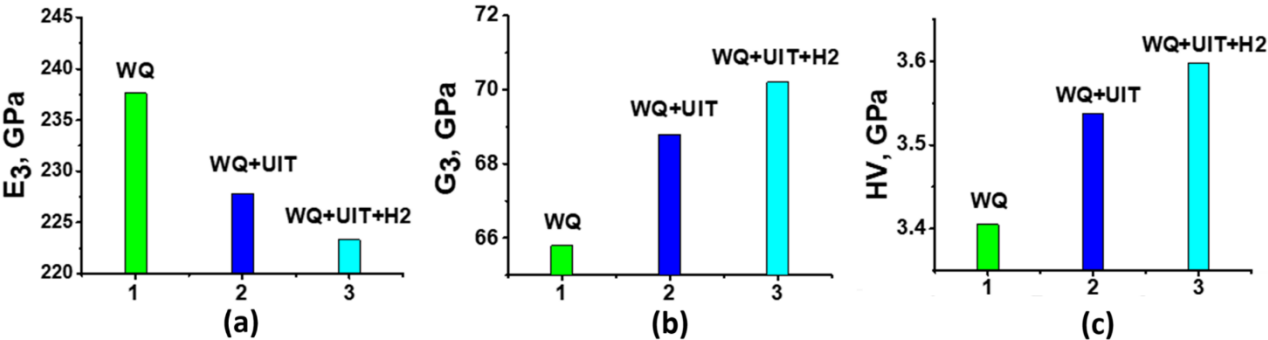


Figure 32. the changes in in E - (a), G -moduli (b), and HV hardness (c) after WQ, WQ + UIT, and WQ + UIT + hydrogenation

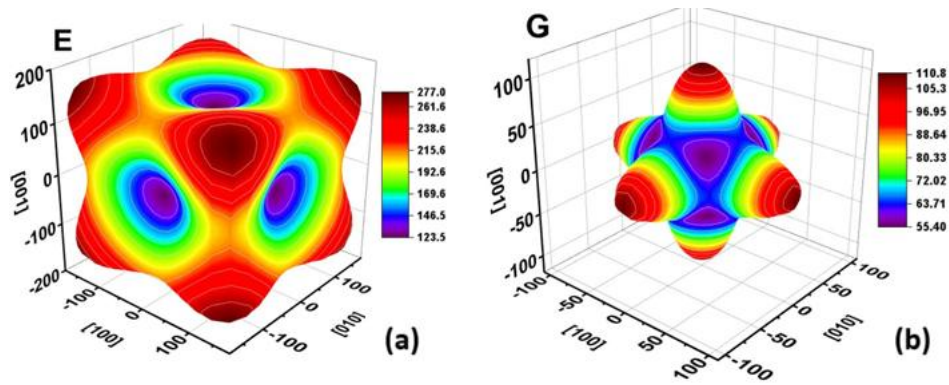


Figure 33. Surfaces of the Young modulus E (a) and shear modulus G (b) for the Inconel 718 single crystal in the initial state reconstructed based on the literature data regarding the elastic constants [132]: $C_{11} = 243.9$ GPa; $C_{12} = 154.9$ GPa; $C_{44} = 110.8$ GPa. The magnitudes of E and G in each direction is illustrated not only by color-coding according to each color scale but also by the distance from the center of the three-dimensional space.

In the Fig. 34 the EBSD structure images of the specimens after WQ, WQ + UIT, and WQ + UIT + hydrogenation (Fig. 34, a-d) are presented, and in the Fig.34 the fraction of [100] crystallites for the central, edge and all areas of the cross-section of the investigated specimens (Fig. 35, a), and the fraction of crystallites of all main crystallographic orientations ([100], [110], and [111]) for the whole cross-section area (Fig. 35, b) are shown.

The results indicate a decrease in the intensity of [111] in the axial direction of the wire after UIT + hydrogenation, which correlate with those obtained using USTA and confirm the possibility of determining the properties of the material with its help in directions inaccessible for measurements, provided that the samples are axially textured. Additionally, an increase in the intensity of [100] is observed, which along with decreasing of E -value (indicated by decreasing of [111] intensity) means an increase in G -modulus in the axial direction (according to Fig. 33). This result also confirms the USTA data and leads to the conclusion, that the textural factor plays a key role in the decrease in Young's modulus, the increase in the shear modulus and, subsequently, the hardness of the alloy. The possibility of determining these characteristics by the express USTA method is extremely promising for technical and

production purposes, considering that methods that can directly determine textural and elastic characteristics from the cross-sectional plane of the wire are quite cumbersome and expensive, require careful preparation of samples, and do not allow for control under operating conditions.

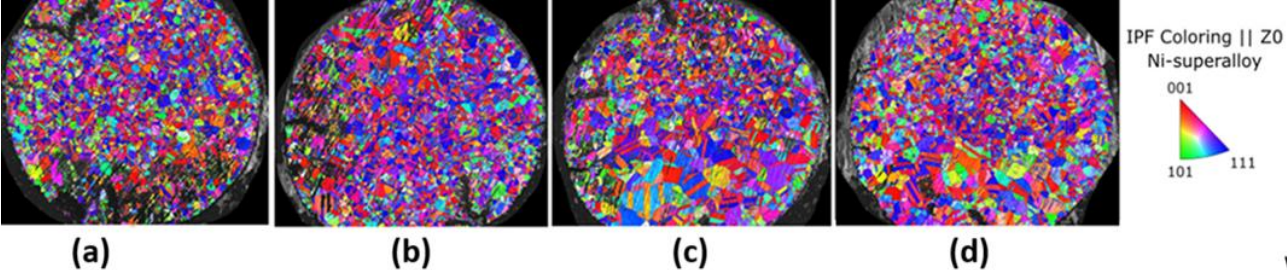


Figure 34. The EBSD structure images of the cross-section of Inconel 718 wires specimens after WQ (a), WQ + UIT (b), WQ + H₂ (c), and WQ + H₂ + UIT (d) accompanied by IPF Coloring

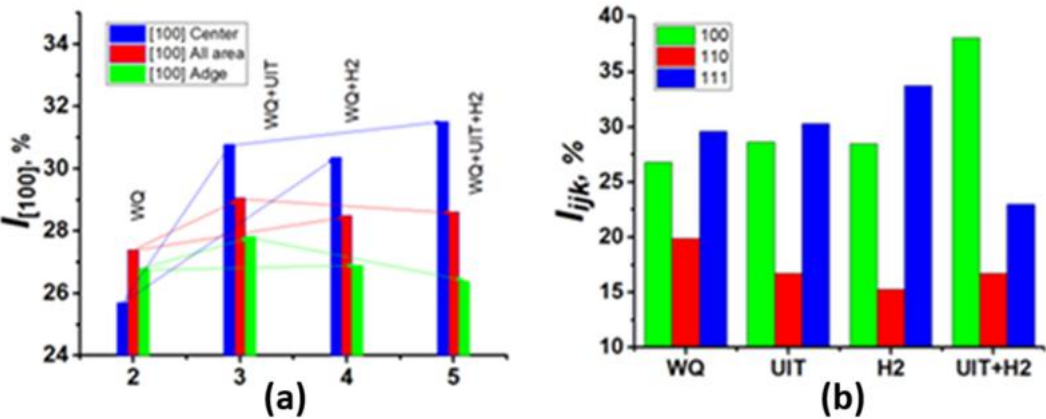


Figure 35. The fraction of [100] crystallites for the central, edge and all areas of the cross-section of Inconel 718 wire specimens (a), and the fraction of crystallites of all main crystallographic orientations ([100], [110], and [111]) for the whole cross-section area (b)

A list of conclusions that can be drawn for this part is as following:

- 1) The increase in the proportion of [100] crystallites in the axial direction after all types of treatments gives grounds to assert that the decrease in Young's modulus E, the increase in the shear modulus G, and the increase in Hv of the alloy are due to the textural factor.

- 2) The effectiveness of the used USTA method for studying wire samples from Inconel 718 type alloys was confirmed, as well as the prospects for using UIT to prevent hydrogen embrittlement of their surface.

THE MAIN RESULTS AND CONCLUSIONS

1. An abnormal brass-to-copper texture transition in Cu-37Zn massive specimens was observed for the first time using ultrasonic impact treatment (UIT) at the ambient temperature (air-UIT). This effect is explained by the influence of the alternating component of the UIT, which facilitates the movement of fixed dislocation segments by breaking their fixation points. The absence of texture-type changes after UIT at cryogenic temperature (cryo-UIT) is attributed to the suppression of defect movement and the promotion of twinning, which results in a brass-type texture. Corresponding changes in the elastic state, hardness, and ductility of the alloys were also observed. This result demonstrates the possibility of obtaining the desired texture and elastic state of the material by selecting the appropriate combination of the aforementioned high-rate deformation methods. In contrast, for plates of the same alloy, air-UIT led to the formation of a copper-type texture, while cryo-UIT produced the expected brass-type texture. This difference in the effect of UIT on massive and plate specimens is explained by the change in maximum stresses developed by the static and alternating components of UIT as the specimens' thickness changes.
2. Reference data were obtained on the elastic and mechanical properties of the alloys 51Ti31Zr10Nb8Ta, 31Ti51Zr10Nb8Ta, 51Ti31Zr18Nb, and 31Ti51Zr18Nb, as well as on the individual effects of Ti, Zr, Nb, and Ta on these properties.
3. An increase in the Young's modulus (E), shear modulus (G), and Vickers hardness (HV) was observed in thin plates of Ta-containing alloys, which may indicate the onset of β -phase instability after UIT.
4. The potential of high-energy dynamic treatments, such as ultrasonic impact treatment (UIT), has been demonstrated for reducing the anisotropy and heterogeneity of the elastic parameters of Ti-Zr-based biomedical β -alloys.
5. For the first time, the ultrasonic texture analysis method was applied to the experimental investigation of the elastic, textural, and the main mechanical properties of small-diameter ($d = 1$ mm) Inconel 718 superalloy wire subjected

to combined hydrogen charging and ultrasonic impact treatment. The crucial role of texture in mechanical properties changes after hydrogenation and/or ultrasonic impact treatment was also established, along with the potential of UIT for preventing hydrogen embrittlement of the surface of the investigated material.

LIST OF REFERENCES

1. Franceschini E.A. Nanostructured Multifunctional Materials: Synthesis, Characterization, Applications and Computational Simulation, 1st ed., Boca Raton, CRC Press, 2021. <https://doi.org/10.1201/9780367822194>
2. Gomez-Villalba L.S. Advances in Nanostructured Materials for Multifunctional Applications: Synthesis, Characterization and Properties, Trans Tech. Publ., 2019. <https://doi.org/10.4028/b-L81ZTg>
3. Zaporozhets O.I., Mordyuk B.N., Mykhailovskyi V.A., Halkina A.A., Dordienko M.O., Burmak A.P., Langi E., Zhao L.G. 2024. Tailoring elastic, mechanical and texture properties of Cu-37Zn brass by ultrasonic impact treatment applied at ambient and cryogenic temperatures, Mater. Today Communications 38, 108325. <https://doi.org/10.1016/j.mtcomm.2024.108325>
4. Zaporozhets O.I., Mordyuk B.N., Dordienko N.A., Mykhailovskyi V.A., Halkina A.A. 2020. Influence of surface ultrasonic impact treatment on texture evolution and elastic properties in the volume of Zr1Nb alloy, Surf. Coat. Technol. 403, 126397. <https://doi.org/10.1016/j.surfcoat.2020.126397>
5. Kallend J. S., Davies G. J. The copper and copper-zinc alloys, texture, 1972, 1, pp.51-69, doi: 10.1155/TSM.1.51
6. Wenk H-R., Van Houtte P. Texture and anisotropy, Rep. Prog. Phys. 67 (2004) 1367–1428, doi:10.1088/0034-4885/67/8/R02
7. Hu H., Sperry P. R., Beck P. A. Rolling Textures in Face-Centered Cubic Metals, Journal of metals, 1952, pp.76-81
8. Hu H., Cline R. S. Temperature Dependence of Rolling Textures in High-Purity Silver, Journal of applied physics, Vol. 32, № 5, 1961, pp. 760-763.
9. Smallman R. E., Creen D. The dependence of rolling texture on stacking fault energy, Acta metallurgica, vol. 12, 1964, pp. 145-154.
10. Madhavan R., Kalsar R., Ray R. K., Suwas S. Role of stacking fault energy on texture evolution revisited, Materials Science and Engineering 82 (2015) 012031 doi:10.1088/1757-899X/82/1/012031

- 11.El-Danaf E., Kalidindi S. R., Doherty R. D., Necker C. Deformation texture transition in brass: critical role of micro-scale shear bands, *Acta mater.* 48 (2000) 2665-2673, doi: [https://doi.org/10.1016/S1359-6454\(00\)00050-1](https://doi.org/10.1016/S1359-6454(00)00050-1)
- 12.Lapeire L., Sidor J., Verleysen P., Verbeken K., De Graeve I., Terryn H., Kestens L.A.I. Texture comparison between room temperature rolled and cryogenically rolled pure copper, *Acta Materialia* 95 (2015) 224–235
- 13.Wassermann G. Der einfluß mechanischer zwillingsbildung auf die entstehung der walztexturen kubisch hlächenzentrierter metalle. *International Journal of Materials Research*, 54(2), 1963, 61-65.
- 14.Hu H. On the mechanism of texture transition in face centered cubic metals, textures and microstructures, 1988, Vols. 8 & 9, pp. 191-206
- 15.Leffers T. Deformation rate dependence of rolling texture in brass containing 5% zinc, *Scripta metallurgica* Vol. 2, pp. 447-452, 1968
- 16.Dillamore I. L., Roberts W. T., Rolling textures in f.c.c. and b.c.c. metals, *act.4 metallurgica*, Vol. 12, 1961, pp. 281-293
- 17.Sitdikov V.D., Zaynullina L.I., Wei K.X., Wei W., Alexandrov I.V. Unusual texture transition during the rolling of the UFG Cu-10%Zn alloy, *Materials Characterization* 149 (2019) 153–157, <https://doi.org/10.1016/j.matchar.2019.01.027>
- 18.Zaporozhets O.I., Mordyuk B.N., Mykhailovskyi V.A., Halkina A.A., Mazanko V.F., Vorona S.P., Ultrasonic nondestructive evaluation of texture and elastic properties of Cu-37Zn brass subjected to shock compression and ultrasonic impact treatment, *Materials Characterization* 226 (2025) 115223. <https://doi.org/10.1016/j.matchar.2025.115223>
- 19.Zaporozhets O.I., Mordyuk B.N., Dordienko N.A., Mykhailovsky V.A., Mazanko V.F., Karasevskaya O.P. Ultrasonic studies of texture inhomogeneities in pressure vessel steel subjected to ultrasonic impact treatment and shock compression, *Surface & Coatings Technology* (2016), doi: 10.1016/j.surfcoat.2016.09.05

20. Statnikov E.S. Physics and mechanism of ultrasonic impact, IIW Document XIII-2004-04.
21. Jamaati R. Four unusual texture transitions in high purity copper during cold deformation followed by quenching, *Mater. Res. Express* 6 (2019) 016513, doi:10.1088/2053-1591/aae4ec
22. Li W., Xie D., Li D., Zhang Y., Gao Y., Peter K. L. Mechanical behavior of high-entropy alloy, *Progress in Materials Science* 118 (2021) 100777, doi: 10.1016/j.pmatsci.2021.100777
23. Miracle D.B., Senkov O.N. A critical review of high entropy alloys and related concepts. *Acta Mater* 2017;122:448–511, doi: 10.1016/j.actamat.2016.08.081
24. Zhang Y., Zuo T.T., Tang Z., Gao M.C., Dahmen K.A., Liaw P.K., et al. Microstructures and properties of high-entropy alloys. *Prog Mater Sci* 2014;61:1–93, doi: 10.1016/j.pmatsci.2013.10.001
25. George E.P., Raabe D., Ritchie R.O. High-entropy alloys. *Nat Rev Mater* 2019;4:515–34, doi: 10.1038/s41578-019-0121-4
26. George E.P., Curtin W.A., Tasan C.C. High entropy alloys: A focused review of mechanical properties and deformation mechanisms. *Acta Mater* 2020;188:435–74, doi: 10.1016/j.actamat.2019.12.015
27. Sathiyamoorthi P., Kim H.S. High-entropy alloys with heterogeneous microstructure: Processing and mechanical properties. *Prog Mater Sci* 2020:100709, doi: 10.1016/j.pmatsci.2020.100709
28. Li Z., Zhao S., Ritchie R.O., Meyers M.A. Mechanical properties of high-entropy alloys with emphasis on face-centered cubic alloys. *Prog Mater Sci* 2019;102: 296–345, doi: 10.1016/j.pmatsci.2018.12.003
29. Ozan S., Lin J., Li Yu., Wen C. New Ti-Ta-Zr-Nb alloys with ultrahigh strength and elastic strain for potential orthopedic implant applications, *Journal of the Mechanical Behavior of Biomedical Materials*, <http://dx.doi.org/10.1016/j.jmbbm.2017.07.011>

30. de Oliveira T.G., Fagundes D.V., Capellato P., Sachs D., da Silva A.A.A.P. A review of biomaterials based on high-entropy alloys. *Metals* 2022;12(11):1940, doi: 10.3390/met12111940
31. Feng J., Tang Y., Liu J., Zhang P., Liu C., Wang L.Q. Bio-high entropy alloys: progress, challenges, and opportunities. *Front Bioeng Biotechnol* 2022;10:1510, doi: 10.3389/fbioe.2022.977282
32. Hu S., Li X., Lin Y., Li T., Zhang G., Li J., Zhang X., Liu D., Systematic study of $(\text{TiZr})_x\text{Nb}_y(\text{TaMo})_z$ medium entropy alloys for biomedical implants, *Journal of Materials Research and Technology* 2023;24:7683 e7703, doi: 10.1016/j.jmrt.2023.05.036
33. Niinomi M. Mechanical properties of biomedical titanium alloys. *Mater Sci Eng, A* 1998;243:231e6, doi : 10.1016/S0921-5093(97)00806-X
34. Wu K.L., Xu Y.J., Zhang L., Zhang Y., Xu W., Chu J.B., et al. Which implant is better for beginners to learn to treat geriatric intertrochanteric femur fractures: a randomised controlled trial of surgeons, metalwork, and patients. *J. Orthop. Transl.* 2020;21:18e23, doi: 10.1016/j.jot.2019.11.003
35. Biant L.C., Bruce W.J.M., Van der Wall H., Walsh W.R. Infection or Allergy in the Painful Metal-on-Metal Total Hip Arthroplasty?, *The Journal of Arthroplasty*, 2010, 25, 334.e311- 334.e316, doi: 10.1016/j.arth.2008.08.015
36. Granchi D., Cenni E., Tigani D., Trisolino G., Baldini N., Giunti A. Sensitivity to implant materials in patients with total knee arthroplasties. *Biomaterials*, 2008, 29, 1494-1500, doi: 10.1016/j.biomaterials.2007.11.038
37. Zhubrak M., Bar-David T. Systemic Nickel Allergy after Internal Fixation of a Bunionectomy. *The Journal of Foot and Ankle Surgery*, 2014, 53, 466-467, doi: 10.1053/j.jfas.2014.03.006
38. Okazaki Y., Gotoh E. Comparison of metal release from various metallic biomaterials in vitro. *Biomaterials*, 2005, 26, 11-21, DOI: 10.1016/j.biomaterials.2004.02.005

39. Zhang L.C., Chen L.Y. A review on biomedical titanium alloys: recent progress and prospect. *Adv Eng Mater*, 2019, 21(4):1801215, doi: 10.1002/adem.201801215
40. Jawed S.F., Rabadia C.D., Khan M.A., Khan S.J. Effect of Alloying Elements on the Compressive mechanical properties of biomedical titanium alloys: a systematic review. *ACS Omega* 2022;7(34):29526e42, doi: 10.1021/acsomega.2c02096
41. Nguyen V.T., Qian M., Shi Z., Song T., Huang L., Zou J. Compositional design of strong and ductile (tensile) Ti-Zr-Nb-Ta medium entropy alloys (MEAs) using the atomic mismatch approach, *Materials Science & Engineering A*, <https://doi.org/10.1016/j.msea.2018.11.054>
42. Polmear I. J. *Light alloys*, 1995, 3rd ed. Edward Arnold, London, UK.
43. Yeh J.-W. Alloy design strategies and future trends in high-entropy alloys, *JOM (J. Occup. Med.)* 65 (12) (2013) 1759–1771, doi: 10.1007/S11837-013-0761-6
44. Senkov O.N., Scott J.M., Senkova S.V., Miracle D.B., Woodward C.F. Microstructure and room temperature properties of a high-entropy TaNbHfZrTi alloy. *J Alloys Compd* 2011;509:6043-8, doi: 10.1016/j.jallcom.2011.02.171
45. Guo N.N., Wang L., Luo L.S., Li X.Z., Su Y.Q., Guo J.J., et al. Microstructure and mechanical properties of refractory MoNbHfZrTi high-entropy alloy. *Mater Des* 2015;81:87e94, doi: 10.1016/j.matdes.2015.05.019
46. Juan C.C., Tsai M.H., Tsai C.W., Lin C.M., Wang W.R., Yang C.C., et al. Enhanced mechanical properties of HfMoTaTiZr and HfMoNbTaTiZr refractory high-entropy alloys. *Intermetallics* 2015;62:76e83, doi: 10.1016/j.intermet.2015.03.013
47. Hu S.W., Li T.J., Su Z.Q., Liu D.X. Research on suitable strength, elastic modulus and abrasion resistance of TiZrNb medium entropy alloys (MEAs) for implant adaptation. *Intermetallics* 2022;140:107401, doi: 10.1016/j.intermet.2021.107401

48. Yuan Y., Wu Y., Yang Z., Liang X., Lei Z.F., Huang H.L., et al. Formation, structure and properties of biocompatible TiZrHfNbTa high-entropy alloys. *Mater. Res. Lett.* 2019;7:225e31, doi: 10.1080/21663831.2019.1584592
49. Nguyen V.T., Qian M., Shi Z., Song T., Huang L., Zou J. A novel quaternary equiatomic Ti-Zr-Nb-Ta medium entropy alloy (MEA). *Intermetallics* 2018, 101:39-43, doi: 10.1016/j.intermet.2018.07.008
50. Wu Y.D., Cai Y.H., Wang Y.D., Wang T., Si J.J., Zhu J., et al. A refractory Hf₂₅Nb₂₅Ti₂₅Zr₂₅ high-entropy alloy with excellent structural stability and tensile properties. *Mater Lett* 2014;130:277-80, doi: 10.1016/j.matlet.2014.05.134
51. Tane M., Akita S., Nakano T., Hagihara K., Umakoshi Y., Niinomi M., Nakajima H. Peculiar elastic behavior of Ti–Nb–Ta–Zr single crystals, *Acta Materialia* 56 (2008) 2856–2863, DOI: 10.1016/j.actamat.2008.02.01
52. Tane M., Akita S., Nakano T., Hagihara K., Umakoshi Y., Niinomi M., Mori H., Nakajima H. Low Young's modulus of Ti–Nb–Ta–Zr alloys caused by softening in shear moduli c_{00} and c_{44} near lower limit of body-centered cubic phase stability, *Acta Materialia* 58 (2010) 6790–6798, DOI: 10.1016/j.actamat.2010.09.007
53. Lee T., Lee S., Kim I., Moon Y. H., Kim H. S., Park C. H., Breaking the limit of Young's modulus in low-cost Ti-Nb-Zr alloy for biomedical implant applications, *Journal of Alloys and Compounds* 828 (2020) 154401, doi: 10.1016/j.jallcom.2020.154401
54. Schönecker S., Li X., Wei D., Nozaki Sh., Kato H., Vitos L., Li X., Harnessing elastic anisotropy to achieve low-modulus refractory high-entropy alloys for biomedical applications, *Materials & Design*, 215, 2022, 110430, doi: 10.1016/j.matdes.2022.110430
55. Schuh B., Völker B., Todt J., Schell N., Perrière L., Li J., Couzinié J.P., Hohenwarter A., Thermodynamic instability of a nanocrystalline, single-phase TiZrNbHfTa alloy and its impact on the mechanical properties, *Acta Mater.* 142 (2018) 201-212, doi: 10.1016/j.actamat.2017.09.035

- 56.Podolskiy A.V., Tabachnikova E.D., Voloschuk V.V., Gorban V.F., Krapivka N.A., Firstov S.A., Mechanical properties and thermally activated plasticity of the Ti₃₀Zr₂₅Hf₁₅Nb₂₀Ta₁₀ high entropy alloy at temperatures 4.2–350K, *Mater. Sci. Eng. A* 710 (2018) 136-141
- 57.Senkov O.N., Miracle D.B., Chaput K.J., Couzinie J.P., Development and exploration of refractory high entropy alloys—A review, *J. Mater. Res.* (2018) 1-37
- 58.Senkov O.N., Pilchak A.L., Semiatin S.L., Effect of Cold Deformation and Annealing on the Microstructure and Tensile Properties of a HfNbTaTiZr Refractory High Entropy Alloy, *Metall. Mater. Trans. A* 49(7) (2018) 2876-2892.
- 59.Couzinie J.-P., Dirras G., Body-centered cubic high-entropy alloys: From processing to underlying deformation mechanisms, *Materials Characterization*, Volume 147, January 2019, Pages 533-544, doi: 10.1016/j.matchar.2018.07.015
- 60.Dirras G., Couque H., Lilensten L., Heczal A., Tingaud D., Couzinie J.-P., Perriere L., Gubicza J., Guillot I., Mechanical behavior and microstructure of Ti₂₀Hf₂₀Zr₂₀Ta₂₀Nb₂₀ high-entropy alloy loaded under quasi-static and dynamic compression conditions, *Mater. Charact.* 111 (2016) 106–113, <https://doi.org/10.1016/j.matchar.2015.11.018>.
- 61.Delannoy S., Baiz S., Laheurte P., Jordan L., Prima F. Elastically Graded Titanium Alloy Produced by Mechanical Surface Deformation // *Front. Mater.*, 16 March 2021 *Sec. Biomaterials*, Vol. 8, 2021, doi: 10.3389/fmats.2021.634236
- 62.Zaporozhets O.I., Mordyuk B.N., Dordienko N.A., Mykhailovskyi V.A., Halkina A.A., Influence of surface ultrasonic impact treatment on texture evolution and elastic properties in the volume of Zr₁Nb alloy, *Surface and Coatings Technology* 403, 126397 <https://doi.org/10.1016/j.surfcoat.2020.126397>
- 63.Zaporozhets O.I., Mordyuk B.N., Dordienko N.A., Mykhailovsky V.A., Mazanko V.F., Karasevskaya O.P.. Ultrasonic studies of texture inhomogeneities in pressure vessel steel subjected to ultrasonic impact treatment and shock compression, *Surface and Coatings Technology*, 307A, 2016, p.693-701. <https://doi.org/10.1016/j.surfcoat.2016.09.053>

64. Chenakin S.P., Mordyuk B.N., Khripta N.I., Surface characterization of a ZrTiNb alloy: Effect of ultrasonic impact treatment, *Applied Surface Science* 470 (2019) 44-55, DOI: 10.1016/j.apsusc.2018.11.116
65. Popov A. A., Illarionov A. G., Grib S. V., Elkina O. A., Ivasishin O. M., Markovskii P. E., Skiba I. A., Effect of Heat Treatment and Plastic Deformation on the Structure and Elastic Modulus of a Biocompatible Alloy Based on Zirconium and Titanium, 2012, published in *Fizika Metallov i Metallovedenie*, 2012, Vol. 113, No. 4, pp. 404–412, DOI: 10.1134/S0031918X12040102
66. Johnson W.H. On some remarkable changes produced in iron and steel by the action of hydrogen and acids. *Proc Roy Soc Lond* 1874;23:168, doi:10.1098/rspl.1874.0024.
67. Bhadeshia H. K. D. H. Prevention of Hydrogen Embrittlement in Steels, *ISI International* 56 (2016), 24-36
68. Chen Yi-Sh., Huang C., Liu P.-Yu., Yen H.-W., Niu R., Burr P., Moore K. L., Martínez-Paneda E., Atrensi A., Cairney J. M. Hydrogen trapping and embrittlement in metals – A review, *International Journal of Hydrogen Energy*, Volume 136, 2025, 789-821, DOI: 10.1016/j.ijhydene.2024.04.076
69. Park Ch., Kang N., Liu S. Effect of grain size on the resistance to hydrogen embrittlement of API 2W Grade 60 steels using in situ slow-strain-rate testing, *Corrosion Science* (2017), 128, 2017, 33-41
70. Koyama M., Akiyama E., Lee Y.K., Raabe D., Tsuzaki K. Overview of hydrogen embrittlement in high-Mn steels. *Int J Hydrogen Energy* 2017;42:12706, doi: 10.1016/j.ijhydene.2017.02.214.
71. Abdollahi M., Sameezadeh M., Vaseghi M. Experimental and statistical optimization of the hydrogen reduction process of nickel oxide. *Mater Manuf Process* 2018;33: 856. doi: 10.1080/10426914.2017.1364751.
72. Hillier E.M.K., Robinson M.J. Hydrogen embrittlement of high strength steel electroplated with zinc–cobalt alloys. *Corros Sci* 2004;46:715–27. [https://doi.org/ 10.1016/S0010-938X\(03\)00180-X](https://doi.org/10.1016/S0010-938X(03)00180-X).

73. Figueroa D., Robinson M.J. The effects of sacrificial coatings on hydrogen embrittlement and re-embrittlement of ultra high strength steels. *Corros Sci* 2008; 50:1066–79. doi: 10.1016/j.corsci.2007.11.023.
74. Fite S., Zukerman I., Shabat A.B., Barzilai S. Hydrogen protection using CrN coatings: experimental and theoretical study. *Surf Interfaces* 2023;37:102629. doi: 10.1016/j.surfin.2023.102629.
75. Gu D.D., Shi X., Poprawe R., Bourell D.L., Setchi R., Zhu J. Material-structure performance integrated laser-metal additive manufacturing. *Science* 2021;372: 6545. doi: 10.1126/science.abg1487.
76. Venkatesan K., Sivasankari R., Balusamy V., Saxena A., Jha P., Datta R. Hydrogen induced cracking in GMA welds of vanadium–titanium microalloyed high strength steel. *Mater Manuf Process* 2010;25:175. <https://doi.org/10.1080/10426910903206766>.
77. Gavriljuk V.G., Shyvaniuk V.M., Teus S.M. Hydrogen in metallic alloys – embrittlement and enhanced plasticity: a review, *Corrosion Reviews* 42 (2024) 2150026, DOI: 10.1515/corrrev-2022-0060.
78. Gavriljuk V.G., Shyvaniuk V.M., Teus S.M. *Hydrogen in Engineering Metallic Materials: From Atomic-Level Interactions to Mechanical Properties*, Springer International Publishing, Cham, 2022, DOI: 10.1007/978-3-030-98624-5.
79. Liu C., Ichitsubo T., Kato H. Effects of precipitation phases on the hydrogen embrittlement sensitivity of Inconel 718, *Corrosion Science* 205 (2022) 110438, DOI: 10.1016/j.corsci.2022.110438.
80. Wang Y., Xie H., Zhou Zh., Li X., Wu W., Gong J., Effect of shot peening coverage on hydrogen embrittlement of a ferrite-pearlite steel, *international journal of hydrogen energy*, *International Journal of Hydrogen Energy*, Vol. 45 (11), 2020, P. 7169-7184, ISSN 0360-3199, doi: 10.1016/j.ijhydene.2020.01.021.
81. Kumar G.R., Rajyalakshmi G., Swaroop S. A critical appraisal of laser peening and its impact on hydrogen embrittlement of titanium alloys, *Proc IMechE Part B: J Engineering Manufacture* 1–28, DOI: 10.1177/0954405419838956

82. Baek S.-H., He Sh., Jang M.-S., Back D.-H., Jeong D.-W., Park S.-H. Ultrasonic nanocrystal surface modification effect on reduction of hydrogen embrittlement in Inconel-625 parts fabricated via additive manufacturing process, *Journal of Manufacturing Processes* 108 (2023) 685–695, doi: 10.1016/j.jmapro.2023.11.024
83. Lu X., Depover T., Johnsen R. Evaluation of hydrogen diffusion and trapping in nickel Alloy 625 by thermal desorption spectroscopy, *international journal of hydrogen energy* 47 (2022) 31673–31683, DOI: 10.1016/j.ijhydene.2022.07.094
84. Chen S., Zhao M., Rong L. Effect of grain size on the hydrogen embrittlement sensitivity of a precipitation strengthened Fe–Ni based alloy, *Materials Science & Engineering A* 594 (2014) 98–102, DOI: 10.1016/j.msea.2013.11.062
85. Oudriss A., Creus J., Bouhattate J., Savall C., Peraudeau B., Feaugas X. The diffusion and trapping of hydrogen along the grain boundaries in polycrystalline nickel. *Scripta Mater* 2012;66. <https://doi.org/10.1016/j.scriptamat.2011.09.036>.
86. Khalid H., Shunmugasamy V. C., DeMott R. W., Hattar Kh., Mansoor B. Effect of grain size and precipitates on hydrogen embrittlement susceptibility of nickel alloy 718, *International Journal of Hydrogen Energy* 55 (2024) 474–490, DOI: 10.1016/j.ijhydene.2023.11.233
87. Tehranchi A., Curtin W.A. Atomistic study of hydrogen embrittlement of grain boundaries in nickel: I. Fracture, *Journal of the Mechanics and Physics of Solids* 101 (2017) 150–165, doi: 10.1016/j.jmps.2017.01.020
88. Lee J.-Ch., Yang D. Ch., Sung M. Y., Kim N.-S., Park H.-K., Choi M., Kim Y. D., Sohn S. S., Park Ch.-S., Influence of crystallographic textures on the hydrogen embrittlement resistance of austenitic stainless steel, *Journal of Materials Research and Technology* 32 (2024) 2757–2766, doi: 10.1016/j.jmrt.2024.08.078
89. Masoumi M., Silva C.C., Beres M., Ladino D.H., G. de Abreu H.F.G. Role of crystallographic texture on the improvement of hydrogen-induced crack resistance in API 5L X70 pipeline steel. *Int. J. Hydrog. Energy* 2017;42:1318–26. <https://doi.org/10.1016/j.ijhydene.2016.10.124>.

90. Masoumi M., Santos L.P.M., Bastos I.N., Tavares S.S.M., da Silva M.J.G., G. de Abreu H.F. Texture and grain boundary study in high strength Fe–18Ni–Co steel related to hydrogen embrittlement. *Mater Des* 2016;91:90–7. <https://doi.org/10.1016/j.matdes.2015.11.093>
91. Li J., Oudriss A., Metsue A., Bouhattate J., Feugas X. Anisotropy of hydrogen diffusion in nickel single crystals: the effects of self-stress and hydrogen concentration on diffusion. *Sci. Reports* 2017;7:45041–9. <https://doi.org/10.1038/srep45041>
92. Sayers C. M. Ultrasonic velocities in anisotropic polycrystalline aggregates, *J. Phys. D: Appl. Phys.*, 15 (1982) 2157–2167. Printed in Great Britain
93. Zaporozhets O. I., Kotrechko S. A., Dordienko N. A., Mykhailovsky V. A., Zatsarnaya A. V. (2015). Ultrasonic investigation of macro residual stresses in 15Cr2NMFA steel after uniaxial compression. *Problems of Atomic Science and Technology (VANT)*, 2(96), 197–203. ISSN 1562-6016.
94. M. Hirao, N. Hara. Ultrasonic Pole Figure for the Texture of Aluminium Alloy // *Appl. Phys. Lett.* 1987, v. 50, N 20, p. 1411–1412.
95. Hao R., Zhang X., Qin J., Ning J., Zhang S., Niu Z., Ma M., Liu R. Anisotropy in elasticity and thermodynamic properties of zirconium tetraboride under high pressure, *RSC Adv.* 5 (2015) 77399–77406, <https://doi.org/10.1039/C5RA15992J>
96. Wang X., Zhang Y.-T., Liu P.-Ch., Yan J., Mo W., Zhang P.-Ch., Chen X.-Q. Ductile-to-brittle transition and materials' resistance to amorphization by irradiation damage, *RSC Adv.*, 2016, 6, 44561–44568. <https://doi.org/10.1039/C6RA05194D>
97. Milman Yu.V., Chugunova S.I., Goncharova I.V., Golubenko A.A. Plasticity of materials determined by the indentation method, *Prog. Phys. Met.* 19 (3) (2018) 271–308, <https://doi.org/10.15407/ufm.19.03.271>
98. Vasylyev M.O., Mordyuk B.M., Voloshko S.M., Zakiyev V.I., Burmak A.P., Pefti D.V. Hardening of surface layers of Cu–39Zn–1Pb brass at holding and high-frequency impact deformation in liquid nitrogen, *Metallofiz. Noveishie*

- Tekhnol. 41 (No. 11) (2019) 1499–1517,
<https://doi.org/10.15407/mfint.41.11.1499>
99. Vasylyev M.A., Mordyuk B.N., Sidorenko S.I., Voloshko S.M., Burmak A.P. Influence of microstructural features and deformation-induced martensite on hardening of stainless steel by cryogenic ultrasonic impact treatment, *Surf. Coat. Technol.* 343 (2017) 57–68,
<https://doi.org/10.1016/j.surfcoat.2017.11.019>
100. Bunge H.-J. X-ray texture analysis in materials and earth sciences. *European Journal of Mineralogy* 1997;; 9 (4): 735–761. doi: 10.1127/ejm/9/4/0735
101. Inaba K., Kobayashi Sh., Uehara K., Okada A., Reddy S. L., Endo T. High Resolution X-Ray Diffraction Analyses of (La,Sr)MnO₃/ZnO/Sapphire(0001) Double Heteroepitaxial Films, *Advances in Materials Physics and Chemistry*, 2013, 3, 72-89, DOI: 10.4236/ampc.2013.31A010
102. David J. D. et al. A review of EBSD: from rudimentary on line orientation measurements to high resolution elastic strain measurements over the past 30 years, *IOP Conf. Series: Materials Science and Engineering* 375 (2018) 012003 doi:10.1088/1757-899X/375/1/012003
103. Davis J.R., *Tensile Testing (Second Edition)*, ASM International, (2004), doi: 10.31399/asm.tb.tt2.9781627083553
104. Yalcin D., How do different specimen geometries affect tensile test results? (2017)
105. Potter U.J., Love G., *Microscopy | Transmission Electron Microscopy*, *Encyclopedia of Food Microbiology*, 1999, Pages 1407-1418, doi: 10.1006/rwfm.1999.1075
106. Xin J., Chaudhari R.V. *Handbook of Solid State Chemistry, Hydrogenation by Metals*, 2017, DOI: 10.1002/9783527691036.hsscvol6025
107. Bisht A., Ray N., Jagadeesh G., Suwas S. Microstructural and crystallographic response of shockloaded pure copper, *J. Mater. Res.* 32 (2017) 1484–1498. <https://doi.org/10.1557/jmr.2017.15>

108. Mordyuk B.N., Prokopenko G.I. Ultrasonic impact treatment – an effective method for nanostructuring the surface layers of metallic materials, in: M. Aliofkhazraei (Ed.), Handbook of Mechanical Nanostructuring, Wiley-VCH, 2015, pp. 417–434. <http://doi.org/10.1002/9783527674947.ch17>
109. Mordyuk B.N., Karasevskaya O.P., Prokopenko G.I., Structurally induced enhancement in corrosion resistance of Zr–2.5% Nb alloy in saline solution by applying ultrasonic impact peening, Mater. Sci. Eng. A 559 (2013) 453–461, <https://doi.org/10.1016/j.msea.2012.08.125>.
110. Xie J.F., Zhu Y.L., Bian F.L., Liu C. Dynamic recovery and recrystallization mechanisms during ultrasonic spot welding of Al-Cu-Mg alloy, Mater. Character. 132 (2017) 145–155, <https://doi.org/10.1016/j.matchar.2017.06.018>
111. Mishra A., Kad B.K., Gregori F., Meyers M.A. Microstructural evolution in copper subjected to severe plastic deformation: experiments and analysis, Acta Mater. 55 (2007) 12–28, <https://doi.org/10.1016/j.actamat.2006.07.008>.
112. Glezer A.M., Metlov L.S. Physics of megaplastic (severe) deformation in solids, Phys. Solid State 52 (6) (2010) 1162–1169, <https://doi.org/10.1134/S1063783410060089>
113. Cho C.-H., Son K., Cho H.. Experimental analysis of deformation texture evolutions in pure Cu, Cu-37Zn, Al-6Mg, and –8Mg alloys at cold-rolling processes, J. Alloys Compounds 934, 2023, 167879. <https://doi.org/10.1016/j.jallcom.2022.167879>
114. Mordyuk B.N., Khripta N.I., Zhao L.G. Twinning-related enhancement in strength and ductility of Cu-37Zn alloy by the cryogenic ultrasonic impact treatment supplemented with ECAP, Mater. Lett. 310 (2022) 131512, <https://doi.org/10.1016/j.matlet.2021.131512>
115. Blaha F., Langenecker B. Tensile deformation of zinc crystal under ultrasonic vibration, Naturwissenschaften 42 (1955) 556, <https://doi.org/10.1007/BF00623773>.
116. Xiao G.H., Tao N.R., Lu K. Microstructures and mechanical properties of a

- Cu–Zn alloy subjected to cryogenic dynamic plastic deformation, *Mater. Sci. Eng. A* 513–514 (2009) 13–21, <https://doi.org/10.1016/j.msea.2009.01.022>.
117. Lu K., Lu L., Suresh S. Strengthening materials by engineering coherent internal boundaries at the nanoscale, *Science* 324 (2009) 349–352, <https://doi.org/10.1126/science.1159610>.
118. Wang P.F., Jie J., Sun X., Liu W., Li T. Simultaneous achievement of high strength and superior ductility in an as-rolled Cu-30Zn brass, *J. Mater. Eng. Perform.* 28 (2019) 7782–7788, <https://doi.org/10.1007/s11665-019-04503-3>.
119. Kumar N.K., Roy B., Das J. Effect of twin spacing, dislocation density and crystallite size on the strength of nanostructured α -brass, *J. Alloy. Compd.* 618 (2015) 139–145, <https://doi.org/10.1016/j.jallcom.2014.08.131>.
120. Turki A., Guelorget B., Optasanu V., François M., Herbst F., Njah N. Microstructure and activation volume of a Cu-6 wt%Zn brass processed by equal channel angular pressing, *J. Alloy. Compd.* 968 (2023) 171974, <https://doi.org/10.1016/j.jallcom.2023.171974>.
121. Zhang P., An X.H., Zhang Z.J., Wu S.D., Li S.X., Zhang Z.F, Figueiredo R.B., Gao N., Langdon T.G. Optimizing strength and ductility of Cu–Zn alloys through severe plastic deformation, *Scr. Mater.* 67 (2012) 871–874, <https://doi.org/10.1016/j.scriptamat.2012.07.040>.
122. Wang P., Jie J., Liu C., Guo L., Li T. An effective method to obtain Cu-35Zn alloy with a good combination of strength and ductility through cryogenic rolling, *Mater. Sci. Eng. A* 715 (2018) 236–242, <https://doi.org/10.1016/j.msea.2018.01.014>.
123. Cai B.Z., Ma X.L., Moering J., Zhou H., Yang X.C., Zhu X.K. Enhanced mechanical properties in Cu–Zn alloys with a gradient structure by surface mechanical attrition treatment at cryogenic temperature, *Mater. Sci. Eng. A* 626 (2015) 144–149, <https://doi.org/10.1016/j.msea.2014.12.070>.
124. Balogh L., Ungar T., Zhao Y.H., Zhu Y.T., Horita Z., Xu C., Langdon T.G. Influence of stacking-fault energy on microstructural characteristics of ultrafine-grain copper and copper–zinc alloys, *Acta Mater.* 56 (2008) 809–820,

- <https://doi.org/10.1016/j.actamat.2007.10.053>.
125. Gu L., Liang N.N., Chen Y.Y., Zhao Y.H. Achieving maximum strength-ductility combination in fine-grained Cu-Zn alloy via detwinning and twinning deformation mechanisms, *J. Alloy. Compd.* 906 (2022) 164401, <https://doi.org/10.1016/j.jallcom.2022.164401>.
 126. Liu Q., Xiong Z.W., Yang J., Fang L.M., Liu Y., Li J., Zhu X.Y., He R., Zhu W.K., Gao Z. Deformation induced phase transition in brass under shock compression, *Mater. Today Commun.* 35 (2023) 106224, <https://doi.org/10.1016/j.mtcomm.2023.106224>.
 127. Zhu Y.T., Liao X.Z., Wu X.L. Deformation twinning in nanocrystalline materials, *Prog. Mater. Sci.* 57 (2012) 1–62, <https://doi.org/10.1016/j.pmatsci.2011.05.001>.
 128. Wu H., Fan G. An overview of tailoring strain delocalization for strength-ductility synergy, *Prog. Mater. Sci.* 113 (2020) 100675, <https://doi.org/10.1016/j.pmatsci.2020.100675>.
 129. Petrov Y.N., Vasylyev M.A., Trofimova L.N., Makeeva I.N., Filatova V.S., Layer wise evolution of the Cu–Zn alloy microstructure after sandblasting, *Appl. Surf. Sci.* 327 (2015) 1–6, <https://doi.org/10.1016/j.apsusc.2014.10.162>.
 130. Kozlov A.V., Selitser S.I. Peculiarities in the plastic deformation of crystals subjected to the acoustoplastic effect, *Mater. Sci. Eng. A* 102 (1988) 143–149, [https://doi.org/10.1016/0025-5416\(88\)90568-X](https://doi.org/10.1016/0025-5416(88)90568-X).
 131. Mordyuk B.N. Flow stress behavior of polycrystalline Ni under combined magnetoand acousto-plastic effects, *Mater. Sci. Eng. A* 397 (2005) 322–329, <https://doi.org/10.1016/j.msea.2005.02.053>.
 132. Iwaoka H., Hirosawa S. First-principles calculation of elastic properties of Cu-Zn intermetallic compounds for improving the stiffness of aluminum alloys, *Comput. Mater. Sci.* 174 (2020) 109479, <https://doi.org/10.1016/j.commatsci.2019.109479>.
 133. Alexandrov I.V., Serebryany V.N., Sarvarova L.N., Alexandrova M.V., Valiev R.Z., Texture and young's modulus anisotropy in nanostructured copper,

- Textures and Microstructures, 32 (1999) 321–339.
<http://doi.org/10.1155/TSM.32.321>
134. Murdoch H.A., Darling K.A., Roberts A.J., Kecskes L. Mechanical behavior of ultrafine gradient grain structures produced via ambient and cryogenic surface mechanical attrition treatment in iron. *Metals* 5(2) (2015) 976–985.
<https://doi.org/10.3390/met5020976>
135. Xiong Q.L., Li Z., Shimada T., Kitamura T. Energy storage and dissipation of elastic-plastic deformation under shock compression: Simulation and Analysis, *Mech. Mater.*, 2021, 158, 103876.
<https://doi.org/10.1016/j.mechmat.2021.103876>
136. Sheng G.U.O., Liu C. T. Phase stability in high entropy alloys: Formation of solid-solution phase or amorphous phase / *Progress in Natural Science: Materials International* 21 (2011) 433–446, DOI: 10.1016/S1002-0071(12)60080-X
137. Wang X., Zhang L., Guo Z., Jiang Y., Tao X., Liu L. Study of low-modulus biomedical β Ti–Nb–Zr alloys based on single-crystal elastic constants modeling, *Journal of the mechanical behavior of biomedical materials*: V.62 (2016).- P.310–318. <http://dx.doi.org/10.1016/j.jmbbm.2016.04.040>
138. Konopatsky A. , Dubinskiy S., Zhukova Y., Sheremetyev V., Brailovski V. , Prokoshkin S., Filonov M. Ternary Ti-Zr-Nb and quaternary Ti-Zr-Nb-Ta shape memory alloys for biomedical applications: Structural features and cyclic mechanical properties *Materials Science and Engineering A* 702 (2017) 301-311 DOI: 10.1016/j.msea.2017.07.046
139. Sheremetyev V., Kudryashova A., Cheverikin V., Korotitskiy A., Galkin S., Prokoshkin S., Brailovski V. Hot radial shear rolling and rotary forging of metastable beta Ti-18Zr14Nb (at. %) alloy for bone implants: Microstructure, texture and functional properties, *Journal of Alloys and Compounds* 800 (2019) 320e326 doi.org/10.1016/j.jallcom.2019.06.041

LIST OF ABBREVIATIONS

FCC – face-centered cubic (lattice)
BCC – body-centered cubic (lattice)
UIT – ultrasonic impact treatment
HESC – high-energy shock compression
USTA – ultrasonic texture analysis
Air-UIT – UIT at room temperature
Cryo-UIT – UIT at cryogenic temperature
HE – hydrogen embrittlement
VEC – valence electron concentration
HEDE – hydrogen enhanced decohesion
HELP – hydrogen enhanced localized plasticity
SEM – scanning electron microscop(y)
SAED – selected area electron diffraction
EBSD – electron backscattering diffraction
TEM – трансмісійна електронна мікроскопія